Fabrication and Optical Characterisation of Yagi-Uda-Antennas and Silica/Gold Core-Satellite Structures

Dissertation
der Mathematisch-Naturwissenschaftlichen Fakultät
der Eberhard Karls Universität Tübingen
zur Erlangung des Grades eines
Doktors der Naturwissenschaften
(Dr. rer. nat.)

vorgelegt von
Felix Nägele
aus Tübingen

Tübingen
2024

Gedruckt mit Genehmigung der Mathematisch-Naturwissenschaftlichen Fakultät der Eberhard Karls Universität Tübingen.

Tag der mündlichen Qualifikation:	27.06.2024
Dekan:	Prof. Dr. Thilo Stehle
1. Berichterstatterin:	Prof. Dr. Monika Fleischer
2. Berichterstatterin:	PD Dr. Dai Zhang

Abstract

In this work, different plasmonic nanostructures were fabricated, investigated using various methods and tested for their sensing abilities. Firstly, nanoscopic Yagi-Uda-antennas were fabricated, whose working principle is proved in the radio frequency range for decades [1, 2]. Their operation principles rely on the constructive and destructive interference of electromagnetic waves, which are emitted by an active element and re-emitted by passive elements. This proven principle was converted here amongst other works to the optical regime.
To find optimal parameters, Finite Difference Time Domain (FDTD) simulations were carried out. The fabrication mostly relied on electron beam lithography, however focused helium ion beam milling is used for the fabrication as well. With the help of this microscope, either whole antenna structures could be fabricated or existing antennas could be manipulated.
Spectra were taken in a Dark Field (DF) microscope, where simple antennas as well as antennas incorporated in a flow cell were investigated. The advantage of a flow cell is the simple manipulation of the local refractive index with the help of different liquids.
Furthermore, the emission characteristics of the antenna were probed with the help of a Back Focal Plane (BFP) microscope built by Annika Mildner, where it was tried to manipulate the emission direction. To do so, simple antennas were incorporated into a flow cell, and a higher refractive index medium was used to influence the polar angle of emission. To change the azimuthal angle of emission, each element of an antenna was half covered in silicon dioxide, and measurements in different refractive index media were carried out.
Additionally, antennas were fabricated on a silicon substrate to be used by Felix Schneider in second harmonic generation (SHG) experiments in a parabolic mirror setup.

In the second part of the thesis, core-satellite-structures consisting of one or two silica cores surrounded by gold nanospheres were investigated. The structures were synthesised by Dr. Yingying Cai from the University of Göttingen, using wet chemistry. FDTD simulations were carried out to determine the expected spectra and obtain the plasmonic modes. DF spectra were taken with unpolarised and linearly polarised light of different orientation and compared to the simulations. Additionally, the Surface Enhanced Raman Spectroscopy (SERS) properties of the structures were determined by covering the structures in Raman active material. Lastly, the sensitivity of the resonance shift of the core-satellite structures depending on the local refractive index was investigated.

Zusammenfassung

In der hier vorliegenden Arbeit wurden verschiedene plasmonische Nanostrukturen hergestellt, mit unterschiedlichsten Methoden untersucht und auf Sensoreigenschaften überprüft. Zunächst wurden nanoskopische Yagi-Uda-Antennen hergestellt, deren Prinzip seit Jahrzehnten im Radiofrequenzbereich erprobt ist [1, 2]. Ihre Funktion beruht auf der konstruktiven und destruktiven Interferenz von elektromagnetischen Wellen, die von einem aktiven Element ausgehen und von passiven Elementen erneut ausgestrahlt werden. Das erprobte Prinzip wird nun wie in vorherigen Arbeiten auf den optischen Spektralbereich übertragen. Um die optimalen Parameter zu finden werden zunächst sogenannte Finite Difference Time Domain (FDTD, engl. Finite-Differenzen-Methode im Zeitbereich) Simulationen durchgeführt. Die Fabrikation der Antennen erfolgt zum Großteil mit Hilfe von Elektronenstrahllithografie, wobei auch fokussiertes Helium-Ionen-Strahl ätzen eingesetzt werden kann. Entweder die komplette Herstellung einer Antenne oder nur die Manipulation existierender Antennen ist mit diesem Gerät erfolgt.
Spektroskopische Untersuchungen wurden an einem Dunkelfeldmikroskop (DF) durchgeführt, wobei einfache Antennen als auch Antennen in Flusszellen untersucht wurden. In den Flusszellen kann auf einfache Weise der lokale Brechungsindex um die Antennen durch unterschiedliche Flüssigkeiten verändert werden.
Ebenfalls wurde das Abstrahlverhalten der Antennen in einem Back Focal Plane (BFP, engl. rückwärtige Brenneben, manchmal auch Fourierebene) Mikroskop, welches von Annika Mildner gebaut wurde, untersucht. Es wurde versucht, die Abstrahlcharakteristik zu beeinflussen: zum einen durch einen höheren Brechungsindex um eine unveränderte Antenne, wobei sich der Polarwinkel der Abstrahlung verändert, zum anderen wurde der Versuch mit einer Antenne wiederholt, bei der die eine Hälfte eines jeden Antennenelements mit Siliziumdioxid bedeckt ist. Dadurch konnte eine Änderung der Abstrahlrichtung im Azimuthalwinkel beobachtet werden.
Zusätzlich dazu wurden noch Antennen auf einem Silizium-Substrat hergestellt, welche in einem Parabolspiegelaufbau von Felix Schneider auf Frequenzverdopplung untersucht wurden.

Des Weiteren wurden Core-Satellite (engl. Kern-Satellit) Strukturen untersucht, welche nasschemisch von Dr. Yingying Cai an der Universität Göttingen synthetisiert wurden und aus einem oder zwei Siliziumdioxid-Kernen bestehen, welche von Gold-Nanokugeln umgeben sind. FDTD-Simulationen dienten zur Bestimmung der plasmonischen Moden und der zu erwartenden Spektren. Es wurden DF-Spektren aufgenommen mit unpolarisierter und linear polarisierter Beleuchtung unterschiedlicher Orientierung und mit den Simulationen verglichen. Des Weiteren wurde die Eignung der Strukturen für Surface Enhanced Raman Spectroscopy (SERS, engl. Oberflächenverstärkte Raman Spektroskopie) eruiert, indem die Strukturen mit Raman-aktivem Material benetzt wurden. Zu guter Letzt wurde noch der Shift der Resonanzfrequenz der Core-Satellite-Strukturen in Abhängigkeit vom lokalen Brechungsindex untersucht.

Contents

1 Introduction

Gold nanostructures have been the topic of extensive research over the last couple of decades due to their versatility and unique properties [3, 4, 5]. Their area of application ranges from localized, self heating nanoparticles to destroy cancer cells [6], to drug delivery [7] and colorimetric sensing due to their high absorption and light scattering properties [8, 9, 10]. Also, their optical properties combined with a surface activation makes them suitable for biosensing applications [11, 12] and their high-intensity, localised electromagnetic near field can be used for surface-enhanced Raman spectroscopy (SERS) [13, 14].
All these applications are based on localised surface plasmon resonances (LSPRs), which describe the collective oscillation of conduction band electrons in response to the oscillating electromagnetic field of incident light [15]. To tune the LSPRs, multiple nanoparticles are assembled into new structures of more complex geometry. This way the individual LSPR modes can couple and new hybridised modes appear [16, 17, 18].
The hybridisation of modes in complex nanostructures also occurs in this work. Here the assemblies of nanostructures are so called Yagi-Uda-antennas, which consist of several gold nanorods of specific geometry and arrangement as well as core-satellite-structures, that are made from one or two silica cores and are surrounded by gold nanospheres. While Yagi-Uda-antennas have proven themselves in the radio frequency regime for decades with a simple and robust design and great directivity of emission, the core-satellite-structures do not have such macroscopic counterpart. Nevertheless, great properties and applications of such structures have been discovered in recent years.
The goal of this work is on the one hand, the fabrication of Yagi-Uda-Antennas in the visible frequency range, as well as the characterisation of their emission pattern. Additionally, antennas were modified in different ways which leads to a manipulation of the emission pattern, which again can be seen in the back focal plane of the microscope objective.
On the other hand, core-satellite structures were simulated to obtain the hybridised plasmon modes. It was taken advantage of these modes and their high near field enhancement to perform surface enhanced Raman spectroscopy as well as refractive index sensing measurements.

1.1 State of the art

To set a context of this work, an overview is given about the state of the art of the two main topics that were handled during this thesis. A brief overview over advancements and applications of optical Yagi-Uda-antennas is given, and different experiments and combinations of core-satellite particles are shown.

1.1.1 Yagi-Uda-antennas

After the invention of radio-frequency Yagi-Uda-antennas in 1926 [1], it took around 80 years to come up with a theoretical proposal of such an antenna for the optical regime. Hofmann et al. and Li et al. proposed, independently of each other, design parameters for a Yagi-Uda-antenna in the optical regime [19, 20]. These theories have been followed up by a number of other theoretical/numerical works, for example for single emitters coupled to optical Yagi-Uda-antennas [21], antennas based on dielectric particles [22], a three-dimensional array of antennas for laser collimation [23], bistable, actively tunable antennas with a semiconductor disc incorporated in the feed of an antenna made from silver [24] but also for optical spectrometers consisting of several antennas, that make use of the changing response to different wavelength excitations [25]. A first paper on directing the second harmonic generated in a gold sphere via the help of two dielectric reflector and director spheres can be found in the work of Xiong et al. [26]. Lastly, the use for optical communication systems has been discussed [27, 28].
Additional to the theoretical works, some Yagi-Uda-antennas with different features have been fabricated and investigated. One of the first doing so were again the Hofmann group, that electron beam lithographically produced such an antenna consisting of gold rods, however with the feed element rotated by 45° compared to the reflector and director elements [29]. The theoretical calculations from their previous work ([21]) could thereby be experimentally confirmed by the group. Quantum dots were successfully coupled to the feed element of a Yagi-Uda-antenna, and its emission was now unidirectional instead of isotropic [30]. Moreover, antennas, which are driven by plasmon-modulated photoluminescence, were fabricated and showed clear directivity in emission. An L-shaped arrangement of two such antennas, which are resonant at different frequencies, could even be used to direct different wavelengths to different directions [31].
However, not only two-dimensional, single antennas were investigated. Arrays of stacked antenna elements were fabricated, and their directive absorption was measured [32]. For a further understanding of the antennas, their near-field dynamics were measured [33].
Further experiments where reflector and director elements were placed around different emitters like a semiconductor wire, an electrically driven feed element and a bow-tie antenna can be found in [34, 35, 36]. A last interesting twist on a Yagi-Uda-antenna can be found in [37], where instead of metal particles, cavities in a waveguide function as antenna elements.
All in all, the research into optical Yagi-Uda-antennas is still relatively limited with

no actual measurements for this antenna type as a sensor, where it was tried to actively manipulate the emission of the antenna, which leads to an interesting field of research.

1.1.2 Core-satellite structures

The term core-satellite structures generally refers to nanoscopic assemblies consisting of a single or multiple core structures that are surrounded by smaller peripheral structures. The surface of the core particles is typically not completely covered by these surrounding satellite particles [38].
Since the first DNA-directed synthesis of such particles in 1998 [39] multiple variations of assembling methods, material combinations and shapes have emerged. Due to this versatility, a wide range of applications have been found for these core satellite particles, which are explained later. It should be noted, that most of the applications are based on the so-called localised surface plasmon resonances (LSPRs), the collective oscillation of conduction electrons in response to the oscillating electromagnetic field of incoming light [15]. These LSPRs can be tuned by assembly of nanoparticles to form new structures, as is the case in core-satellite structures. Here the individual modes couple, and new hybridised modes appear [16, 17, 18].
One application of core-satellite structures is to exploit their optical properties to form a refractive index sensor. Ode et al. [40] found that the coupled LSPR peaks of gold core/gold satellite structures are more sensitive to refractive index shifts than their native counterparts and received a sensitivity of ca. 350 nm/RIU. With the help of surface activation, this sensor can be further expanded to a biosensor [41, 42, 43]. Furthermore, it was shown that the disassembly and formation of the whole core-satellite structure can be used as a colorimetric biosensor [44, 45].
Another application that makes use of LSPR or rather the high field enhancement between the core and satellite or satellite and satellite is the surface enhanced Raman spectroscopy (SERS) [46, 47, 48]. Finite-difference time-domain (FDTD) simulations already revealed high intensities between particles, several orders of magnitude higher than on sphere surfaces alone [49]. Additionally, they found that core-satellite chains exhibit higher enhancements than individual core-satellite particles.
SERS measurements were carried out on multiple structures such as gold nanorod core/silver nanoparticle satellite structures, that took advantage of high single-particle SERS enhancement of silver compared to gold [50] and gold nanorod core/gold nanoparticle satellite structures, which showed that the SERS signal increases nearly proportionally with the number of satellites per core [51]. Other material combinations for SERS measurements include hollow porous gold nanoshell [52], iron core / gold satellite structures [53, 41] and silver core / gold satellite structures [54] among others.
Other applications of core satellite structures range from thermoresponsive measurements [55, 56] to cancer therapy [57, 58, 59, 60] and drug delivery [61, 62].
Due to the high customisability of core satellite structures, various material combinations such as the mentioned gold core / silver satellite structures [50, 63], gold

core / gold satellite structures [39, 46, 64, 40, 65, 66], silica core structures [55, 67, 68] and iron oxide cores [41, 69, 53] are possible structures, but even exotic materials like $NaYbF_4$ core / CaF_2 satellite structures [61] as well as ZnS core / gold satellite structures [70] have been reported.
Not only the material can be changed, but also the shape. From rod-shaped core [50] to nanocubes as core [65] to star-shaped cores [71] many options are available. Additional to these parameters, gap size, particle size, core size and arrangement of the structures (such as satellite position or multicore structures) are free to change to obtain the structure with desired properties.
In the work presented here, chemically bottom-up fabricated core-satellite structures consisting of one or two silica cores surrounded by gold nanosphere satellites are investigated and compared to FDTD simulations. The structures are fabricated by Yingying Cai at the group of Philipp Vana at the University of Göttingen [72].

2 Fundamental theory

In this chapter, some of the theoretical fundamentals are explained to understand the content of this work. First, some electromagnetic and plasmonic basics are outlined, followed by their application in Yagi-Uda-antennas. Furthermore, a look at the simulation method of finite difference time domain (FDTD) is taken, before continuing to nonlinear properties of solid state particles and finishing with the theory of Raman spectroscopy.

2.1 Plasmons

Since plasmons are the fundamental physical effect, that play a role throughout this whole work, a theory is given on what they are and how they behave. Plasmons describe the interaction of electromagnetic waves with the free electrons of the conductance band in metals. Under certain circumstances, a collective oscillation of the density of these electrons can be excited, which then behaves like a quasi particle: the plasmon. One can distinguish between three major types of plasmons: bulk plasmons in volume materials, surface plasmon polaritons (SPP) (see chapter 2.1) at surfaces and boundaries and localised surface plasmon polaritons (LSPP) (see chapter 2.3) in particles, that are smaller than the wavelength of the exciting electromagnetic wave.
To understand these phenomena better, a brief overview is given over how electromagnetic waves behave and can be described (see chapter 2.1.1) and how electrons behave in a metal (see chapter 2.1.3). The following chapters are oriented along the books *Elektrodynamik, Optik* and *Principles of Nano-Optics* [73, 74, 75].

2.1.1 Maxwell's equations

Maxwell's equations, named after James Clerk Maxwell, are a set of four differential equations which describe the phenomenological relation between electric fields $\vec{E}$, magnetic flux density $\vec{B}$, electric charge densities ρ and current densities $\vec{j}$. The four equations are introduced separately, and their meaning described in a few words.

Gauss's law

$$\vec{\nabla} \cdot \vec{E}\,(\vec{r}, t) = \frac{\rho\,(\vec{r}, t)}{\epsilon_0} \tag{2.1}$$

Gauss's law says, that the source of the electric field is electric charges. Furthermore, the net outflow of electric field through a closed surface is proportional to the electric charges that are enclosed by it. The constant of proportionality between the two is the permittivity of free space ϵ_0.

Gauss's law for magnetism

$$\vec{\nabla} \cdot \vec{B}\left(\vec{r}, t\right) = 0 \tag{2.2}$$

Gauss's law for magnetism says, that the magnetic flux density does not diverge, which means that the magnetic field is source free and field lines have to be closed loops. Magnetic monopoles therefore do not exist.

Faraday's law of induction

$$\vec{\nabla} \times \vec{E}\left(\vec{r}, t\right) = -\frac{\partial \vec{B}\left(\vec{r}, t\right)}{\partial t} \tag{2.3}$$

Faraday's law of induction says, that a change of the magnetic flux density in time leads to a curl of an electric field. The negative sign is due to Lenz's law.

Ampère's law with Maxwell's addition

$$\vec{\nabla} \times \vec{B}\left(\vec{r}, t\right) = \mu_0 \vec{j}\left(\vec{r}, t\right) + \mu_0 \epsilon_0 \frac{\partial \vec{E}\left(\vec{r}, t\right)}{\partial t} \tag{2.4}$$

The original Ampère's law states, that electric currents generate a magnetic field around them. The addition by Maxwell states, that additionally magnetic fields also relate to changing electric fields which are called displacement currents by Maxwell. In the equation above, μ_0 relates to the permeability of free space.

2.1.2 Electromagnetic Waves

To solve Maxwell's equations in vacuum and to achieve a solution for propagating electromagnetic waves, one applies an additional rotation operator to equations 2.3 and 2.4. One obtains:

$$\vec{\nabla} \times \left(\vec{\nabla} \times \vec{E}\left(\vec{r}, t\right) \right) = -\frac{\partial \left(\vec{\nabla} \times \vec{B}\left(\vec{r}, t\right) \right)}{\partial t}, \tag{2.5}$$

$$\vec{\nabla} \times \left(\vec{\nabla} \times \vec{B}\left(\vec{r}, t\right) \right) = \epsilon_0 \mu_0 \frac{\partial \left(\vec{\nabla} \times \vec{E}\left(\vec{r}, t\right) \right)}{\partial t}. \tag{2.6}$$

Now one substitutes equations 2.3 and 2.4 again into the right side of equations 2.5 and 2.6:

$$\vec{\nabla} \times \left(\vec{\nabla} \times \vec{E}\left(\vec{r}, t\right) \right) = -\epsilon_0 \mu_0 \frac{\partial^2 \vec{E}\left(\vec{r}, t\right)}{\partial t^2}, \tag{2.7}$$

$$\vec{\nabla} \times \left(\vec{\nabla} \times \vec{B}\left(\vec{r}, t\right) \right) = -\epsilon_0 \mu_0 \frac{\partial^2 \vec{B}\left(\vec{r}, t\right)}{\partial t^2}. \tag{2.8}$$

The operator identity $\nabla \times \left(\nabla \times \vec{A} \right) = \nabla \left(\nabla \cdot \vec{A} \right) - \Delta \vec{A}$ with Δ being the Laplace operator comes in handy and transforms equations 2.7 and 2.8 with respect to equations 2.1 and 2.2, which both equal zero in vacuum as follows:

$$\Delta \vec{E}\left(\vec{r}, t\right) = \epsilon_0 \mu_0 \frac{\partial^2 \vec{E}\left(\vec{r}, t\right)}{\partial t^2} \tag{2.9}$$

$$\Delta \vec{B}\left(\vec{r}, t\right) = \epsilon_0 \mu_0 \frac{\partial^2 \vec{B}\left(\vec{r}, t\right)}{\partial t^2}. \tag{2.10}$$

With additionally $c = \sqrt{\epsilon_0 \mu_0}$, the non-trivial solution to that equation is an electromagnetic wave, which travels at the speed of light. It is important to remember that additionally to the wave equation a possible solution for electromagnetic waves also has to fulfil Maxwell's equations to be physically correct. The ansatz for solving equation 2.9 is:

$$\vec{E}\left(\vec{r}, t\right) = \vec{E}_0 e^{i\left(\vec{k}\vec{r} - \omega t\right)}, \tag{2.11}$$

with $\vec{E}_0$ being the amplitude of the wave, ω being the angular frequency and $\vec{k}$ being the vector, that expresses the direction of propagation. The equations can be translated with $c = \sqrt{\epsilon \epsilon_0 \mu \mu_0}$ for the propagation of light in different media.
In vacuum (and in a very good approximation in air) the field vectors $\vec{E}$ and $\vec{B}$ are perpendicular to each other and both are again perpendicular to the direction of propagation $\vec{k}$.

2.1.3 Free Electron model

To explain a number of effects and the optical properties in metals, one can look at a plasma model [76]. In this model, free electrons with a number density of n behave like a gas and move on a background of fixed, positive ion cores. The details of the lattice potential like distance and geometry are not taken into account, as well as electron-electron interactions. Instead, aspects of the band structure are incorporated into an effective mass m of the electrons.
As a response to an external electromagnetic wave, the electrons start to oscillate. Their motion however is damped by collisions, which occur at a characteristic frequency $\gamma = 1/\tau$, where τ is the relaxation time of the free electron gas. To derive the dielectric function, which is important to describe plasmonic effects, a look at the equation of motion for electrons influenced by an external field $\vec{E}(t) = \vec{E}_0 e^{(-i\omega t)}$ is taken:

$$m\frac{\partial^2 \vec{r}}{\partial t^2} + m\gamma\frac{\partial \vec{r}}{\partial t} = e\vec{E}_0 e^{(-i\omega t)}. \tag{2.12}$$

In equation 2.12, ω is the frequency of the external electromagnetic field $\vec{E}_0$ and e is the charge of an electron. An ansatz for a particular solution to that differential equation is an oscillating electron with $\vec{r}(t) = \vec{r}_0 e^{(-i\omega t)}$. The solution is then:

$$\vec{r}(t) = \frac{e}{m\left(\omega^2 + i\gamma\omega\right)}\vec{E}(t), \tag{2.13}$$

where the complex amplitude incorporates the phase shift between the exciting electromagnetic wave and the oscillation response of the electron.
The displacement of the electrons induces a macroscopic polarisation $\vec{P} = -ne\vec{r}$ and is therefore:

$$\vec{P}(t) = -\frac{ne^2}{m\left(\omega^2 + i\gamma\omega\right)}\vec{E}(t). \tag{2.14}$$

The plasma frequency $\omega_p = \sqrt{\frac{ne^2}{\epsilon_0 m}}$ is the frequency at which undamped electrons would oscillate after excitation. With the introduction of the frequency-dependent polarisation

$$\vec{P}(\omega) = \epsilon\chi(\omega)\vec{E}(\omega), \tag{2.15}$$

where χ is the electric susceptibility and the frequency-dependent dielectric function

$$\epsilon(\omega) = 1 + \chi(\omega) \tag{2.16}$$

the dielectric function of a free electron gas can be derived. By substituting the plasma frequency into equation 2.14 and comparison with equations 2.15 and 2.16, one obtains the frequency-dependent dielectric function of the free electron gas:

$$\epsilon(\omega) = 1 - \frac{\omega_p^2}{\omega^2 + i\gamma\omega}. \tag{2.17}$$

This model holds validity for alkali metals through the visible range up to the ultraviolet regime. For noble metals, the model is limited due to interband transitions in

the visible spectrum for wavelengths of 500 nm and lower [77].
To accommodate for that effect, the differential equation 2.12 gets expanded by a linear term that represents the restoring force of the nuclei on an excited electron. The spring constant of that force is α, and the effective mass of the bound electron is m^*, which is material and temperature dependent. The modified equation of motion of the electron is:

$$m^* \frac{\partial^2 \vec{r}}{\partial t^2} + m^* \gamma \frac{\partial \vec{r}}{\partial t} + \alpha \vec{r} = e\vec{E}_0 e^{(-i\omega t)}. \tag{2.18}$$

With the same ansatz as above one obtains the extended dielectric function of

$$\epsilon(\omega) = 1 + \frac{\tilde{\omega}_p^2}{\omega_0^2 - \omega^2 - i\gamma\omega}. \tag{2.19}$$

$\tilde{\omega}_p$ is the equivalent of the plasma frequency, but only for bound electrons and $\omega_0 = \sqrt{\alpha/m^*}$ incorporates the spring constant. The corrections mentioned above are the idea of the oscillator model, which was developed by Hendrik Antoon Lorentz in 1907 [78].

2.1.4 Surface Plasmon Polariton (SPP)

As discussed above, the valence electrons in metals can be described as a (nearly) free electron gas in front of a background consisting of positively charged nuclei. Under certain circumstances, the electrons can be excited to a collective oscillation: a plasmon. The excitation is quantized and can be seen from a quantum mechanical perspective as bosonic quasi particles.
Amongst the different types of plasmons (as listed above) one of them is the surface plasmon polariton (SPP). The SPP occurs on boundaries between metals and dielectric materials and is a coupling between an oscillation of the charge carrier density and an electromagnetic wave in the dielectric. It is a polariton due to its coupling to the electromagnetic wave. The plasmon propagates parallel to the boundary, is a longitudinal oscillation, and its amplitude decays exponentially in the perpendicular direction to the metal as well as the dielectric material. This can be seen in figure 2.1.

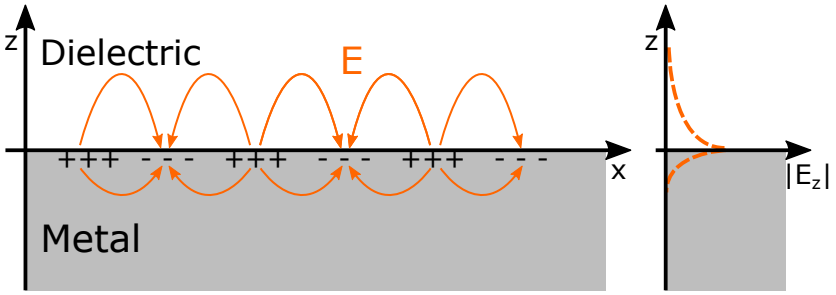

Figure 2.1: Left: visualisation of the oscillating charge carrier density and the electric field of surface plasmon polaritons. Right: exponential decay of the z-component of the electric field in the dielectric material and the charge density distribution in the metal. Adapted from [79].

To obtain the dispersion relation of SPPs, one has to solve Maxwell's equation and search for a solution, which propagates parallel to the metal-dielectric boundary. Furthermore, one has to take into consideration the continuity of the electric and magnetic field at the boundary. Additionally, let for $z < 0$ be the metallic half space and for $z > 0$ the dielectric half space, as in figure 2.1. The whole calculation would exceed this chapter, but can be found in [76].
To understand the results, let $\epsilon_1 = \epsilon_1' + i\epsilon_1''$ be the complex dielectric constant of the metal and $\epsilon_2 = \epsilon_2' + i\epsilon_2''$ the one of the dielectric material. The dispersion relation of the SPP, with a wave vector k_x in x-direction parallel to the boundary, is then

$$k_x = \frac{\omega}{c}\sqrt{\frac{\epsilon_1 \cdot \epsilon_2}{\epsilon_1 + \epsilon_2}} \tag{2.20}$$

with ω the frequency of the electromagnetic wave. Assuming that $|\epsilon_1'| \gg |\epsilon_1''|$ and $|\epsilon_2''| = 0$, the real part of k_x is:

$$k_x' = \frac{\omega}{c}\sqrt{\frac{\epsilon_1' \cdot \epsilon_2}{\epsilon_1' + \epsilon_2}} \tag{2.21}$$

By inserting the dielectric function of the free electron gas (equation 2.17) into equation 2.20, one can see that in the regime of large wave vectors the frequency of SPPs approaches a constant value of:

$$\omega_{SPP} = \frac{\omega_p}{\sqrt{1 + \epsilon_2}}. \tag{2.22}$$

This results in the logical solution that the frequency of the SPP is dependent on the dielectric function of the dielectric material.
A quick look at the wavelengths of SPPs gives the following result:

$$\lambda_{SPP} = \frac{2\pi}{k_x} = \sqrt{\frac{\epsilon_1 + \epsilon_2}{\epsilon_1 \cdot \epsilon_2}}\lambda_0. \tag{2.23}$$

The wavelength in vacuum is λ_0.
To excite an SPP, the momentum and energy of the incident light and plasmon have to match. However, as can be seen in equation 2.21, this is normally not the case. The momentum of the light in the x-direction is smaller than that of the SPP. To overcome that, the field component parallel to the boundary has to be enhanced. This is the case for evanescent waves. Evanescent waves occur in close vicinity of a surface, where total reflection is happening.
In the Otto configuration, the total reflection happens at a prism/air interface and excites SPPs in a metal film in close vicinity to the interface. In the Kretschmann configuration, the total reflection happens at the prism/metal interface and excites SPPs on the surface of the metal opposite to the interface. Both configurations can be seen in figure 2.2. The requirement for SPP excitation is:

$$k_x = \frac{\omega}{c}\sqrt{\epsilon_2'}\sin(\theta). \tag{2.24}$$

A third configuration for SPP excitation, which can also be seen in figure 2.2, has a grating on the surface. Due to refraction of light at the grating with constant g, phase matching takes place between SPP and incoming photon, whenever the condition

$$k_x = \frac{\omega}{c}\sin(\theta) + \frac{2\pi}{g} \tag{2.25}$$

is fulfilled [76].

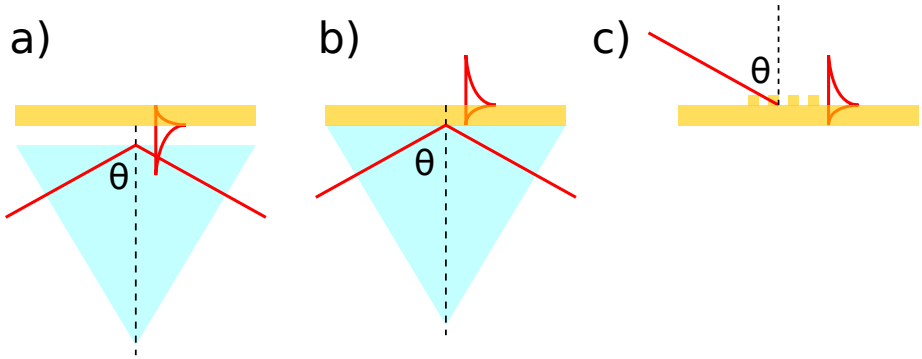

Figure 2.2: a) Otto configuration for SPP excitation. b) Kretschmann configuration for SPP excitation. c) Grating for SPP excitation. Adapted from [80].

2.1.5 Localised Surface Plasmon Polariton (LSPP)

When the dimensions of the examined material are reduced even further from a thin surface region to dimensions where particles are smaller than the wave length of the exciting light in every direction, so called localised surface plasmon polaritons (LSPP) form. As other plasmons, LSPPs can be described as a driven damped oscillator.

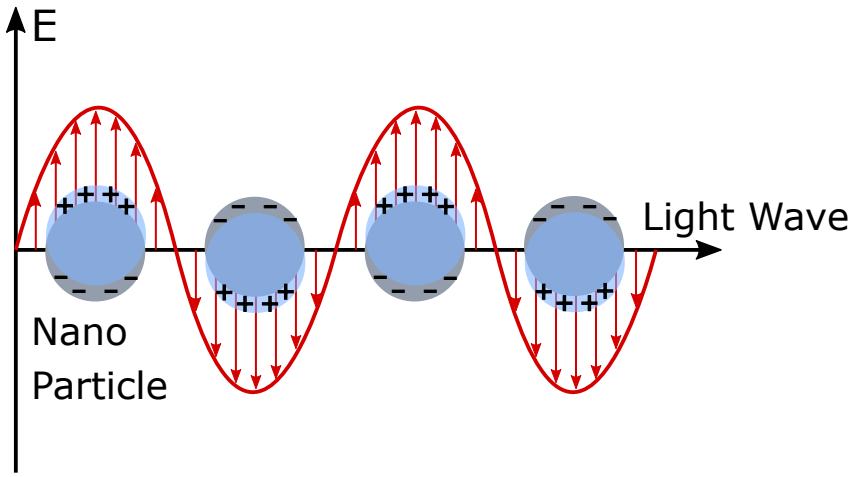

Figure 2.3: Scheme of a localised surface plasmon polariton. The external electric field induces oscillations in the charge density. Adapted from [81].

A model to describe the effects of an LSPP is the quasi-static model. It can be used for particles much smaller than the wave length of the exciting wave. In that case, the field penetrates the whole particle and its phase is constant over the whole range. The problem resembles now a static one with a solution, where the external field excites a dipole proportional to its own field amplitude.
The following calculations to obtain the scattering cross-section and strength of the near field of a spherical particle with radius a are based on [75, 82].
Since the problem is of spherical symmetry, the Laplace equation $\Delta\Phi = 0$ is also written in spherical coordinates (r, θ, φ):

$$\frac{1}{r^2 \sin(\theta)} \left[\sin(\theta) \frac{\partial}{\partial r} \left(r^2 \frac{\partial}{\partial r} \right) + \frac{\partial}{\partial \theta} \left(\sin(\theta) \frac{\partial}{\partial \theta} \right) + \frac{1}{\sin(\theta)} \frac{\partial^2}{\partial \varphi^2} \right] \Phi(r, \theta, \varphi) = 0. \tag{2.26}$$

The solutions for this equation are of the form

$$\Phi(r, \theta, \varphi) = \sum_{l,m} b_{l,m} \cdot \Phi_{l,m}(r, \theta, \varphi), \tag{2.27}$$

where $b_{l,m}$ are constants dependent on the boundary conditions and $\Phi_{l,m}(r, \theta, \varphi)$ are of the form:

$$\Phi_{l,m}(r, \theta, \varphi) = \begin{Bmatrix} r^l \\ r^{-l-1} \end{Bmatrix} \begin{Bmatrix} P_l^m(\cos\theta) \\ Q_l^m(\cos\theta) \end{Bmatrix} \begin{Bmatrix} e^{im\varphi} \\ e^{-im\varphi} \end{Bmatrix}. \tag{2.28}$$

$P_l^m(\cos\theta)$ are the associated Legendre functions, and $Q_l^m(\cos\theta)$ are Legendre functions of the second kind. The case distinction in equation 2.28 is dependent on $l \in \mathbb{N}$, the order of the function, which defines the range of $m \in [-l, l]$. If l is even, the top row is used, if l is uneven, the lower row is used.
Now, let Φ_1 be the potential in the sphere and $\Phi_2 = \Phi_s + \Phi_0$ be the one outside the sphere. $\Phi_0 = -E_0 z = -E_0 r P_1^0(\cos\theta)$ is the external potential and Φ_s the scattering potential. To satisfy the boundary conditions at the surface of the sphere, the electric field as well as the normal component of the electric electric displacement has to be continually, which means for the potential

$$\left.\frac{\partial\Phi_1}{\partial\theta}\right|_{r=a} = \left.\frac{\partial\Phi_2}{\partial\theta}\right|_{r=a}, \tag{2.29}$$

$$\epsilon_1 \left.\frac{\partial\Phi_1}{\partial r}\right|_{r=a} = \epsilon_2 \left.\frac{\partial\Phi_2}{\partial r}\right|_{r=a}. \tag{2.30}$$

ϵ_1 and ϵ_2 are the dielectric functions of the sphere and the surrounding, respectively. With the help of the boundary conditions and the knowledge, that the associated Legendre functions are orthogonal to each other, one obtains the potential inside the sphere

$$\Phi_1 = -\frac{3\epsilon_2}{\epsilon_1 + 2\epsilon_2} E_0 r\cos\theta, \tag{2.31}$$

as well as the potential outside the sphere

$$\Phi_2 = -E_0 r\cos\theta + \frac{\epsilon_1 - \epsilon_2}{\epsilon_1 + 2\epsilon_2} a^3 E_0 \frac{\cos\theta}{r^2}. \tag{2.32}$$

With the help of $\vec{E} = -\nabla\Phi$, one can derive the electric field:

$$\vec{E}_1 = \frac{3\epsilon_2}{\epsilon_1 + 2\epsilon_2} E_0 (\cos\theta\vec{e}_r - \sin\theta\vec{e}_\theta) = \frac{3\epsilon_2}{\epsilon_1 + 2\epsilon_2} E_0 \vec{e}_z, \tag{2.33}$$

$$\vec{E}_2 = E_0 r (\cos\theta\vec{e}_r - \sin\theta\vec{e}_\theta) + \frac{\epsilon_1 - \epsilon_2}{\epsilon_1 + 2\epsilon_2} \frac{a^3}{r^3} E_0 (2\cos\theta\vec{e}_r - 2\sin\theta\vec{e}_\theta) \tag{2.34}$$

One can see in equation 2.33, that the electric field is constant throughout the whole particle, which is consistent with the premise that the particle is smaller than the penetration depth of the external electric field.
The second term of equation 2.34 (the scattered field) is the same as the field of a dipole of moment $\vec{p} = \varepsilon_2 \alpha \vec{E}_0$, placed at the centre of the sphere. The polarisation of such a dipole is:

$$\alpha = 4\pi\epsilon_0 a^3 \frac{\epsilon_1 - \epsilon_2}{\epsilon_1 + 2\epsilon_2}. \tag{2.35}$$

So far the calculations above were made in a static field, however, in actuality the field is oscillating with an angular frequency ω. The electric field of an oscillating

dipole is then given by [83]:

$$\vec{E} = \frac{1}{4\pi\epsilon_2}\left(-\frac{\vec{p}\,(t_0)}{r^3} + \frac{3\vec{r}\left[\vec{r}\cdot\vec{p}\,(t_0)\right]}{r^5} + \frac{ik\vec{p}\,(t_0)}{r^2} - \frac{3ik\vec{r}\left[\vec{r}\cdot\vec{p}\,(t_0)\right]}{r^4} - \frac{k^2}{r^3}\vec{r}\times\left[\vec{r}\times\vec{p}\,(t_0)\right]\right), \tag{2.36}$$

where k is the wave number in the surrounding medium and $t_0 = t - kr/\omega$. The first two terms describe the so-called *static field* and make up the scattered field. The following two terms are the *induction field*, which represent the field induced by the current due to dipole oscillation. The final term is the *radiation field*. Only this field among the last three terms radiates into infinite distance and is therefore the far-field component.
The magnetic field is given by [83]:

$$\vec{H} = -\frac{i\omega}{4\pi}\left(\frac{1}{r^2} - \frac{ik}{r}\right)\vec{r}\times\vec{p}\,(t_0)\,. \tag{2.37}$$

In the developed form the equations become

$$\vec{E} = \frac{\vec{p}e^{ikr}}{4\pi\epsilon_2}\left[\left(\frac{2}{r^3} - \frac{2ik}{r^2}\right)\cos\theta\vec{e}_r + \left(\frac{1}{r^3} - \frac{ik}{r^2} - \frac{k^2}{r}\right)\sin\theta\vec{e}_\theta\right] \tag{2.38}$$

$$\vec{H} = -\frac{i\omega\vec{p}e^{ikr}}{4\pi}\left(\frac{1}{r^2} - \frac{ik}{r}\right)\sin\theta\vec{e}_\varphi. \tag{2.39}$$

These equations can be used to calculate the real part of the Poynting vector, which gives rise to the time average of the energy flow:

$$\bar{S} = \frac{1}{2}\mathrm{Re}\left(\vec{E}\times\vec{H}^*\right) = \frac{1}{2}\mathrm{Re}\left(E_0H_\varphi^*\vec{e}_r - E_rH_\varphi^*\vec{e}_\theta\right). \tag{2.40}$$

The total radiation power is given by

$$W = \frac{\omega k^3\epsilon_2}{12\pi}|\alpha|^2\,E_0^2, \tag{2.41}$$

while the energy density of the external field is

$$\bar{S_0} = \frac{\omega\epsilon_2}{2k}E_0^2. \tag{2.42}$$

This finally leads to the scattering cross-section, which is given by

$$\sigma_{sca} = \frac{W}{\bar{S}_0} = \frac{k^4}{6\pi}\left|\alpha\,(\omega)\right|^2. \tag{2.43}$$

However, power is not only removed from the incident beam due to scattering, but also due to absorption, which together make up the extinction. The power dissipated

by a point dipole is given by Poynting's theorem and is

$$P_{abs} = \left(\frac{\omega}{2}\right) \mathrm{Im}\left[\vec{p} \cdot \vec{E}_0^*\right]. \tag{2.44}$$

This gives rise to the absorption cross-section of

$$\sigma_{abs} = \frac{k}{\epsilon_0} \mathrm{Im}\left[\alpha\left(\omega\right)\right] \tag{2.45}$$

From equations 2.43 and 2.45 one can see, that σ_{sca} scales with a^6, while σ_{abs} scales with a^3. This means, that for large particles scattering dominates the extinction, while for smaller particles it is dominated by absorption. Furthermore, one can see that the plasmon frequency is dependent on the dielectric functions ϵ_1 and ϵ_2. This is the reason for the use of plasmonic structures as refractive index sensors.

2.2 Polarisation

Since the driving of the Yagi-Uda-antennas as well as the excitation of the core-satellite structures is dependent on the polarisation of the used light, an introduction is given on different polarisations and how to manipulate it. The chapter is following the book *Optik* by Eugene Hecht [74].
The polarisation of electromagnetic waves describes the direction of the electric field vector and its change in time. If the electric field vector oscillates in a plane, it is called linear polarisation (see upper half of figure 2.4). If the electric field vector has a constant value, but is rotating around the direction of propagation $\vec{k}$, it is called circular polarisation (see lower half of figure 2.4). A combination of both is possible and leads to an elliptical projection of the electric field vector and is therefore called elliptical polarisation. Stochastic distribution of the electric field vector is unpolarised light.

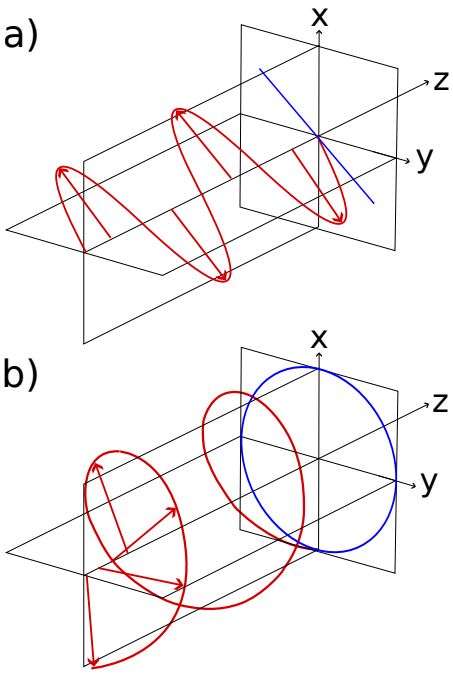

Figure 2.4: a) Linearly polarised light, with an electric field vector oscillating in a fixed plane. The blue line represents the accumulated path of movement of the electric field vector. b) Circularly polarised light, with an electric field vector rotating around the direction of propagation. The blue circle represents the accumulated path of movement of the electric field vector. Adapted from [74].

It is possible to convert unpolarised light to linearly polarised light with the help of a polarisation filter. To understand how this and later transformations of one polarisation into another work, it helps to look at all polarisations in a base of two linearly polarised waves with different amplitudes and phases between them. Without loss of generality, let these polarisation axes be the x- and y-axis.

To polarise unpolarised light, several effects are possible to use, such as birefringence, dichroism and reflection [74]. One technique, which uses reflection, is a wire-grid polariser consisting of parallel conductive rods for electromagnetic waves with wavelengths in the macroscopic range. The optical counterpart are thin polyvinyl alcohol films consisting of polymer chains which are doped with iodine so that they are conductive (such as so-called H-sheets invented by Edwin Herbert Land [84]).
When unpolarised light falls onto such a (microscopic) grid, the part that is polarised parallel to the grid lines is exciting motion of the valence electrons along these chains. The electrons are mostly dissipating the energy which was put into the system by the light, resulting in a heating of the material and an absorption of the light with parallel polarisation. Light which is polarised perpendicular to the chains cannot excite a meaningful motion of electrons along the width and is therefore passing through undisturbed. The result is polarised light behind the filter. The filter described above is generally a broadband filter.

It is also possible to manipulate the polarisation of light, for example to change the plane in which polarised light oscillates, or change linear polarisation to circular polarisation. To do so, so-called wave plates are used. The wave plates are made from a birefringent material, typically crystals, which are optically anisotrope and have two different refractive indices for light that is linearly polarised along or perpendicular to a certain crystal axis.
The axis of the crystal with high propagation velocity is called the fast axis, has the refractive index n_{fast} and is in this example along the y-axis. The slow axis is perpendicular to that and has the refractive index n_{slow}. Let's assume polarised light with an angle of 45° to the y-axis. This light can be described as a superposition of two electromagnetic waves of the same amplitude without a phase difference, which are oscillating in the x- respectively y-plane. Due to the different refractive indices, which the two waves experience, the waves will have a phase difference of

$$\Delta\varphi = \frac{2\pi}{\lambda_0} \cdot d \cdot (n_{slow} - n_{fast}) \tag{2.46}$$

after passing the crystal. d is the thickness of the plate and λ_0 the vacuum wave length.
Depending on the phase difference $\Delta\varphi$, one differentiates between quarter- and half-wave plates. Is d chosen in a way that $\Delta\varphi = \pi/2$, one obtains a quarter wave plate. For linearly polarised light with a 45° angle to the fast crystal axis as described above, the polarisation changes to circular polarisation. For other angles, the polarisation changes to an elliptical one.
Is d chosen in a way that $\Delta\varphi = \pi$, one obtains a half-wave plate. Is the angle between polarisation and fast axis at the entrance α, it has an angle of $-\alpha$ at the exit. This wave plate can be used to manipulate the polarisation plane of linearly polarised light.
In this work, a linear polarisation filter is used to polarise the unpolarised light of the microscope light source in darkfield measurements. By rotating the filter, core-satellite structures can be excited along different axis. Additionally, a half-wave plate is used to change the orientation of the linearly polarised laser light to ecxite the long and short axis of Yagi-Uda-antennas as well as a quarter-wave plate to change the

linear polarisation to a circular polarisation for particles of unknown orientation.

2.3 Yagi-Uda-antennas

The Yagi-Uda-antenna design was invented in the early 1920s by Shintaro Uda at the Tohoku Imperial University in Japan [85]. A later article with smaller contributions was published in 1928 by Hidetsugu Yagi in English, which gained wider circulation. This is the reason why the antenna is often referred to as Yagi-antenna in English literature.
The design was (and still is partially) immensely popular as radar and television antennas in radio frequency. In the following sections, its basic working mechanism is explained, followed by a look at how things change when going from radio frequency into the optical regime. However, before that some basic metrics, which can be used to characterise an antenna, will be introduced.

2.3.1 Antenna Metrics

Directivity

The directivity of an antenna is a parameter, that gives rise to how concentrated the emitted radiation power is into a single direction [86]. The angular radiation power or radiation pattern $\mathrm{p}(\theta, \varphi)$ is defined as

$$\int_0^{\pi} \int_0^{2\pi} \mathrm{p}(\theta, \varphi) \sin\theta \mathrm{d}\varphi \mathrm{d}\theta = \mathrm{P}_{\mathrm{rad,tot}}, \tag{2.47}$$

with $\mathrm{P}_{\mathrm{rad,tot}}$ being the sum of radiated power. The directivity is then defined as the ratio of angular radiation power to a hypothetical isotropic radiator. The directivity $\mathrm{D}(\theta, \varphi)$ is given by:

$$\mathrm{D}(\theta, \varphi) = \frac{4\pi}{\mathrm{P}_{\mathrm{rad,tot}}} \mathrm{p}(\theta, \varphi). \tag{2.48}$$

If the direction (θ, φ) is not explicitly given, normally the direction of the maximum is referred to

$$\mathrm{D}_{\mathrm{max}} = \frac{4\pi}{\mathrm{P}_{\mathrm{rad,tot}}} \mathrm{Max}\left[\mathrm{p}(\theta, \varphi)\right]. \tag{2.49}$$

Gain

The gain of an antenna is closely related to the directivity. However, additional to the directional capabilities, the efficiency of the antennas is taken into account as well.

Therefore, the gain G is defined as

$$G = \frac{4\pi}{P_{tot}} p(\theta, \varphi) = \epsilon_{rad} D, \tag{2.50}$$

where P_{tot} is the total power, that is inserted into the antenna system and ϵ_{rad} is the radiation efficiency, which gives rise to how well an antenna converts the input power into radiated power [87].

Front-to-back ratio

The front-to-back ratio (f/b ratio) of an antenna compares the antenna gain of one direction to the gain of the direction opposite or direction turned by 180° from the specified azimuthal angle. Typically, the angle of maximum emission is used if not stated otherwise.

2.3.2 Radio frequency

A Yagi-Uda-antenna contains several elements: a driven element and several parasitic/passive elements, which are responsible for the beam formation. The driven element, also called the feed, is typically resonant with a length slightly shorter than $\lambda/2$ (typically 0,45-0,49λ). The directors are passive elements, which are parallel to the feed and, as the name suggests, are directing the radiation of the feed (see figure 2.5). These elements are usually a bit shorter than the feed and of the length of 0,4 to 0,45λ. The separation amongst the directors and between the feed is usually 0,3 to 0,4λ. It is however not necessary, that either the length or the spacing between the elements has to be uniform for an optimal design.

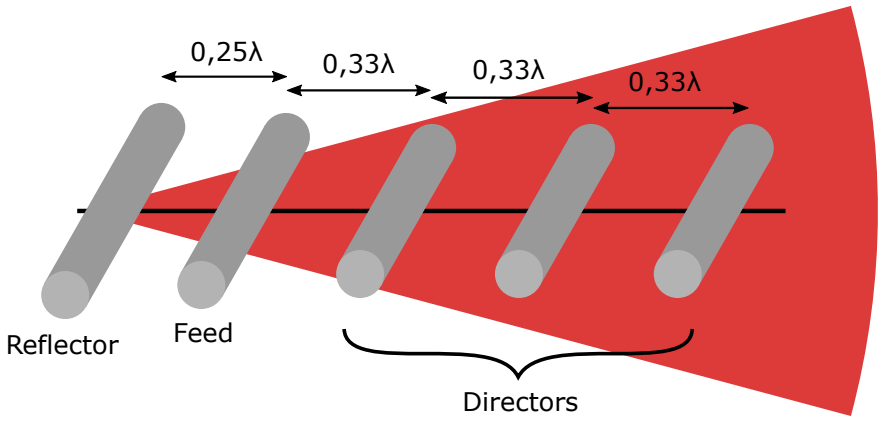

Figure 2.5: Sketch of a Yagi-Uda-antenna. The feed element is the only actively driven element while reflector and directors are designed and placed in such a way that a directed emission is ensured. Adapted from [29].

The last element of such an antenna is the reflector. It is also placed parallel to the feed, but opposed to the directors and is supposed to reflect radiation of the feed in that direction, which again leads to an increase of directivity of the antenna. The reflector is a bit larger than the feed, while its distance to the feed is shorter than that of the directors, with around $0{,}25\lambda$.
The aforementioned dimensions of the passive elements have two major effects. Firstly, due to the length of the reflector being longer than that of the feed, the element will have an inductive reactance, which means, that the phase of the current lags behind the one of the induced electromagnetic field. Similarly, due to the length of the director being smaller than the one of the feed, it has a capacitive reactance, which means, that the phase of the current leads the one of the electromagnetic field.
Secondly, the spacing between the feed and the passive elements influences the total phase difference of the currents in these elements. If the spacing and length/reactance of the director elements is chosen accordingly, the electromagnetic waves emitted by the feed and re-emitted by the directors all reach the front of the antenna in phase. This leads to a constructive interference of these waves and an increase of signal strength in the forward direction.
Similarly, the phase difference of the wave emitted by the feed and re-emitted by the reflector is around π in the backwards direction. This leads to a destructive interference and near-cancelling of the signal in this direction (see figure 2.6).

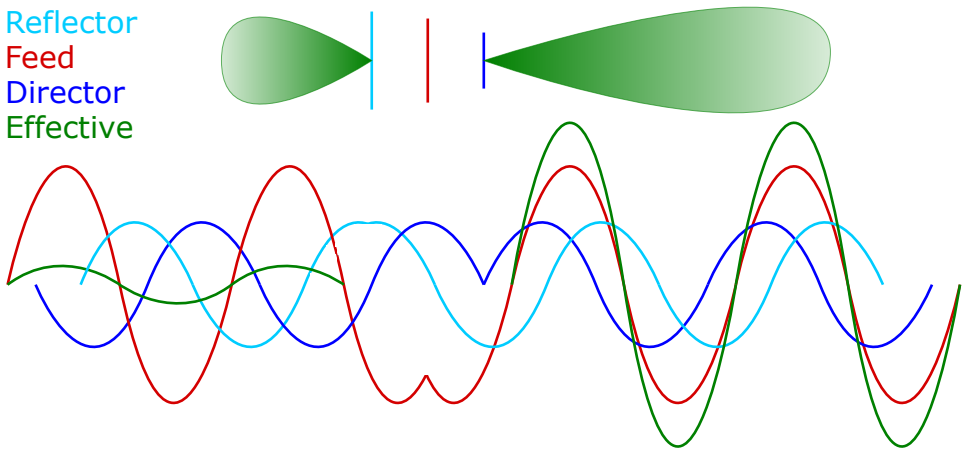

Figure 2.6: The emitted electromagnetic waves of the feed and the re-emitted waves of the parasitic elements interfere in such a way, that the signal is increased forwards, in the direction of the directors and decreased backwards, in the direction of the reflector. Adapted from [88].

In practice, most antennas consist of one reflector element, because already the second element is only very weakly driven due to the destructive interference of the waves from the feed and first reflector element. The contribution of the second element would therefore be very weak.
For directors however, the improvements are considerable for more elements, how-

ever the number of director elements is capped by the decrease of the induced currents of the further elements. Typical numbers are 6 to 12 directors, which can achieve gains (relative to a lossless isotropic source) between 30 and 54 (14,8 – 17,3 dB) [85].
Among the reflector-feed arrangement, the feed itself and the size and spacing of the directors, the latter is deemed as the most critical with the highest effect on forward gain, backward gain, and input impedance.

2.3.3 Optical

Generally, Maxwell's equations are scale invariant in vacuum and therefore independent of the wavelength. However, this changes for frequency dependent properties of matter. Metals generally cannot be seen as perfect conductors at optical frequencies, and electromagnetic fields fully penetrate the particles rather than just induce surface currents [85]. This coincides well with the assumptions of the quasi-static approach mentioned above, which has the effect, that for such small particles the role of electromagnetic induction is taken over by the effective mass of the free electrons of the plasmon oscillation. In conventional antennas positive polarizability is associated with a capacitive effect, however at optical frequencies the negative real part of the dielectric constant turns this into an inductive effect [89]. This additional inductivity leads to antenna elements in the optical regime which are smaller than half the wavelength in size, opposed to their radio frequency counterparts.
A further reduction in size leads to even higher inductive effects due to the negative dielectric constant. As a result, the magnetic induction becomes relatively small, and plasma resonances become largely independent of particle size.
Similar to chapter 2.3, a quasi-static response with the neglection of the magnetic induction can be used as a model to calculate the polarization $\vec{P}$ of a nanoparticle. The incoming electric field is $\vec{E}$, and the response to that can be described in three separate parts: the response of the material inside the particle dependent on the complex dielectric constant $\epsilon_{part} = \epsilon_r \epsilon_{med}$, the field of the surface charges on the border between particle and the medium (which are dependent on the shape of said border), and the radiation damping field from the dipole emission with dipole $\vec{d} = \vec{P}V$ with V being the volume of the particle. According to [19] the incoming field polarizes the particle as follows:

$$\vec{E} = \frac{1}{(\epsilon_r - 1)\,\epsilon_{med}}\vec{P} + \frac{N}{\epsilon_{med}}\vec{P} - i\frac{4\pi^2 V}{3\epsilon_{med}\lambda^3}\vec{P}. \tag{2.51}$$

The depolarisation factor N describes the capacitive effect of surface charges and is an analogy to the demagnetization factor which describes the weakening of the electric field $\vec{E}$ due to the polarization $\vec{P}$.
The first term in equation 2.51 corresponds to the inductive effect of the material, the second term to the capacitive effects due to the shape of the particle, and the third term corresponds to radiation losses and can be seen as an effective resistance of the

particle. Solving equation 2.51 for $\vec{P}$ gives the following form:

$$\vec{P} = \frac{(\epsilon_r - 1)\,\epsilon_{med}\vec{E}}{1 + N\,(\epsilon_r - 1) - i\,(\epsilon_r - 1)\,R}, \quad \text{with} \quad R = \frac{4\pi^2 V}{3\lambda^3}. \tag{2.52}$$

From the equation above one can identify the parameter for relative losses γ and effective detuning δ depending on the dielectric constant $\epsilon_r = \epsilon_{part}/\epsilon_{med}$, its volume V and depolarization factor N. The parameters are:

$$\gamma = \frac{\mathrm{Im}\,(\epsilon_r)}{R\,|\epsilon_r - 1|^2}, \tag{2.53}$$

$$\delta = \frac{1}{R}\left(N + \frac{\mathrm{Re}\,(\epsilon_r - 1)}{|\epsilon_r - 1|^2}\right). \tag{2.54}$$

Absorption losses pose the main limiting factor for optical nano-antennas. According to equation 2.53 the main influence on these losses are material properties (represented by $\mathrm{Im}\,(\epsilon_r)$) and the volume of the nanoparticle. This way, absorption losses of the material can be compensated by increasing the volume of the particle. As a good starting point for antenna design, parameters (especially the volume/geometry, since the material selection is very limited) should be chosen, so that the loss parameter γ is one or lower. For the properties of gold in glass, the antennas should be around the order of a tenth of the wavelength inside the medium (here glass).
For a fixed size of the first element, the detuning of the other elements can be determined. Equation 2.54 shows the relation between the detuning δ and the depolarization factor N, which can be adjusted by varying the ratio between a and b, the dimensions parallel and perpendicular to the electric field respectively. In [90] the depolarization factor is analytically calculated for some simple geometries. With that, the dielectric constants of gold for different frequencies from [91], and a dielectric constant of glass $\epsilon_{med} = 2,3$ one can calculate the size of a nanoparticle, which can be used to construct an antenna.
For an elliptical particle with aspect ratio of 2,76 at its resonance wavelength of 705 nm a loss parameter of $\gamma = 0,5$ is obtained for a length of $2a = 115\,\mathrm{nm}$ [19]. For the director elements of a Yagi-Uda-antenna with the above-mentioned element as a feed, the detuning parameters have to be controlled. As can be seen in equation 2.54, a change in depolarization factor ΔN results in a detuning of $\delta = \Delta N/R$. To detune the feed element operating at 705 nm with a loss of $\gamma = 0,5$ to $\delta = 1$, one has to increase the depolarization factor to $N_1 = N_0 + R = 0,136$ with $N_0 = 0,120$ and $R = 0,016$. For ellipsoids, this corresponds to an aspect ratio of 2,5. For the volume corresponding to losses of $\gamma = 0,5$ at 705 nm, one obtains a length of $2a = 107\,\mathrm{nm}$ of the ellipsoid. So a reduction in length of around 7% corresponds to an increase of the detuning δ of one [19].
These analytical calculations can be used as a starting point for numerical calculations and simulations of optical Yagi-Uda-antennas.

2.4 Back Focal Plane Microscopy

In normal microscopy it is possible to retrieve information about position and size of an object, or generally speaking: spatial information. However, it is sometimes of advantage to obtain information which is encoded in the wave vector. Such information can be the periodicity of a grating below the refraction limit [92], the orientation of a single molecule [93] or the radiation pattern of a nanoparticle antenna [94]. Due to this variety of applications, *back focal plane* (BFP) microscopy, which grants access to this information, became of growing interest in general and specifically in plasmonics [95, 96].

To access this information, one has to look at how lenses (including microscope objectives) work. Every microscope objective is characterised by the Numerical Aperture (NA), which is given by NA=n $\sin(\phi)$, where n is the refractive index of the medium between object and objective and ϕ is half the opening angle of the light which can enter the microscope. An object is normally placed in the focus of the objective (so one focal length f_{obj} away). The sample emits (scattered) light from every point in the sample plane f(x,y) under different angles θ_i, which is the angle relative to the optical axis. This light can be thought of in the far-field as plane waves $u_i(x,y)$. So, the light arriving at the objective lens can be described as the weighted sum of these plane waves. Upon passing the objective lens, the composite light gets separated again and gets transformed by the bi-convex lens into paraboloidal waves, which focus on one point in the back focal plane. This way, any plane wave $u_i(x,y)$ leaving the sample under the angle $\left(\theta_{x,i}, \theta_{y,i}\right)$ gets mapped onto a single point $g\left(\theta_{x,i} f_{obj}, \theta_{y,i} f_{obj}\right)$ in the BFP [97]. Now, the angular distribution of the light emitted by the sample can be recorded.

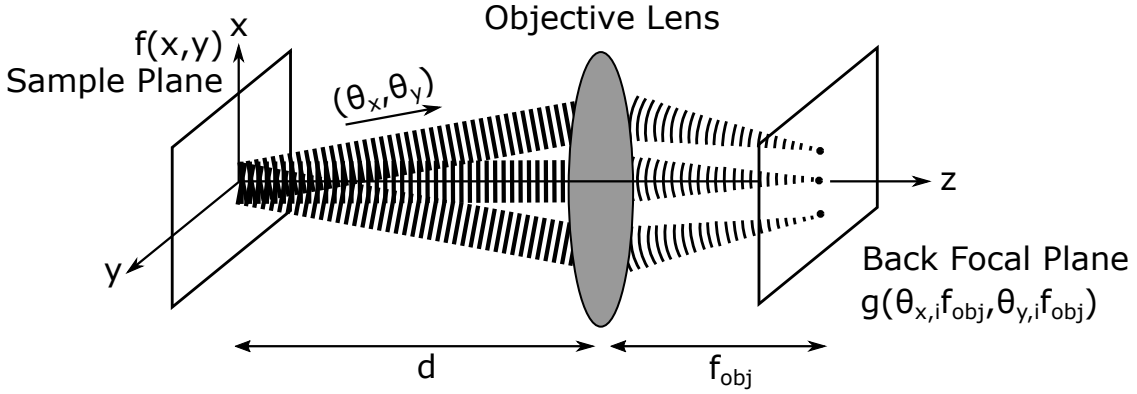

Figure 2.7: Scheme of the light path for acquiring a BFP image. The objective lens is placed a distance d away from the sample plane $f(x,y)$ and one focal length f_{obj} away from the back focal (Fourier) plane $g\left(\theta_{x,i} f_{obj}, \theta_{y,i} f_{obj}\right)$. Plane waves $u_i(x,y)$ emitted by the sample under angle $\left(\theta_{x,i}, \theta_{y,i}\right)$ are collected by the objective lens onto the same spot in the back focal plane. The objective forms a Fourier transformation of the light and contains angular information. Due to the casing of the objective lens, the BFP is not directly accessible and must therefore be projected with a second lens, the Bertrand lens. Adapted from [98].

While information from the BFP is given in angular coordinates, each point in the BFP is associated with a wave vector $\vec{k}$ of the scattered light. Due to the transformation of information from the real space with units of length to the momentum space with reciprocal units of length, one can say that this process is a Fourier transformation. The BFP is therefore also called the Fourier plane [99, 100].
Several limitations arise to the BFP microscopy. For once, it is only possible to observe one half space of the emission/scattering of light. This gets even further reduced, since in practice only angles smaller than the maximum half-angle of the microscope objective can be observed. High NA (oil) objectives are therefore best fitted for BFP imaging.
A further problem is, that for any given microscope objective the BFP is inside the metal casing, which makes a direct projection impossible. A second lens, the Bertrand lens, is therefore introduced, which images the BFP onto the eventual detector [101]. Moreover, it should be noted that modern objectives are infinity corrected, meaning that the light leaving the objective is collimated. The advantage is to place further objectives into the light path, before refocusing the parallel light with a tube lens. This means, that in infinity corrected systems one does not image the Fourier plane, but rather the back-aperture plane [93].
A detailed description of the setup used for this work can be found in chapter 3.2.

2.5 Radiation Pattern of Dipoles near Interfaces

The radiation of a dipole in a homogeneous medium is well understood and only depends on the emitter properties. The radiation pattern is radially symmetric around the axis of the dipole moment $\vec{p}$. The highest intensity is emitted perpendicular to the dipole axis and follows a $\sin^2\theta$ distribution, where θ is the angle between dipole and observation direction [73].

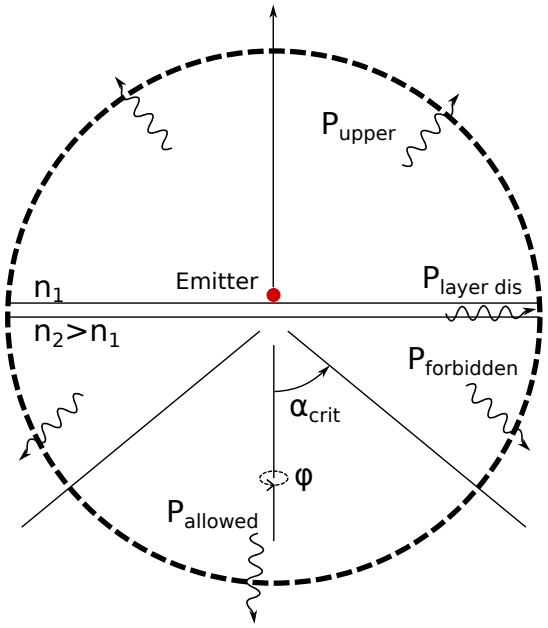

Figure 2.8: Scheme of the radiated power of an emitter close to the interface of two dielectric media. The refractive index of the lower half n_2 is higher than that of the upper half n_1. The total emitted power P_{tot} is emitted via several channels: the dissipated power along the surface $P_{layerdis}$, radiation into the upper half P_{upper}, radiation into the 'forbidden' zone $P_{forbidden}$ with $\alpha > \alpha_{crit}$ and into the 'allowed' zone $P_{allowed}$ with $\alpha < \alpha_{crit}$. Adapted from [75].

However, this pattern changes when the dipole is close to or on a dielectric surface with refractive index n_2, while itself it is in a medium of refractive index $n_1 < n_2$. As can be seen in figure 2.8, the total emitted power P_{tot} is not distributed symmetrically around the dipole, but divided into radiation into the upper half P_{upper}, the power dissipated along the surface $P_{surface}$, the allowed zone of the lower half $P_{allowed}$ with angles smaller than the critical angle $\alpha < \alpha_{crit} = \arcsin(n_1/n_2)$ and the forbidden zone of the lower half $P_{forbidden}$ with $\alpha > \alpha_{crit}$ (see figure 2.9) [75].

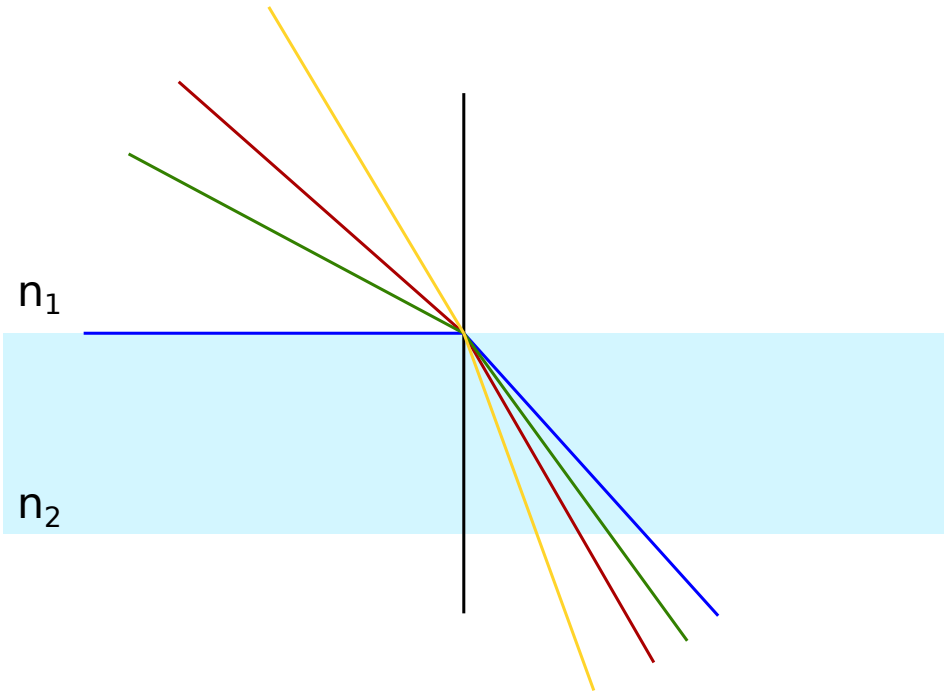

Figure 2.9: Beam paths of light coming from the upper half with small refractive index n_1 going into the lower half with larger refractive index n_2. According to Snell's law, the beam is refracted towards the surface normal. In the limiting case of the beam coming in parallel to the boundary, it would be refracted onto the critical angle α_{crit} (blue beam path).
In this classical picture, it is not possible to find an angle of illumination in the upper half, that corresponds to a beam in the lower half that has an angle $\alpha > \alpha_{crit}$. The area with $\alpha > \alpha_{crit}$ in the lower half is therefore called the forbidden zone.

For light from an emitter far away from the surface the zone is forbidden, because according to Snell's law incoming light that refracts into that zone has to have a complex value:

$$\alpha_{incoming} = \arcsin\left(\frac{n_2}{n_1}\sin(\alpha)\right). \tag{2.55}$$

No classical beam path is possible for illumination of areas in the lower half with $\alpha > \alpha_{crit}$.
This changes for an emitter placed directly or in close vicinity of a surface. The situation describes now the setup of an inverted microscope with a high NA oil objective with nanostructures on top of a glass microscope cover slip, as is the case for a majority of measurements performed in this work. Due to the high NA of the objective and the emitted positioned on the glass cover slip, radiation into the allowed zone of the lower half $P_{allowed}$ as well as parts of the radiation into the forbidden zone of the lower half $P_{forbidden}$ can be observed.

For the calculation of the intensity distribution in the BFP as a function of α, the Weyl

representation can be applied. There, the spherical waves emitted by the dipole are decomposed and represented as a superposition of a planar and an evanescent wave [102]. Additionally, one has to look at the projection of the emission onto the BFP of a microscope objective. While the same angle $d\alpha$ is always projected onto the same arc ds (with $s = R \cdot \alpha$) and therefore would correctly represent the power radiated into that direction, this holds not true for the projection onto the BFP plane. For a length in the BFP plane the projection $dr = ds\cos\alpha$ has to be applied, meaning that for higher angles of α, the power gets projected on decreasing sections dr. To account for this, the correction factor of $1/\cos\alpha$ is introduced, which also ensures conservation of energy [103]. The intensity distribution in the BFP generated by the emitter $\vec{E}_{emitter}$ is now:

$$I_{BFP} \propto \frac{1}{\cos\alpha} \left|\vec{E}_{emitter}\right|^2 . \tag{2.56}$$

2.6 Calculation of dipole emission near planar interface

To understand the back focal plane (BFP) images, which are taken throughout this work, one has to understand the emission of dipoles near a planar surface. First theories were developed as early as 1909 by Sommerfeld [104] for radiating dipoles vertically orientated on a planar and lossy ground. Later, the problem was expanded by a superposition of plane waves and evanescent waves [102, 105, 106]. First experimental observations were reported by Lukosz and Meier in 1981 [107]. The explanations of the topic given here are mostly based on [93, 75, 108, 109].
To understand the following calculations better, the geometry of the described situation is shown in figure 2.10. A point-dipole emitter $\vec{p}$ is placed in the centre of the optical axis (but with potentially variable height) and has an orientation given by the angles Φ and Θ. The incident angle θ_S of light that corresponds to an emission angle of θ is given by Snell's law:

$$\theta_S = \text{arscin}\left(\frac{n_2 \sin\theta}{n_1}\right). \tag{2.57}$$

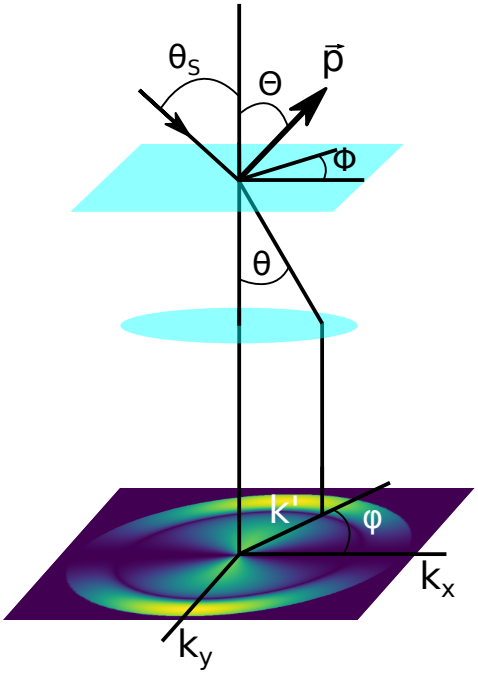

Figure 2.10: Scheme of the geometry, that is used to derive the calculation of the BFP of an emitter placed on the surface of a planar interface. The dipole $\vec{p}$ is oriented along angles Φ and Θ and its emission into direction θ will be detected at position (k', φ). Adapted from [93].

Complex values for the incident angle θ_S are allowed (which is crucial for the forbidden zone). The collected light is projected onto the BFP, and its position there is

given by the momentum k' and the azimuthal angle φ. The wave number of the incident light is $k_0 = 2\pi/\lambda$ The relation between the emission angle θ and the k-vector coordinate in the BFP is:

$$\left|k'\right| = 2\pi\frac{n_2}{\lambda}\sin\theta = k_0 n_2 \sin\theta \tag{2.58}$$

$$\begin{pmatrix} k'_x \\ k'_y \end{pmatrix} = \begin{pmatrix} \cos\varphi \\ \sin\varphi \end{pmatrix} \cdot \left|k'\right|. \tag{2.59}$$

Following equation 2.56, one can split up the emitted power into a parallel and perpendicular field component and obtains

$$I_{\text{dipole}}(\theta,\varphi) \propto \frac{1}{\cos\theta}\left(E_p E_p^* + E_s E_s^*\right), \tag{2.60}$$

where * indicates the complex conjugated and E_p and E_s are

$$E_p = c_1(\theta)\cos\Theta\sin\theta + c_2(\theta)\sin\Theta\cos\theta\cos(\varphi - \Phi) \tag{2.61}$$

$$E_s = c_3(\theta)\cos\Theta\sin(\varphi - \Phi). \tag{2.62}$$

The different c coefficients are

$$c_1(\theta) = n^2\frac{\cos\theta}{\cos\theta_S}t^p(\theta_S)\,\Pi(\theta_S), \tag{2.63}$$

$$c_2(\theta) = n t^p(\theta_S)\,\Pi(\theta_S), \tag{2.64}$$

$$c_3(\theta) = -n\frac{\cos\theta}{\cos\theta_S}t^s(\theta_S)\,\Pi(\theta_S), \tag{2.65}$$

with

$$\Pi(\theta_S) = \exp\left(-ik_0 n_1 \cos(\theta_S)\,\delta\right), \tag{2.66}$$

where $n = n_2/n_1$ is the relative refractive index between upper and lower half. Π corrects for the distance of the emitter from the surface given by δ, and t^p and t^s are the Fresnel transmission coefficients for p- and s-polarised light respectively:

$$t^p = \frac{2n_1\cos\theta_S}{n_1\cos\theta + n_2\cos\theta_S}, \tag{2.67}$$

$$t^s = \frac{2n_1\cos\theta_S}{n_1\cos\theta_S + n_2\cos\theta}. \tag{2.68}$$

In figure 2.11, the calculated BFP pattern of a dipole oriented along the x-axis ($\Theta = 90°$, $\Phi = 0°$) can be seen. The calculation used a refractive index of n=1,52 for the substrate (which is typical for glass cover slips [110]) and n=1 for air. As microscope objective, an oil objective with NA=1,4 was assumed. The BFP was calculated with normalized wave vector components k_x/k_0 and k_y/k_0. To give respect to the detection limit of the objective, only values for $k_x^2/k_0^2 + k_y^2/k_0^2 \leq NA^2 = 1,4^2$ were taken into account.
Several things can be seen immediately. There is a discontinuity between the inner

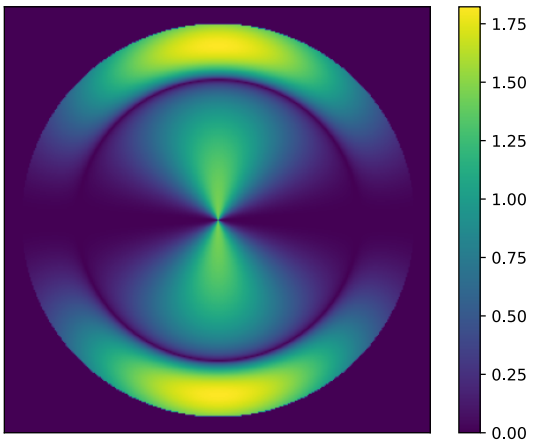

Figure 2.11: Calculated emission pattern of a dipole oriented along the x-axis ($\Theta = 90°, \Phi = 0°$) in the BFP. An objective of NA=1,4 was assumed for calculations.

and outer region. This inner ring corresponds to the critical angle of total internal reflection at the air-glass interface [93]. The edge of the outer ring is limited by the NA of the aperture. Furthermore, two bright spots can be seen in the region of the forbidden light. These spots do not only represent the maximum of emission, but also is the integrated intensity of the outer region exceeding that of the inner region, the allowed region.

2.7 Finite Difference Time Domain Simulations

Simulations of different nanostructures have been carried out through the course of this work. This was done to either determine the dimensions of the nano structure, which was then fabricated after the simulated blueprint, or structures were already given and simulations were carried out to understand the plasmonic nature of the structures.
The ultimate goal of all simulation techniques is to (numerically) solve the Maxwell equations for a given structure and its dielectric function. To do so, multiple approaches are possible, however here the so-called *finite difference time domain* (FDTD) approach was used. The method was first developed by Kane S. Yee in 1966 [111]. In contrast to other methods (which were used before and are still used), the FDTD method does not solve Maxwell's equations in the frequency domain, but rather (as the name suggests) in the time domain. All electrical and magnetic fields are calculated for each time step t_1, t_2, t_3..., instead of finding a steady state solution.
The following explanations are based on [112]. Yee's idea was to base the calculation only on the time-dependent Maxwell's curl equations, which were slightly adapted by a fictive magnetic charge current density $\vec{J}_B$:

$$\frac{\partial \vec{H}}{\partial t} = -\frac{1}{\mu}\nabla \times \vec{E} - \frac{1}{\mu}\vec{J}_B \tag{2.69}$$

$$\frac{\partial \vec{E}}{\partial t} = \frac{1}{\epsilon}\nabla \times \vec{H} - \frac{1}{\epsilon}\vec{J}. \tag{2.70}$$

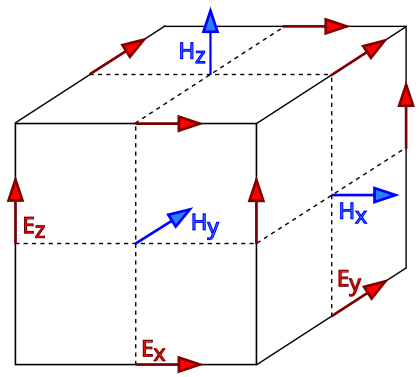

Figure 2.12: Scheme of a cubic unit cell of a Yee space lattice. The position of the electric and magnetic field vector components are arranged in a way, so that each $\vec{E}$ component is surrounded by four circulating $\vec{H}$ components and vice versa.

The Yee algorithm then solves due to the coupling of Maxwell's curl equation for both the electric and magnetic field in time and space, instead of just one of them with a wave equation. An upside of that is a more robust solution, while unique features of each field can be modelled if both fields are available.

To solve the equations, a Yee space lattice is used, which can be seen in figure 2.12. The algorithm does not calculate $\vec{E}$ and $\vec{H}$ at the same time and the same position. Instead, $\vec{E}$ and $\vec{H}$ are separated into their Cartesian components. The components are placed in such a way, that each $\vec{E}$ component is surrounded by four circulating $\vec{H}$ components and vice versa. This way, the three-dimensional space is filled by an array of interconnected contours of Faraday's and Ampere's law.
In time, the calculation is done by staggering the calculations for the $\vec{E}$ and $\vec{H}$ field. First, all the $\vec{E}$ components are calculated for the Yee space lattice and are stored in memory. Then, the $\vec{H}$ components are calculated based on the $\vec{E}$ component data, which was just stored in the memory. After storing the $\vec{H}$ component data, one cycle is completed and a new one begins until the simulation time frame is completed. This computation technique is called leapfrog arrangement and is depicted in figure 2.13.

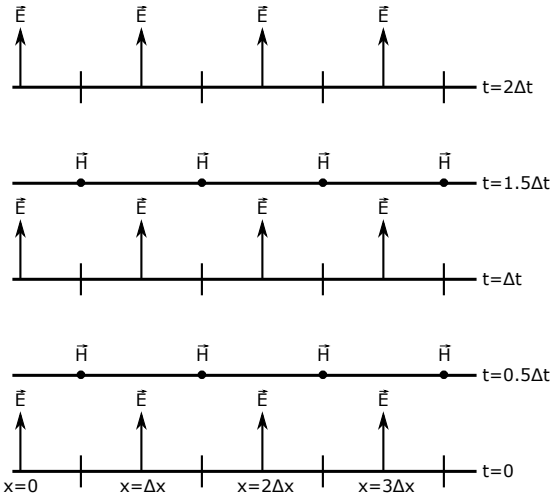

Figure 2.13: Scheme of a one-dimensional leapfrog array. Adapted from [112]

This method has several advantages. Firstly, the leapfrog method is fully explicit and can therefore avoid algebraic problems like matrix inversions, which are load intensive and error-prone [113]. Secondly, the time-stepping algorithm is non-dissipative, meaning that wave modes do not falsely decay on non-physical artefacts.
The exact simulation setups adjusted to the different needs are discussed in the results section.

2.8 Nonlinear properties

In this work, measurements were carried out on Yagi-Uda-antennas in a parabolic mirror setup. This setup allows for work with pulsed lasers, which can achieve high peak intensities. With such high intensities and therefore high electric fields new phenomena arise. The following chapter gives an introduction to such phenomena.

For low intensities the relation between light and polarisation is linear as can be seen in equation 2.15. The electric field acts on the outer and valence electrons, and the resulting polarisation is parallel and directly proportional to the external field strength. This is also true for harmonic external fields. However, this is not the case any more for very high intensities. The polarisation P can not continue to grow indefinitely with increasing E. Nonlinear effects have to come into play, which are negligible for low intensities but dominate for high intensities [74].
In case of an isotropic medium, and P parallel to E, the polarisation can be developed in a series:

$$P = \epsilon_0 \left(\chi E + \chi_2 E^2 + \chi_3 E^3 + \dots \right). \tag{2.71}$$

Here, χ is noticeably greater than χ_2, χ_3, etc. The medium is now illuminated by a field

$$E = E_0 \sin(\omega t). \tag{2.72}$$

The response to that is (with the help of trigonometric/Pythagorean identities):

$$P = \epsilon_0 \chi E_0 \sin(\omega t) + \frac{\epsilon_0 \chi_2}{2} E_0^2 (1 - \cos(2\omega t)) + \frac{\epsilon_0 \chi_3}{4} E_0^3 (3\sin(\omega t) - \sin(3\omega t)) + \dots. \tag{2.73}$$

The meaning of the different terms in equation 2.73 will be discussed in the following section.

2.8.1 Second Harmonic Generation

If one has a closer look at the second term of equation 2.73, one can see two things: a constant polarisation and a term with $\cos(2\omega t)$. The constant polarisation in the medium is proportional to E_0^2 and implies a constant voltage difference in the material. This term is called *optical rectification* [114].
The $\cos(2\omega t)$ term however means, that there is now a variation in polarisation with double the frequency as the incident light. The emitted light of all the oscillating electrons has now a frequency component of 2ω as well. This process is called *second harmonic generation* (SHG).
In the photon picture, one can say, that two photons of energy $\hbar\omega$ lead to the emission of one photon of energy $2\hbar\omega$.
Second harmonic generation is only possible, if the polarisation P in a material does not invert with an inverting E field. The even powers of the dielectric function in the

polarisation cannot be zero. This means, that the material can not be isotropic (like glass or water), and crystals can not have an inversion centre.
However, it is possible to observe the effect of surface SHG in these materials (normally in reflection), where broken symmetries at the surface are exploited for (surface sensitive) SHG measurements [115, 116, 117].
Additionally, SHG can be observed in nanostructures of centrosymmetric material. Here, the number of surface atoms to volume atoms increases and spacial inhomogeneities of the electromagnetic field have to be taken account for [118].

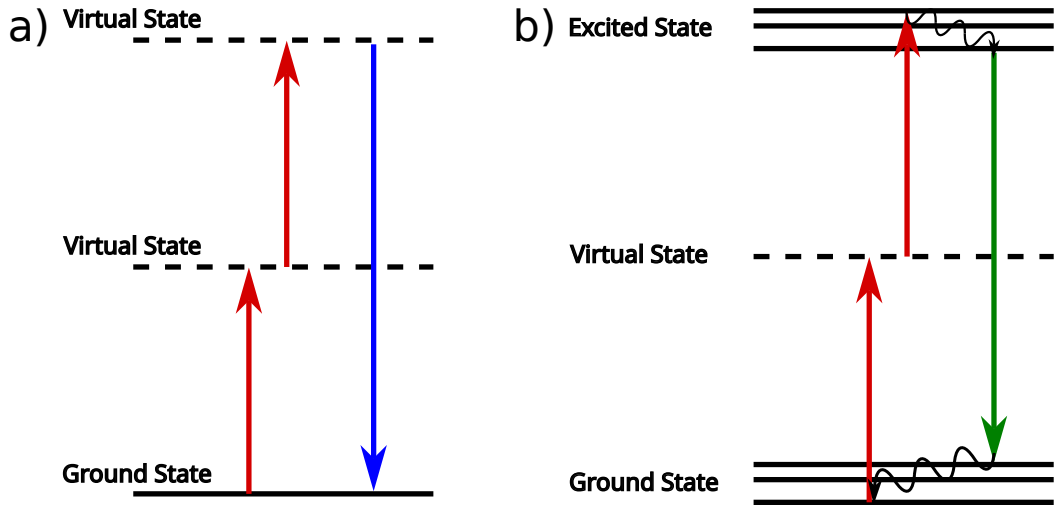

Figure 2.14: a) Second harmonic generation assisted by two virtual states. Two photons of frequency ω are combined in a single photon of frequency 2ω. b) Two-photon absorption assisted by a single virtual state. Since non-radiative relaxation processes happen at the ground and excited stage, the resulting photon typically has a frequency smaller than 2ω. In gold films, the spectrum is continuous due to the many different ground and excited states, which are non-degenerate due to rotational and vibrational modes.

2.8.2 Two-Photon Absorption

Two-photon absorption (TPA) was first theoretically predicted in 1931 by Maria Goeppert-Mayer and describes the simultaneous absorption of two photons to excite a system (typically from the ground state) to another excited state [119]. The frequencies of the exciting photons can be, but do not have to be the same, however the energy gap between ground and excited state is smaller or equal to the sum of the photon energies. The probability of a TPA is proportional to the square of light intensity and a third order process, which means it is dependent on χ_3 [120].
The fluorescence emission after the TPA is typically of lower energy than the sum of the exciting photons. The excited system first de-ecxites non-radiatively followed by a fluorescence emission and reaches the ground state typically after another non-radiative relaxation (see figure 2.14). Depending on the system, for example organic molecules, TPA and its photoluminescence can be used as a spectroscopy

method, however for gold films the spectrum is continuous due to many different ground and excited states, which are non-degenerate due to rotational and vibrational modes.

2.9 Raman spectroscopy

Raman spectroscopy [121, 122] is a technique commonly used to identify and characterise molecules and solids by their individual fingerprints. Its main advantages are, that it is non-destructive, offers structural and electronic information of the material and operates with high resolution. This leads to applications in various fields such as physics, chemistry and biology [123].
Raman scattering describes the inelastic scattering of photons in matter. This means, that the incident photon of frequency ω has a different frequency after the scattering event. This can happen, when said photon excites e.g. a molecule from its initial ground state to a higher virtual state. The photon gets absorbed during this process. When the molecule relaxes into a higher vibrational ground state, a new photon gets reemitted with frequency $\omega' = \omega - \omega_{\text{phon}}$, which is called the Stokes scattering. Since the system eventually has to return to a stationary state, a phonon of energy ω_{phon} is created. Analogously, if the molecule starts in a higher vibrational state, gets further excited into a virtual state and then relaxes into the ground state, a photon of energy $\omega' = \omega + \omega_{\text{phon}}$ is emitted. This process is called Anti-Stokes scattering [123, 124].
Since the probability of finding a molecule in the ground state is higher than that in a vibrational state, the majority of Raman spectra (as well as in this work) are Stokes scattering measurements.

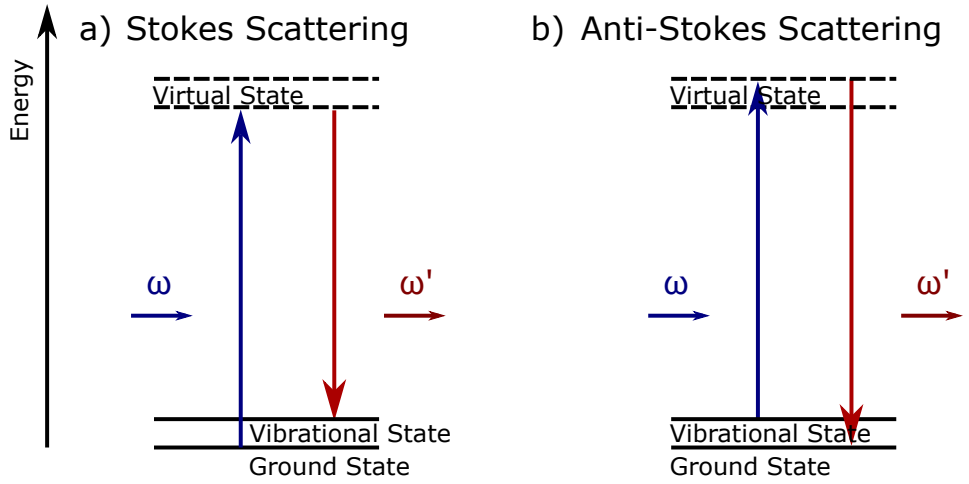

Figure 2.15: Energy level diagrams of inelastic Raman scattering. a) Stokes scattering: The system absorbs a part of the energy brought in by the photon and creates a phonon of energy $\omega_{\text{phon}} = \omega - \omega'$. b) Anti-Stokes scattering: The system loses energy in the form of a phonon and emits a photon with additional energy of $\omega_{\text{phon}} = \omega' - \omega$.

The intensity of the Raman signal is dependent on the induced electric dipole moment μ' generated by the incident electric field E_0 and the so-called derived polarisability α'_k (which is sometimes also called the Raman tensor). The derived polarisability "reflects the sensitivity of molecular polarizability to changes of nuclear configuration along the normal coordinate of vibration" [125]p.76.

This means that a higher probability of Raman scattering is achieved by increasing the electric dipole moment by either changing the derived polarisability or increasing the local (incident) field intensity E_0 [125]. This can be achieved by increasing laser intensity, however this method is limited by the measurement setup and can potentially destroy samples, since this also comes with an increased laser power. Another method is to exploit the increased local near-field in the vicinity of a plasmonic nanostructure [126, 127, 128].

To measure this enhancement of local field intensity, or rather the resulting higher Raman scattering probability, one can calculate the enhancement factor (EF). This factor is used to express the sensitivity of a SERS measurement, specifically the ratio of signal from a single molecule on a nanostructure compared to that of a molecule on an unstructured surface of the same material. The EF can be calculated with [14]:

$$EF = \frac{I_{SERS}}{I_{ref}} \cdot \frac{N_{ref}}{N_{SERS} \cdot n}. \tag{2.74}$$

In equation 2.74, I_{SERS} and I_{ref} are standing for the intensities measured on SERS structures and on the reference spot of unstructured material. Their ratio is the so-called relative EF (EF_{rel}). The number of molecules illuminated in the confocal area of the objective is denoted by N_{ref}, whereas N_{SERS} describes the number of molecules per nanostructure. The factor n corrects that number with the amount of nanostructures, that are present in the confocal area, to obtain the total amount of molecules affected by SERS.
This approach however has several disadvantages. For once, it is very hard to actually obtain the number of molecules per area (for the reference as well as the SERS structures). Additionally, it would be further assumed, that all molecules no matter where on the nanostructure experience enhancement. This is typically not the case, since most structures are specifically designed to achieve small areas of high field enhancements.
A more practical approach is therefore to assume homogeneous coating of all surfaces and compare the confocal area of the laser A_{laser} with the effective area of the nanostructure hotspots A_{eff} [14]. This approach leads to the effective EF (EF^*):

$$EF^* = EF_{rel} \cdot \frac{A_{laser}}{A_{eff} \cdot n}. \tag{2.75}$$

To calculate the confocal area of the laser A_{laser}, it is assumed that this area is circular. One can calculate with the Abbe diffraction limit (equation 2.76), the numerical aperture of the objective NA_{obj} and the laser wavelength λ_{laser} the diameter of the laser spot d_{laser}. With that knowledge and equation 2.77 the area of the laser can be calculated.

$$d_{laser} = \frac{0.61 \cdot \lambda_{laser}}{NA_{obj}} \tag{2.76}$$

$$A_{laser} = \frac{1}{4}\pi d_{laser}^2 \tag{2.77}$$

The effective area of the hotspot can be approximated with dimensions of the nanostructures acquired by SEM images or with the help of numerical simulations.

3 Measurement Setups

Several different measurements and experiments have been carried out for this work. Due to the varying nature of the measurements, several different setups have been used or built up. In the following chapters, some light is shed on the exact specifications of these setups and how they are used.

3.1 Dark-Field Microscopy and Spectroscopy

Most spectra are taken with an inverted microscope made by Nikon: the Eclipse Ti-S. A schematic overview of how the beam path looks can be seen on the left of figure 3.1.
The light path begins with a 100 W halogen light source, which is directed downwards towards the sample and objective. Before reaching the sample, a dark-field condenser cuts out the central beam path and reflects the outer beams in a cone with a tip in the objective plane towards the sample. The opening angle of that light cone is higher than the one corresponding to the Numerical Aperture (NA) of the objective which means, that no light reaches the objective, if it is not refracted on a sample structure. This leads to very high contrasts and also to the name of the dark-field microscope.
The refracted light gets collected by the objective and guided into the slit of a spectrometer, in this case the 'Shamrock 303i' by Andor Technology. The slit restricts the part of the light that reaches the spectrometer and therefore determines together with the magnification of the objective the area of which a spectrum is taken. With a smaller slit width, the spacial resolution is increased, however the intensity of the incoming light is decreased. The standard slit width of this setup is 100 µm.
After passing the slit, the light gets reflected by a spherical mirror onto a diffraction grating with a grating constant of 150 lines/mm. Due to the grating, light of different wavelengths gets reflected in different angles and therefore is spectrally split up/sorted. Such a device which sorts the light spectrally is called a spectrograph, here the 'Shamrock 303i' by Andor Technology.
By rotating the grating, the wavelength of optimal reflection can be chosen. Here a central wavelength of 700 nm is set. The spectrally sorted light gets reflected by a second spherical mirror onto a detector, in this case the charge-coupled device (CCD) camera 'iDus 416' by Andor Technology. The camera chip consists of 256 $\times$ 2000 pixels with a pixel size of 15 $\times$ 15 µm^2 and is cooled down to –39 °C, to reduce dark current in the semiconductor device [129].

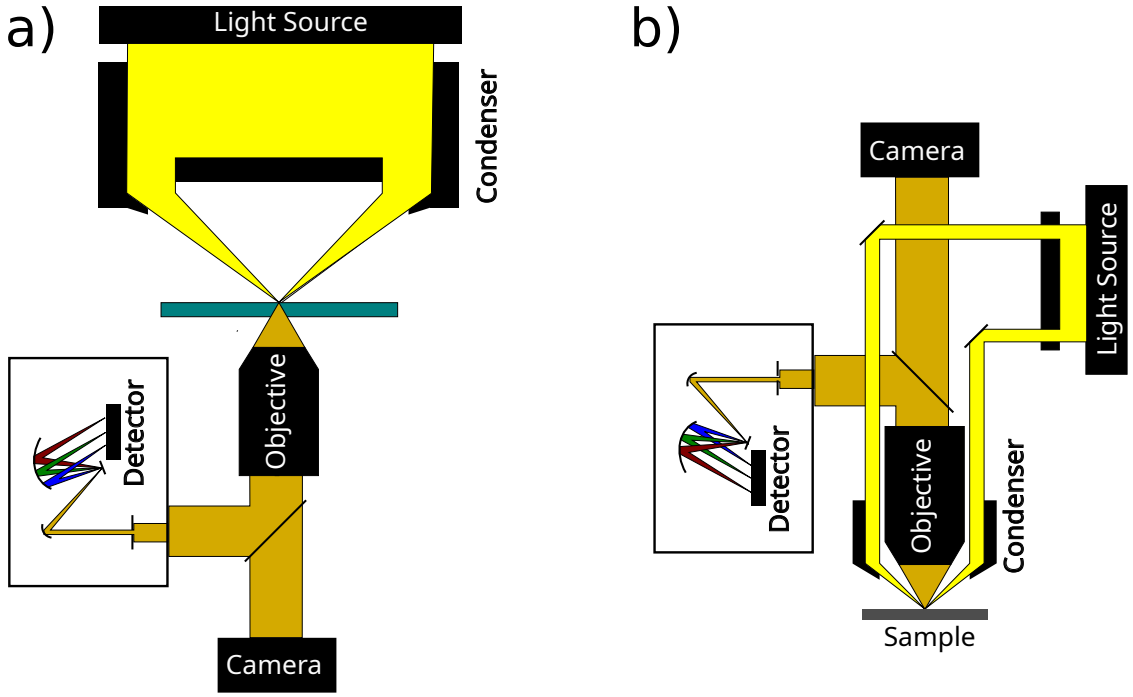

Figure 3.1: a) Scheme of an inverted microscope for transmission measurements with a condenser for dark-field illumination and spectrometer. b) Scheme of a microscope for reflective measurements with a condenser for dark-field illumination and spectrometer.

The second dark-field microscope is the 'Axio Scope A1' by Zeiss, which operates in transmission or reflection mode, but was only used in the reflective configuration. It is used for the probing of samples with a non-transparent substrate, mainly the samples on Si substrate for the SHG measurements.
The beam path can be seen on the right side of figure 3.1 and is generally similar to the one of the inverted microscope, with the difference that the condenser is now integrated into the objective. This way, the sample gets illuminated from the top and collects the reflected signal.
Measurements in the reflective setup were taken with a Zeiss 100× 'Epiplan Apochromat', which has an NA of 0,95 with an integrated condenser NA of 0,97. In the transmission setup, several objectives were used. For the spectra of the core-satellite structures, a 60× objective, the Nikon S Plan Fluor WD 60x/0.70, was used, which uses no immersion medium and therefore does not require cleaning of the sample after every measurement. For back focal plane measurements two different objectives were used: the Nikon Fluor 100x/0.5-1.3 Oil Iris (objective I), which has a variable NA ranging from 0.5 to 1.3, and the Nikon CFI Apochromat TIRF 100x Oil/ 1.49 (objective II) with a fixed NA of 1,49. With an immersion oil (Zeiss Immersol 518 F) of refractive index n=1,518 this translates to opening angles of $\arcsin(0,5/1,518) = 19{,}23°$ for the closed objective aperture up to $\arcsin(1,3/1,518) = 58{,}91°$ for the completely open objective aperture of objective I. Since the condenser has an NA of 0,8 to 0,95 for air (the medium between condenser and sample), which translates to opening angles of the illumination cone of $\arcsin(0,8) = 53{,}13°$ to $\arcsin(0,95) = 71{,}81°$, the first objective can not be

used for dark field microscopy, if the objective aperture is completely open. Since the second objective has an opening angle of $\arcsin(1,49/1,518) = 78{,}98^\circ$, it is not possible to take dark-field images with this objective.

For measurements with immersion liquid, a drop of oil gets placed on top of the inverted objective, followed by the sample on top of the piezo stage. After raising the objective until contact is made through the oil with the sample, the sample can be observed either through the eyepiece or a camera, which is connected via a beam splitter just before the spectrometer.
To obtain the best possible spectra, a software written by Dr. Simon Dickreuter is used. By scanning the sample around the region of interest stepwise in x- and y-direction and integrating the whole spectrum at each step, the spot with the highest signal is found. The same happens in the z-direction, to find the optimal focus spot.
For a corrected spectrum, a lamp, a background and a dark current spectrum have to be obtained. For a lamp spectrum in the transmission setup, simply a spectrum of the light source is taken without a sample, oil or filter in between. In the reflective setup, the light is focused on the surface of a piece of Teflon. The spectrum of the reflected light is then saved as lamp spectrum.
The dark current of the detector is measured by turning off the light source and integrating for the same amount of time as for later measurements. To take a background measurement, first a structure of interest gets focused upon by the procedure described above. After that, the stage gets moved by 10 µm in a direction where nothing else is except clean empty substrate.
Spectra (and background and dark current spectra) are taken after focusing and with typical parameters of 15 s integration time and averaging over 3 measurements. To obtain the corrected spectra from all the ones mentioned above, one has to use the following formula:

$$I_{corr} = \frac{I_{raw} - I_{background}}{I_{lamp} - I_{dark}} \tag{3.1}$$

3.2 BFP Setup

For BFP measurements, the inverted microscope setup described above is extended by Annika Mildner in several ways. A laser beam is coupled into the back of the microscope and can illuminate the structures through the objective from below. Due to that, only reflective measurements of the back-scattered light are possible. However, due to the higher refractive index of the substrate (ITO/glass) compared to air or water, the majority of the power is radiated into the substrate anyway. The continuous wave diode laser has a wavelength of 473 nm, a power of 50 mW and is the model gem473 by Laser Quantum. In the beam path of the laser, before coupling into the microscope is first a shutter, which is coupled to the measurement computer and blanks automatically outside of measurements (but can manually be switched to always blank or always open). The shutter is followed by a laser clean-up notch filter, a set of grey filters with optical densities (OD) ranging from 0 OD (no filter) to 4 OD to tune the intensity, and a polarising beam splitter to ensure a linear polarisation of the laser light parallel to the table surface. Following that, either a $\lambda/4$-plate or a $\lambda/2$-plate can be placed into the beam path. The $\lambda/4$-plate at a 45° setting turns the linearly polarised light into circular polarised light, while a $\lambda/4$-plate at an angle α rotates the polarisation plane by 2α (see chapter 2.2). This way it is possible to illuminate structures along their transversal axis, longitudinal axis, or both at once (with circularly polarised light).
Two mirrors are used and tuned so that the laser is coupled into the microscope objective parallel to the objective axis and in its middle. As a check, the image gets defocused. If the laser spot shifts while defocusing, the laser hits the objective at an angle and must be adjusted accordingly.
To produce the BFP image, an additional lens (the Bertrand lens) is used. This is necessary due to the fact that the BFP of the objective is inside the metal casing of the objective and can therefore not be directionally sampled. The Betrand lens is therefore placed in such a way, that it projects the BFP of the objective onto the CCD camera sensor.
To take a BFP image with objective I, first the aperture in the objective is closed, and the sample can be positioned using the DF image and the camera (the Bertrand lens has to be out of the beam path). Now the halogen lamp is turned off and the objective aperture is completely opened. A bright spot, reflected from the structures, gives a hint if the laser is still in the right position or not. For a higher signal, the grey filter can be changed for a lower OD one or completely removed, however this poses the risk of destroying the sample. The Bertrand lens is swapped into the beam path, to image the BFP. Before the actual measurement, a reference image is taken next to the structure, which is subtracted from the measurement to remove background signal.
For measurements with objective II, only the transmission image of the microscope can be used for positioning of the sample due to the high NA of the objective. A higher number of markers on the sample can help for orientation. Again, the reflection of the laser on the sample can help to find structures. Otherwise, measurements are taken the same way for both objectives.
After the measurement, the objective gets cleaned with lens tissues dipped in petroleum ether. To remove the residual oil from the samples, the samples are

placed in acetone and cleaned in the ultrasonic bath for 5 min, followed by another 5 min in isopropanol and blow-drying with nitrogen.

3.3 Flow cell

Measurements with samples in a flow cell are carried out on the Nikon DF setup as well. The flow cell samples are prepared as described in chapter 4.3 and placed on the piezo stage. Measurements were taken with objective I, but are also possible with objective II, with the same caveats as described above.
Additionally, tubes are inserted in both holes of the flow cell, connecting one side of the channel with a peristaltic pump and the other with an empty bottle, which acts as a waste collector. An image of the setup can be seen in figure 3.2. The pump is the model ISM597D by Ismatec used in combination with Masterflex Ismatec Tygon S3 E-Lab tubes with a 0,19 mm inner diameter. The other end of the tube in the pump is connected to a bottle of either water or water/glycerine mixtures in different ratios. The bottle can be easily changed when stopping the pump, to make measurement series with different liquids in the flow cell. The flow rate is set to 7 ml/min while measuring and to 20 ml/min for cleaning after measurements. The cleaning cycle consists of pumping de-ionised water for 20 min through the whole system, followed by pumping air until the all the water is displaced. This step takes around 5 min, depending on the length of the connection tubing.

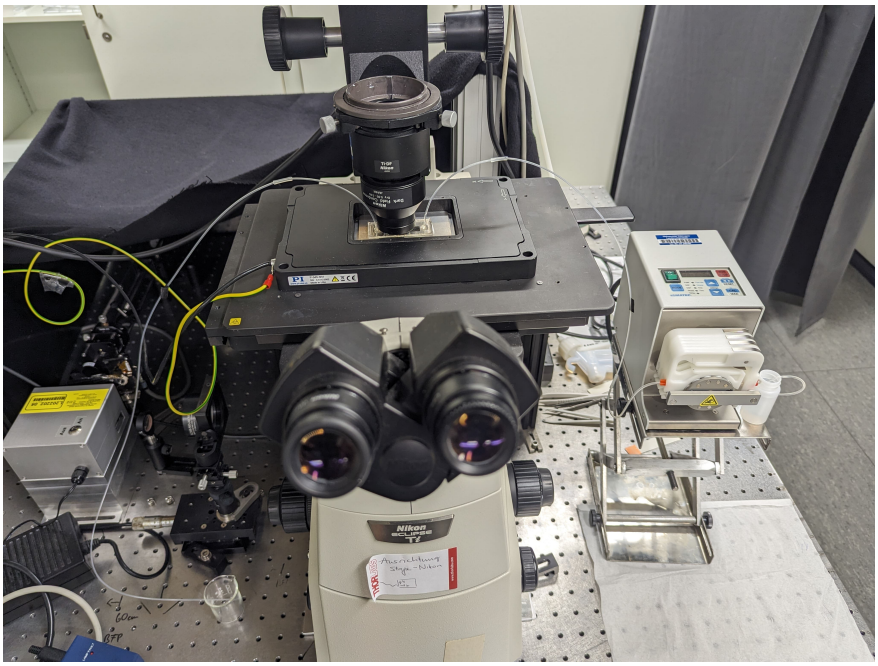

Figure 3.2: Setup for measurements with flow cells. To the right is the peristaltic pump with one end of the tube drawing in water or water/glycerol mixture from a bottle and the other end leading to the flow cell. The flow cell is placed in the inverted microscope on a piezo stage under the dark-field condenser. An additional tube leads from the flow cell to a beaker to collect the liquids.

3.4 BFP parabolic mirror

The setup for measurements of SHG and TPA is a home-built (not by the author of this thesis) parabolic mirror setup in the group of Dr. Dai Zhang / Prof. Alfred J. Meixner at the University of Tübingen. The specialty of such a setup is, that the laser which illuminates the sample is not focused by a lens, but rather by a mirror. A sketch of the setup can be seen in figure 3.3.
The mirror has a hole in the middle, which offers a possibility to see the sample and position it into the focus spot of the laser. Advantages of such a setup are high laser powers without absorption (and possibly destruction) in the lens, as well as a high purely geometric NA. In this setup, a numerical aperture of NA = 0,9986 is achieved with a pulsed laser of wavelength 779 nm at a 40 MHz repetition rate. Due to the pulsed laser, higher peak electric fields can be achieved at lower average laser powers compared to a continuous wave laser. This is useful to generate a high SHG signal without destroying the sample. Laser powers of 32 mW are possible and useful for SHG measurements, but even the pulsed laser potentially can melt gold samples at that power level. The power is tuned down for that reason to 10 mW.
Furthermore, the setup has a Glen-Taylor prism to produce linearly polarised light and a half-wave plate to manipulate the polarisation plane. It should be noted, that the beam splitter in front of the mirror reflects laser light of wavelength 779 nm but blocks this wavelength in transmission towards the detectors. Measurements on this setup were performed by Felix Schneider.

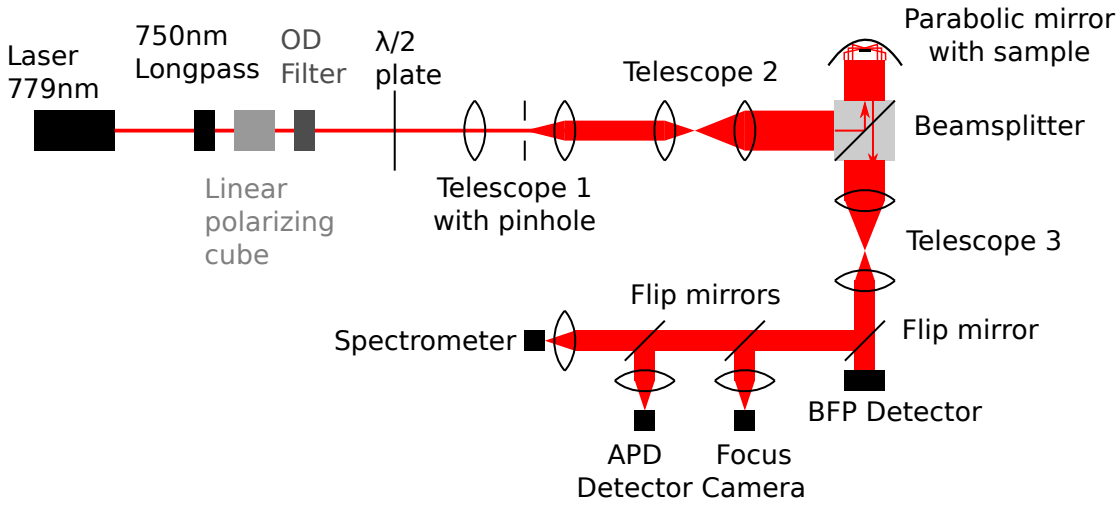

Figure 3.3: Scheme of the parabolic mirror setup. The laser is focused on the sample via a mirror instead of conventional lenses, which makes the setup suitable for high NA and high intensity measurements.

3.5 Raman spectroscopy

The Raman spectroscopy measurements were carried out on a setup of the group of Prof. Dr. Frank Schreiber at the University of Tübingen. The setup is a commercially available one: the LabRAM HR by Horiba Jobin Yvon. It is fitted with a 632 nm laser, whose intensity can be reduced by a set of optical filters. The laser powers typically used were 1,3 mW and 2,5 mW and are specified for the given measurements. The setup has a grating of 1500 lines/mm and the sensor is cooled down to –120 °C with liquid nitrogen to decrease noise.
The objective used to focus the laser and collect the signal is an Olympus LMPlanFL N with a magnification of 50 and a numerical aperture of 0,50. Measurements were performed by the author of the thesis after an introduction to the instrument by Frederik Unger.

4 Fabrication

This chapter provides an overview of all the fundamental methods used over the course of the thesis. Firstly, the broadly used electron beam lithography technique is introduced and explained how it is applied to produce Yagi-Uda-antennas. Secondly, optical lithography, which is used to produce flow cell positives and marker structures, gets explained. Thirdly, the Helium-Ion-Microscope (HIM) is introduced and how it is used to either produce or further manipulate existing Yagi-Uda-antennas. Following that, the fabrication steps for the flow cells, which are used for refractive index measurements, are explained. Lastly, the instructions on how to produce planet satellite structures, which were provided by Dr. Yingying Cai of the group of Prof. Philipp Vana from the University of Göttingen are shown.

4.1 Lithography

Lithography processes are mostly used to create a pattern of variable size and form on a substrate. To do so, a substrate is coated with a resist, which is then exposed (either by (UV)-light or electron beam) in the desired pattern. In case of a positive resist (as shown in Figure 4.1) the exposed resist gets dissolved in the developer and leaves the patterned resist on top of the substrate. The mask can now be used for further production steps such as evaporation and lift off or as an etching mask.

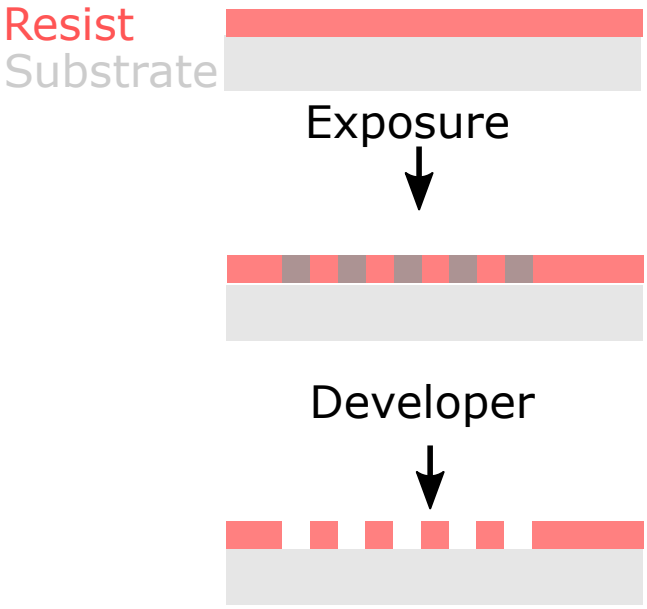

Figure 4.1: Basic scheme of a lithography process with a positive resist.

4.1.1 Electron Beam Lithography

Electron Beam Lithography (EBL) was used as the main technique to fabricate Yagi-Uda-antennas of variable sizes and arrangements. For start, a microscope cover slip ($18 \times 18\ mm^2$) is cleaned for 5 min in a 10% KOH solution, followed by another 5 min in the same KOH solution with additional H_2O_2 (ratio 2:1). A thin layer (50 nm) of indium tin oxide (ITO) is then deposited on one side (now the top side) of the glass. This is done as a sputtering process.
The layer is nearly completely transparent and conductive (enough) due to the semiconducting properties of ITO. This helps to prevent charging effects on the sample during the EBL process as well as during the inspection of the samples in the Scanning Electron Microscope (SEM), while still allowing measurements in the optical setup.
To prepare the sample for EBL, a 120 nm thin layer of Poly(methyl methacrylate) (PMMA) is spin coated on top of the ITO layer in two steps: first at 2600 rpm for 6 sec to spread the resist, followed by a step at 5000 rpm for 60 sec to reach the final thickness of 120 nm. The resist is pre-baked at 150 °C for 5 min to evaporate some of the solvent.
After the patterning in the SEM with the desired structures, the sample is developed in a mixture of methyl isobutyl ketone (MIBK) and isopropanol (ratio of 1:3) for 65 sec. The result, in the case of a positive resist like PMMA, is that the exposed structures get dissolved and are now left as holes in the mask. To finish off the fabrication of simple antenna structures, a layer of gold (40 nm) is thermally evaporated on top. In a lift-off process, the remaining layer of PMMA is dissolved in acetone, which also results in a removal of the gold layer on top of it. The only remaining gold on the sample is the one directly on the ITO in the shape of the pattern, which was written into the resist during the EBL process. In figure 4.2 one can see an array of antennas fabricated in the way described above.
If, for some reason, the ITO layer should be omitted, the sample has to be made conductive in another way. Here it was done with a conductive resist: the Protective Coating AR-PC 5090.02 (Electra 92) by Alresist. Again, first, a PMMA layer is applied as described above on a clean glass substrate. Due to the smoother surface of glass, layers of PMMA resist tend to be thinner on glass substrates, hence the spin parameters were decreased to 3000 rpm for 60 sec to still obtain a 120 nm thick resist layer.

Before applying the Electra 92 on top of that layer, it gets filtered with a 0,2 µm pore sized filter, which helps to achieve an even distribution of the conductive film without any holes. The Electra 92 resist is spin coated on top of the PMMA layer at 4000 rpm for 60 sec, which results in a layer thickness of 40 nm [130].
The resist gets tempered at 90 °C for 2 min, before it is ready to use for EBL. After the exposure, Electra 92 can be removed in a water bath and the rest of the process can proceed as described above.
Due to the lower conductivity of Electra 92, structure sizes are limited to around 20 nm, however this is small enough for all structures that were fabricated in this work [130].

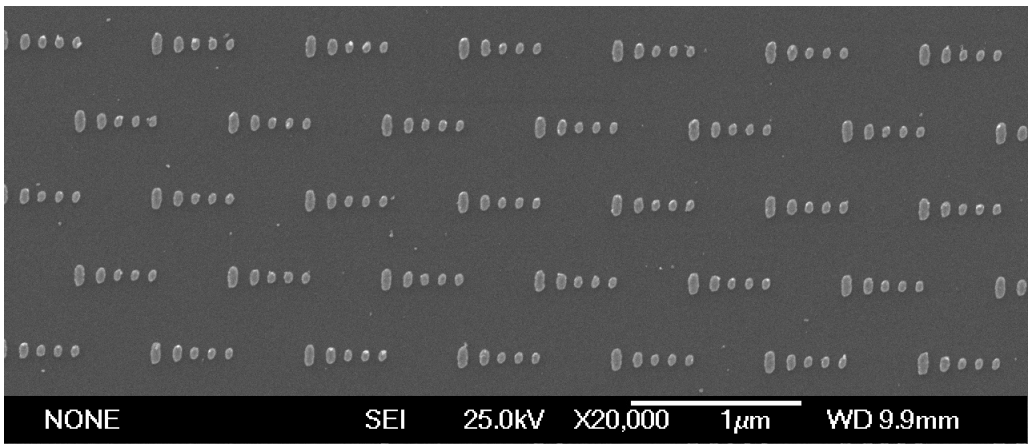

Figure 4.2: SEM image of Yagi-Uda-antennas fabricated with an EBL process.

4.1.2 Optical Lithography

Optical lithography was used in two different ways in the course of this work. One way was the production of a grid structure on glass/ITO substrates, which were then used to assemble planet-satellite structures on top of it (see chapter 4.4). This way, it is possible to take optical and SEM measurements at the exact same particle. The fabrication of the grids is similar to EBL. On top of the glass/ITO substrate, a layer of resist (ma-P1215) is spin coated (at 300 rpm for 30 sec) and pre-baked at 90 °C for 12 min. The pattern is written into the photosensitive resist with a focused LED light source, which is rastered over the sample, exposing the resist to UV-light in a controlled manner. This way of patterning is called maskless alignment (since no photomask is used) and was done in a μMLA by Heidelberg Instruments
After the development of the positive resist in ma-D 331 for 40 sec, a layer of gold is thermally evaporated on top. Analogous to the EBL process, the resist gets removed in acetone, leaving only the desired grid structure on the sample.
Furthermore, the maskless aligner was used to fabricate a mask to use in a classical mask aligner (which will be explained further down). This time, the glass substrate is already covered with a chrome layer on one side (low reflective chrome on soda lime by g-materials). On top of that, again the same photoresist (ma-P1215) is applied in the aforementioned manner. After the patterning in the maskless aligner and the same developer process, the whole mask is submerged in chrome etch (TechniEtch Cr01 by MicroChemicals) for 30 sec. Now, only the part where the resist was dissolved in the developer process is exposed to the etchant, which results in the desired pattern being etched into the chrome layer.

The photomask can now be used in a classical mask aligner for photo lithography. In the case of this work, it was used to produce a positive mould, which can then be used to produce flow cells (see chapter 4.3). The process described in the following section is derived from the manufacturing sheet [131]. To start off, a 4 inch wafer is cleaned in an acetone ultrasonic bath, followed by one in isopropanol. After that, the wafer is dried completely on a hotplate at 100 °C for 5 min. Around 2 g of SU-8 resist are spin coated on top of the wafer. A low spinning speed of 500 rpm is used to spread the resist on the wafer, followed by a higher spin rate of 4000 rpm, to

reach the final thickness.
The resist is soft baked to evaporate the solvent and densify the film. This is done in two steps: one at 75 °C for 10 min, immediately followed by a second one at 95 °C for 15 min. The temperature control ensures reduced stress formation in the resist and therefore cracking, as well as better resist-to-substrate adhesion [131].
The resist is exposed in a classical mask aligner with the help of the aforementioned mask. The mask gets pressed onto the resist, with the metal side facing towards the resist. This ensures, that no gap is between the mask and the resist, which suppresses diffraction of the light and ensures sharp structures. The resist is exposed (through the holes of the mask) for 10 min to the light of a mercury vapour lamp. Before the resist is developed, it has to be post-exposure baked at 75 °C for 2 min, followed by 5 min at 95 °C. This ensures a selective crosslinking of the exposed parts of the film.
To develop the resist, it gets submerged for 5 min in propylene glycol methyl ether acetate (PGMEA). Since SU-8 is a negative resist, the pattern of the photo mask remains on top of the wafer and can be used to produce flow cells.

4.2 Helium Ion Microscope

Most of the nanostructures of this work were produced with the help of EBL, as described above. However, even this advanced technology has its limitations [132]. A new microscope, similar to the SEM, has been developed: the Helium Ion Microscope (HIM). Instead of rastering an electron beam over the sample surface, the same is done with helium ions. The ions are produced via the field effect. At the tip of a wolfram needle, which typically consists of three atoms (called the trimer) a positive voltage is applied. Due to the field gradient, helium atoms are drawn towards the needle, where the field strength exceeds a few V/Å. Approaching the apex and therefore maximum field strength, the outermost electrons can tunnel into the tip, leaving positive helium ions, which are accelerated away from the tip [133]. The ion beam then gets focused and manipulated with electro- and magnetostatic optics to form a focused beam.
The advantages are smaller probe sizes (due to lower energy spread between the individual ions) and a narrow sample interaction volume near the surface [133].
Another difference between SEM and HIM however is not only the potential higher resolution and sensitivity, but also the interaction of the relatively heavy (compared to electrons) helium ions with the material the HIM scans over. The ions have such a high momentum, that they can eject material out of the surface they are hitting. This effect is called sputtering [134]. This effect is similar to that of Gallium Focused Ion Beams (FIB), where the beam consists of gallium ions. However, due to the lower mass and higher velocity of the helium ions, the interaction volume is small on the surface, which leads to very high precision manipulation of the surface with feature sizes down to the regime of only several nanometres.

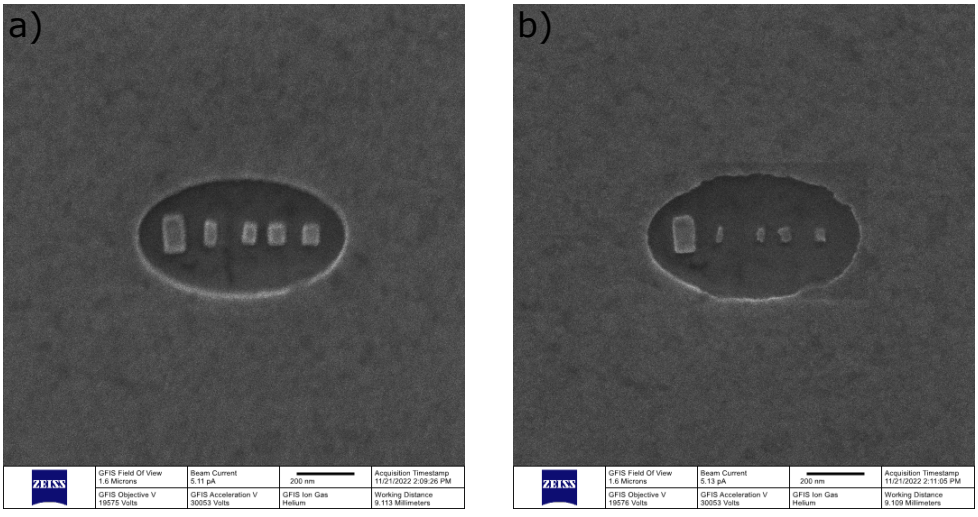

Figure 4.3: Damaging of structures in the HIM by scanning over and focusing on them. a) Image was taken immediately after milling in the HIM. b) Image was taken after refocussing on the newly produced structures. The highly focused helium ion beam scanning over a small area clearly has a high enough etching rate to destroy delicate structures.

One downside is, that due to the light mass of the helium ions the sputtering rate is low, since only around every 14th helium ion is sputtering a gold atom [135]. Furthermore, the sample gets damaged already by just imaging it, and micro-cavities of accumulated helium atoms build up in the sample [136]. Additionally, one could see second hand sputtering which widened gap sizes, potential redeposition of the sputtered gold [137], and reproducibility issues (see figure 4.3 and figure 4.4).
The HIM used was a Zeiss Orion NanoFab and was used in two different ways: the fabrication of antennas and the manipulation of antennas. The fabrication of antennas in the HIM started off with a classical electron beam lithography step, however, two different approaches were taken.

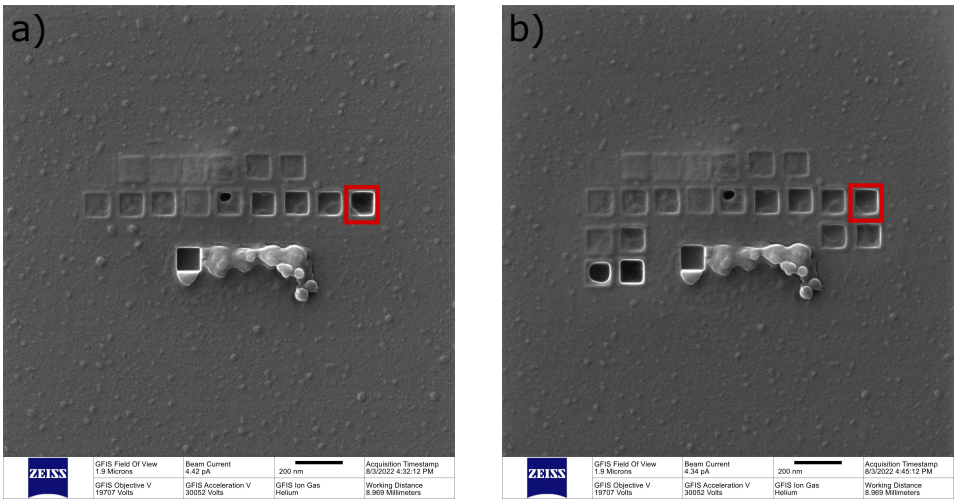

Figure 4.4: Series of dose tests, to determine what dose is needed to etch through a 50 nm layer of ITO. It can be seen, that the test field in the red square of picture a) appears to be etched through at first. However, after several further attempts in the same area, the test hole appears to be filling back up due to sputtered ITO and carbon residue in the chamber.

For the first attempt, the EBL is performed on a glass substrate with an ITO layer on top and follows the steps of EBL on a conducting substrate. The EBL process and subsequent evaporation of 40 nm gold produced rectangles with dimensions of 225 nm $\times$ 560 nm and lattice constants of 4 µm in x- and y-direction (see figure 4.5). These patches are used in the HIM to etch out the antennas with high precision. Different approaches were taken on how to achieve the sharpest antenna structures with the closest dimensions to the ones established in simulations.
On the one hand, it was tried to use low currents of around 3 pA produced by a small aperture of 10 µm, low helium pressure of 1×10^{-6} Torr and a crossover point of the beam of "5". The advantage of this configuration is a highly focused beam with low opening angle. This way, the narrowest line cuts with line widths of 6 nm and highest precision are possible. The drawback however is a low etching rate. To etch an antenna out of the aforementioned patches, high doses of over 15 nC/µm^2 and durations of over 10 min are required for a single antenna. This makes it not only a very uneconomical way to produce antennas, but also a suboptimal one, since

the stage of the HIM is slowly drifting, which can amass over the course of 10 min to several nm, which negates the advantage of the high precision etching (see left side of figure 4.6).

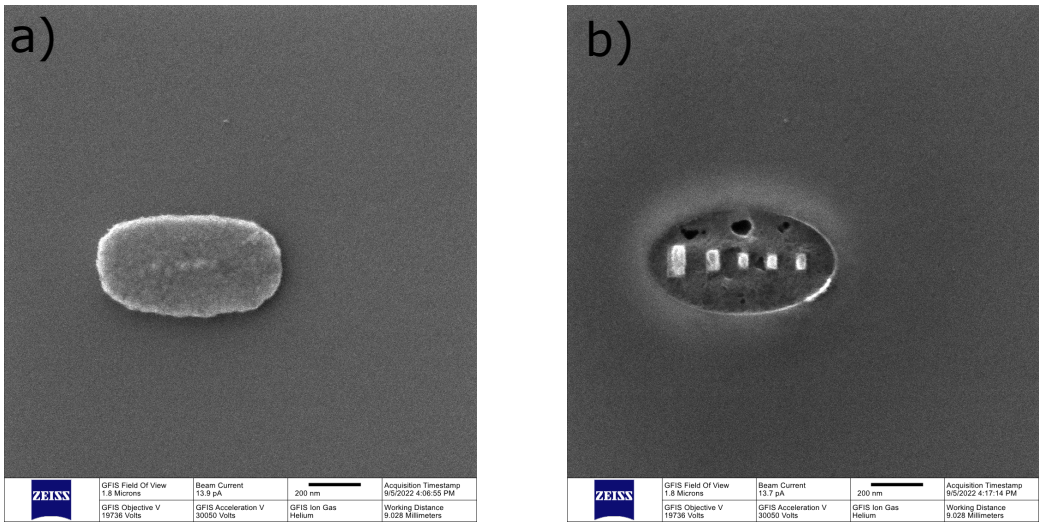

Figure 4.5: a) Patches of gold on ITO for the fabrication of Yagi-Uda-antennas in the HIM. b) Yagi-Uda-antenna etched out of a gold patch on ITO. Over the antenna, holes can be seen, where the ITO layer is also etched through.

To counter the two major downsides of the high precision, but low effective beam configuration, a higher current configuration with a current of around 13 pA is chosen. The 20 µm diameter aperture is chosen, as well as a higher helium pressure of 2×10^{-6} Torr and a lower crossover point of "4" to achieve a compromise between high current and high precision. Especially, the higher helium pressure is an easy way to increase the current without increasing the spot size of the focus. Due to the higher pressure in the gas field ion source (GFIS), more atoms come into close vicinity of the trimer, where they get ionised and can contribute to the ion beam current without influencing the quality of the beam [138]. However, this can only go up so far, as a higher increase of pressure also increases the probability of destruction of the trimer configuration at the tungsten tip.
A larger diameter aperture, however, allows for ions with higher deviation of the optimal and intended beam path to reach the sample, therefore increasing the focus spot size. The same applies for a lower cross-over point of the beam in the HIM column closer to the aperture, therefore these two parameters have to be adjusted carefully.
For the design of the etching patterns, the NanoPatterning and Visualization Engine (NPVE) software was used, which was distributed together with the HIM. As a base pattern, an oval shape was used, which fits the shape of the gold patches. Into that shape the Yagi-Uda-antenna design was laid out with rectangles and the shapes combined with a NAND operator in such a way, that everything in the oval gets etched away except the rectangles of the Yagi-Uda-antennas.

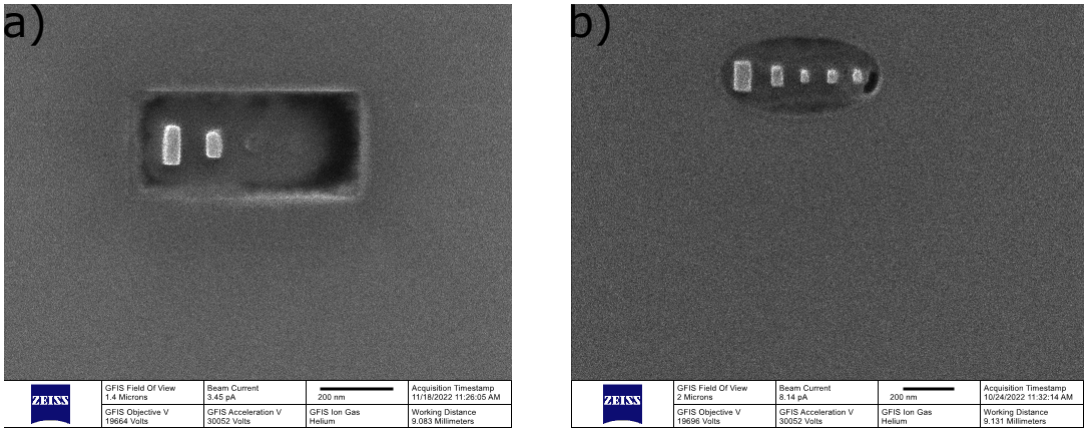

Figure 4.6: Yagi-Uda-antennas etched from gold patches; a) low-current configuration, b) high-current configuration.

As can be seen in figure 4.6, the configuration with high currents yields better results than the one with lower current. This is due to the drastically lower etching times of only 1-2 min compared to the over 10 min for the low-current configuration, which heavily counters the misplacement of the structures due to stage drift. Additionally, the required dose decreases to $7\,\mathrm{nC}/\mu\mathrm{m}^2$, since the etching rate apparently also increases with higher current configuration.

Since the ITO layer appears to be relatively soft material for HIM etching with also a relatively high secondary sputter rate of the ejected ITO atoms/molecules, it was tried to generate a configuration with gold directly on top of the glass substrate. For this second configuration, EBL was performed as described in chapter 4.1.1 in the configuration of non-conductive substrates with an Elecatra 92 layer on top of the PMMA resist. As an adhesive layer between the glass and the gold, a thin layer of 3 nm of chromium was evaporated on the glass before the gold was evaporated on top.
To make the sample conductive, a 10 nm thick layer of ITO was sputtered on top of it. Again, the same etching pattern with the high-current configuration is applied to the gold patches to fabricate Yagi-Uda-antennas.
Additionally, the etching pattern was modified in a way that now half of the antenna gets exposed to a low etching dose such that the ITO layer gets removed on one half of the antenna.
A similar way to use the HIM to manipulate antennas was with an SiO_2 coating. To do so, Yagi-Uda-antennas were fabricated in a standard EBL process on a glass/ITO substrate, but now with an additional 10 nm layer of SiO_2 on top of the gold antennas before the lift-off. In the HIM, it was now tried to remove the SiO_2 layer on the upper half of each antenna element, so that the antenna is again half covered in SiO_2 (see figure 4.7). This was done in an attempt to manipulate the emission direction of the antennas (see chapter 5.6).

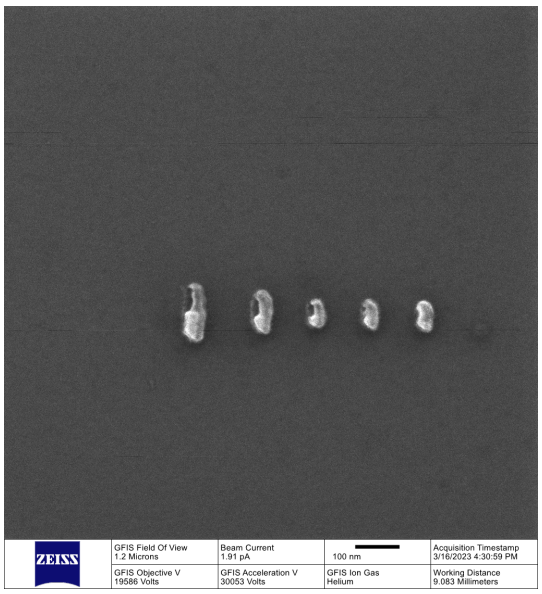

Figure 4.7: Manipulation of the antenna. Antennas were first fabricated in an EBL process with a layer of SiO_2 on top of the gold antenna elements. With the help of the HIM on one half (in this case towards the top of the image) the SiO_2 layer was etched away, exposing the gold elements beneath.

4.3 Flow cell

For the manipulation of the directivity and for the use of the antennas as refractive index sensors, the antennas were incorporated into microfluidic flow cells. The flow cells consist of two main parts, a large glass substrate (dimensions: $2 \times 6\,cm^2$) at the bottom, on which the Yagi-Uda-antennas are fabricated with either EBL or HIM assisted techniques, and a counterpart on top made out of polydimethylsiloxane (PDMS).
To produce the channel top made from PDMS, the flow cell positive out of SU-8 on a Si substrate is used (see chapter 4.1.2). However, before it is used it gets treated with a layer of tridecafluoro-1,1,2,2-tetrahydrooctyl-1-trichlorosilane (F_{13}TCS). This process is done in a glove box due to the very dangerous nature of the chemical [139]. First, the wafer gets heated to 150 °C for 30 min in a Petri dish to get rid of remaining water on the wafer surface. A drop of F_{13}TCS gets cast in the Petri dish close to the wafer and is then enclosed by a second Petri dish. Following that, the sample remains another 30 min on the hotplate, which completes the Chemical Vapour Deposition (CVD) process, and all open hydroxyl groups of the wafer could bond with an F_{13}TCS molecule. After cooling down, the wafer gets submerged once in a water bath to ensure that all remaining free F_{13}TCS molecules react with water, therefore rendering them harmless.
With this step an easy removal of the PDMS from the rectangular mould and the channel positive made from SU-8 is ensured (see figure 4.8). Due to the protective layer, adhesion between SU-8 and wafer becomes greater than between SU-8 and PDMS, which reduces the possibility of accidentally removing the channel positive from the wafer and therefore increases its reusability.

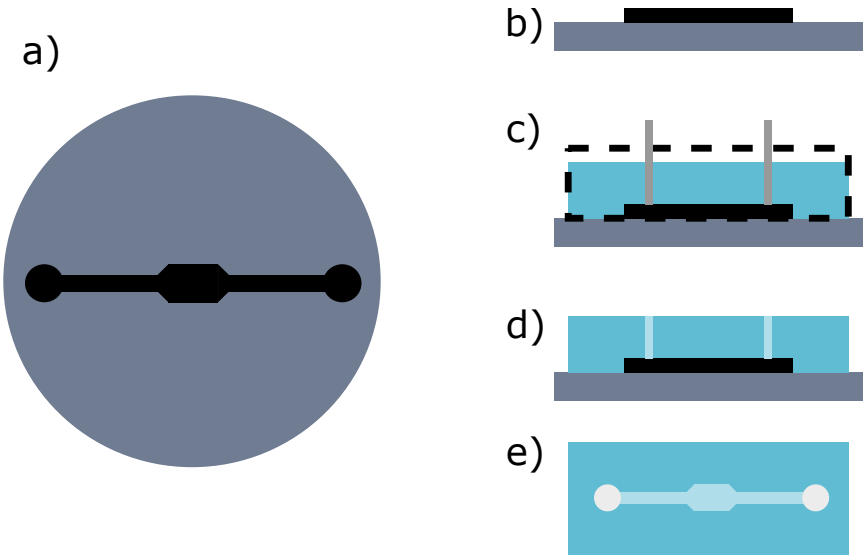

Figure 4.8: a) Scheme of the channel positive made from SU-8 on silicon wafer. b) Prepared wafer with channel positive on top. c) The mould gets placed on top and centred. Small needles get placed on the circular ends of the channel positive to provide a feed for tubing. The PDMS/curing agent mixture gets poured into the mould. d) After curing the PDMS on the hotplate, the mould and needles are removed. e) PDMS piece with holes for tubing and a flow channel imprint. The channel is completed by pressing a glass with antennas against it.

The PDMS ('Sylgard 184' by Sigma Aldrich) for the channel top gets prepared by mixing 2 g of PDMS with 0,2 g temperature sensitive curing agent (or generally in a ratio of 10:1). To ensure thorough mixing, the PDMS is stirred for 5 min and then stored for at least one hour in the fridge. Since the curing process is temperature sensitive, only very little reaction happens in the fridge, and it can be stored there for over 24 h before final usage.
The waiting step in the fridge is essential so that air bubbles, which build up during the mixing process, can diffuse out of the PDMS before it gets finally cured. While settling in the fridge, the mould for the PDMS gets set up. It is made up of the coated wafer with the channel positive on top of a (at first cold) hot plate, a hollow aluminium block with inner dimensions of $2 \times 6\,\mathrm{cm}^2$, an acrylic plate on top of the aluminium block with slits to pour PDMS through, pinholes for needles of the same diameter as the tubes of the peristaltic pump, and lastly the needles themselves, which go through the pinholes and sit on the ends of the flow channel positive (see figure 4.8).
Only a small amount of PDMS is poured into the mould carefully, in fact so little, that the relatively high viscosity liquid needs up to 10 min to fully settle and cover the whole area defined by the aluminium block. This is necessary, because otherwise the flow cell would be too thick to fit between the dark field condenser and objective (see chapter 3.3) and has the additional advantage that air bubbles, which occurred during pouring, can diffuse out of the PDMS.
After settling, the hotplate gets turned on to 150 °C, so that the PDMS can be cured for 12 min. As a result, the PDMS has an elastic, rubber-like texture and can be care-

fully peeled out of the aluminium block and from the surface of the wafer. The PDMS strip now has the flow channel negative on the bottom side and two holes at the ends reaching through the strip to the top-side.
For the final assembly, the PDMS strip gets placed bottom-side up in the Reactive Ion Etching (RIE) machine, to activate the surface in an oxygen plasma (20 W, 100 mTorr, 30 s). During this step, polar hydroxyl groups (-OH) are formed in the PDMS surface that can now form covalent bonds with silica-based materials such as glass or any material that has the same hydroxyl groups [140, 141]. Afterwards, the PDMS strip gets placed very carefully bottom-side down on top of the glass substrate with the antenna structures. It is most important that the (small) flow channel and the area with antennas overlap, so that the antennas are placed inside the channel. If the alignment is correct, the PDMS strip gets carefully pressed onto the glass by applying pressure with the hands from the inside (area with channel and antennas) to the outside. The activated PDMS sticks to the glass strongly enough for it to seal the channel and is leakproof for the typically very low applied pressures by the pump.

4.4 Core-Satellite Structures

The core-satellite structures, which were examined in this work, were fabricated by Yingying Cai in the group of Philipp Vana at the University of Göttingen. The following section is based on the paper [72] by Cai et al. and its supplementary information.
The structures consist of gold nanoparticles, which are capped with polyethylene glycol (PEG) as satellites around a single core of a pristine silica particle. The production (see figure 4.9) consists of two main steps, which both take advantage of the properties of the PEG shell. Firstly, the PEG works as multidentate linker between the gold nanoparticles and the silica core, which leads to an adsorption of the gold nanoparticles on the surface of the silica core. This happens due to hydrogen bond interactions of the PEG with the silica surface. The PEG wraps around the core, which gives a high contact area with a high amount of bonds and therefore stable bonding.
Secondly, when casting the solution onto a flat surface, the PEG chains offer sufficient mobility so that the gold nanoparticles can rearrange themselves around the silica core and can produce two-dimensional ring structures between the silica core and the surface.

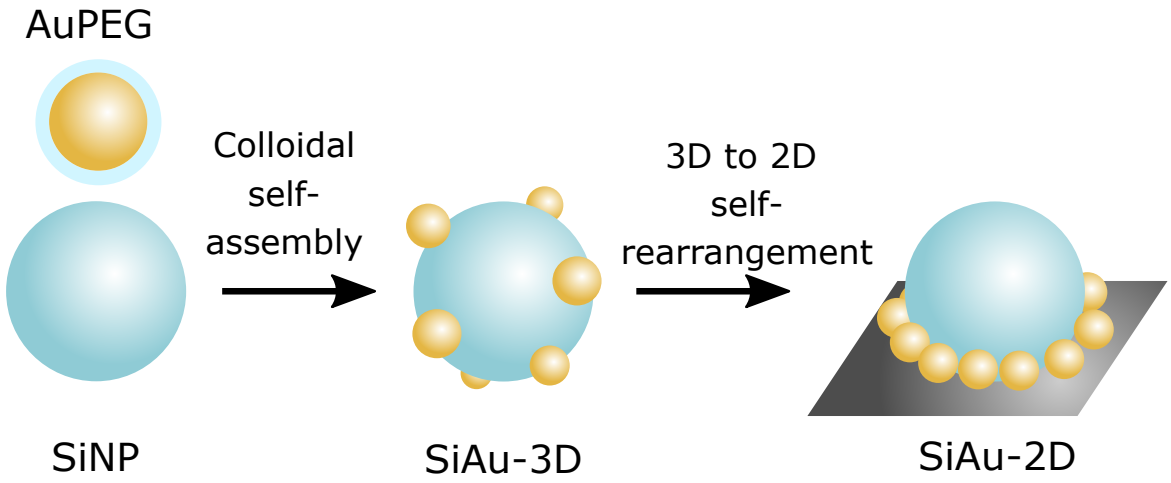

Figure 4.9: Fabrication scheme of the core-satellite structures. First, gold nanospheres are coated with a PEG layer. The nanospheres and the silica cores form clusters mediated by the hydrogen bonds of the PEG on the silica surface. After drop casting, the gold spheres have sufficient mobility to arrange in a 2D structure, surrounding the silica core in a ring.

The typical production steps for 13 nm diameter gold nanoparticles are the following [142]: To a boiling solution of $HAuCl_4$ (500 mL, 0,5 mM) a hot solution of sodium citrate (25 mL, 39 mM) is added. After refluxing for 15 min, the solution gets cooled to room temperature. This results in 13 nm diameter gold nanoparticles, which can be used as seeds for larger diameters and can be modified according to [143] by adding additional sodium citrate solution and $HAuCl_4$ solution while stirring at

90 °C [72].

For adding the PEG layer, 120 mL of the citrate-capped gold nanoparticle solution is mixed with an aqueous solution of poly(ethylenglycol)methyletherthiol (500 mL, 2 mg/mL) in an ultrasonic bath. For changing the solvent from water to tetrahydrofuran (THF), the solution is centrifuged (12 000 rpm, 90 min) four times with redispersion in between the cycles.

The synthesis of the silica cores is based on the technique shown in [144]. The following recipe is for silica beads of 39 nm diameter, but the diameter can be adjusted with the dosing of the tetraethyl orthosilicat (TEOS). IGEPAL® CO-520 (31,3 g) by Sigma-Aldrich and cyclohexane (250 mL) are mixed while stirring for 10 min. Following that, ammonia (32%, 2,3 mL) is carefully added dropwise, and stirring proceeds for another 30 min before adding the TEOS (1,72 mL). The reaction then proceeds for another 22 hours under stirring at room temperature, before it gets quenched by adding ethanol (50 mL) to the mixture. Purification of the mixture is done by three centrifugation cycles (5000 rpm, 30 min) in ethanol, before dispersing in THF for storing.

The self-assembly into 3D colloidal nanostructures happens by mixing the aforementioned silica and gold nanoparticle solutions. A typical amount would be 27 µL of gold nanoparticle solution (which contains around 3 mgAu/mL in THF) into 120 µL silica solution (0,1 mg/mL) under bath sonication. Another 30 min of ultrasonic bath is followed by stirring on an orbital shaker (150 rpm) overnight. This ensures a good mixing and saturation of gold nanoparticles on the silica surface.

To purify the colloidal solution from excess gold nanoparticles, glass beads with a diameter of 0,5 mm are added. On the surface of the glass beads, excess gold nanoparticles can accumulate the same way they did on the silica cores with typically 12 mg of glass beads removing 1 µg of 13 nm sized gold nanoparticles. Clean-ups happen in two steps, where half of the beads is added to the unpurified solution and topped off with THF until all beads are submerged. After each addition, the sample is mixed on an orbital shaker (175 rpm, 20 min). The purified colloidal solution is retrieved by a micropipette. Transmission electron microscopy (TEM) images of the solution can clarify, whether additional cleaning steps are necessary.

To form the 2D core-satellite structures, the colloid solution is simply drop cast on the desired substrate surface, here glass/ITO substrates with gold grids (see chapter 4.1.2). The solvent simply evaporates under ambient conditions, and samples are ready for characterisations with DF microscopy or SEM imaging.

Since some of the samples were contaminated with a considerable amount of residue after drop casting, some of those samples were cleaned up with an oxygen plasma in a reactive ion etching (RIE) process. The cleaning was done in a Plasmalab 80 by Oxford Instruments (20 W, 100 mTorr, 10 °C, 3 min). Since the sample

was much cleaner after the plasma etching, it is assumed that most of the residue was excess PEG. Noticeably, in the SEM one can see the difference between samples which were plasma cleaned and those that were not, by a missing 'halo' around the structures. It is assumed to be the PEG, which functioned as a mediator in the chemical synthesis (see chapter 6).

5 Yagi-Uda-antennas

Yagi-Uda-antennas have been a proven antenna concept in the radio frequency regime for decades since their invention [1]. Due to their simplicity in design, a translation of the concept into the optical regime was sought after. To find the optimal design for this work, numerical simulations have been first carried out in the programme Lumerical by ANSYS. After establishing multiple designs, the fabrication had to be tweaked to fabricate antennas of the same dimensions. After improving measurement regimes over time, directed emission could be seen from a single illuminated antenna structure. From there on, additional features were added to the antennas themselves or they were incorporated in flow cells.

5.1 Simulations

Simulations were carried out to find the highest intensity of the field in forward direction, which was emitted into the substrate. It was first decided to optimise the antennas for a wavelength of 650 nm, because that was the wavelength of the cadmium selenide/zinc sulphide quantum dots (by PlasmaChem GmbH), which were later tried to couple to the antennas to drive them.
The simulation setup consisted of a glass substrate with known refractive indices [145] and a 50 nm thick ITO layer with a fixed refractive index of 1,9. Although the refractive index of ITO is wavelength dependent, it is also preparation dependent. Since there is no data available for sputtered ITO layers with the exact parameters as stated in the fabrication section, the refractive index of ITO had to be estimated. The estimation is based on former published data [146] and yielded good alignment between simulation and experiment.
Two 2D discrete Fourier transformation (DFT) monitors were placed 0,15 µm above and below the surface of the ITO layer in the x,y-centre of the simulation. Both monitors have dimensions of 2,95 µm $\times$ 2,95 µm. The monitors register the electrical field at the surface and can also perform a transformation into the far field. The transformation is done by a projection of the far field onto a hemisphere surface 1 m away from the monitor.
A point source is located on the x-axis 0,035 µm away from the coordinate origin and 0,025 µm above the surface. The polarisation of the point source is parallel to the y-axis, has a wavelength range of 600 nm-900 nm and a pulse length of 3,98 fs.
To find the optimal geometry, first a gold feed is placed into the origin with a height of 0,05 µm. A parameter sweep is performed, to find the length that has the best resonance at 650 nm. Following that, the reflector element is introduced, and several sweeps determine the optimal length and distance to the feed to suppress backwards reflection. After that, three directors are placed and again their size and distance is swept to find the best forward directivity. However, always the same size and distance is chosen in the sweeps for all directors. The final dimensions chosen as the target for fabrication can be seen in figure 5.1.

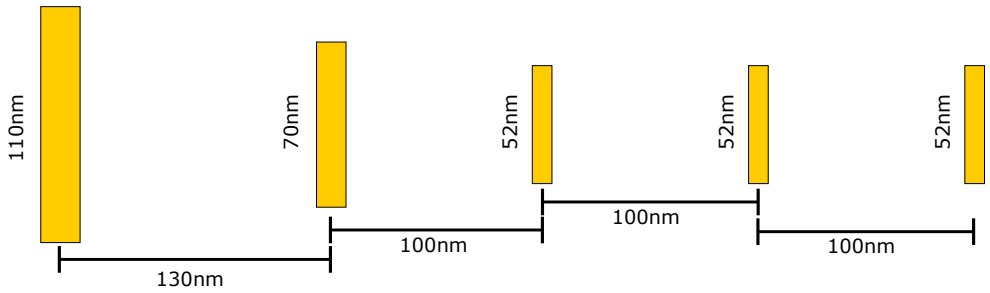

Figure 5.1: Sketch of the final Yagi-Uda-antenna dimensions.

The far-field projection of this configuration can be seen in figure 5.2. The far-field emission of this antenna into the glass/ITO substrate shows a directivity of $D_{max} = 2{,}76$ into the direction of the directors. The calculation was done by comparing the maximum emission (the forward direction) to the average emission. The front-to-back ratio (f/b ratio) is calculated by dividing the maximum emission by the emission of the angle rotated by 180° to that (the direction of the reflector). The f/b ratio is 3,43 for the simulation.

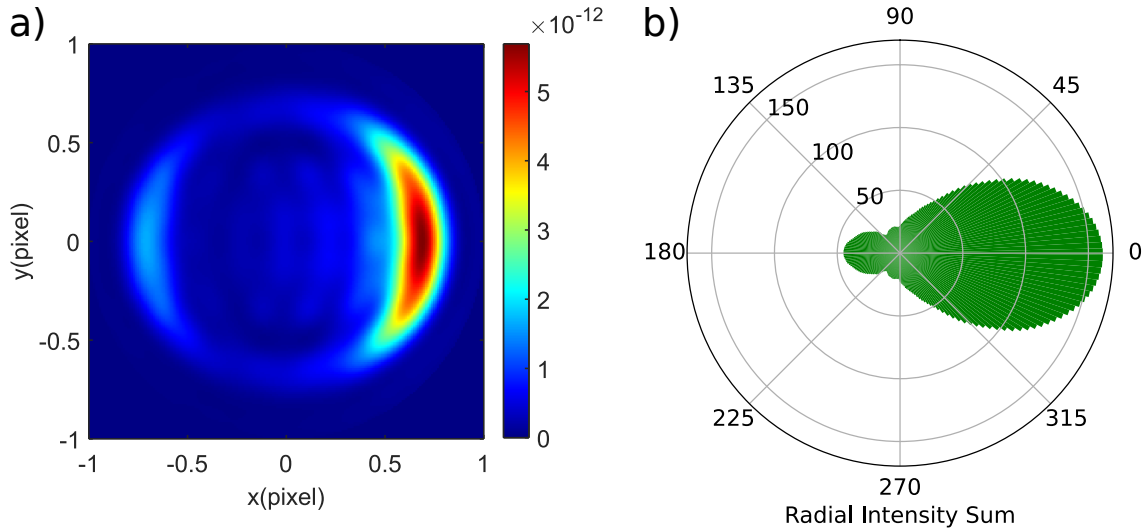

Figure 5.2: a) Far-field projection of the near field simulated with the configuration mentioned above and antenna structure from figure 5.1. b) Radial intensity distribution of the simulated antenna emission.

5.2 Spectra

Over the course of this work over 200 sample substrates were fabricated, each consisting of typically 4 antenna fields with around 400 antennas in each field. Of these samples around a quarter were prepared in the final standard dimensions and geometries. Simple spectra of Yagi-Uda-antennas are taken in the DF setup with the help of illumination via the blue laser. Since the spectra of the antennas were not the main focus of this work, only around 40 antennas have been analysed spectrally. Since the fabrication process proved to be reliable, different antennas and their spectra did not differ too much. The mean laser-driven spectrum of 23 standard Yagi-Uda-antennas with standard deviation intervals can be seen in figure 5.3.
Both laser filters (see chapter 3.2) are placed in the beam path to suppress the laser signal as much as possible. The suppressed part of the spectrum due to the notch filters is visible in the spectrum between 467 nm and 482 nm. A broad peak can be seen at 642 nm. The objective used for this measurement was the oil objective with NA=1,49. With the help of equation 2.76 and the laser wavelength of 473 nm, one can calculate the diameter of the laser focus to $d_{laser} = 193$ nm. When compared to the dimensions of the antenna depicted in figure 5.1, one can see that the elements have distances smaller than the diameter of the laser focus. This means, that for a typical spectrum (and also BFP image), several antenna elements are illuminated, which is an explanation for the very broad peak in the laser-driven spectrum of the antenna. The spectrum of the antenna is an overlap of the spectra of several different antenna elements.

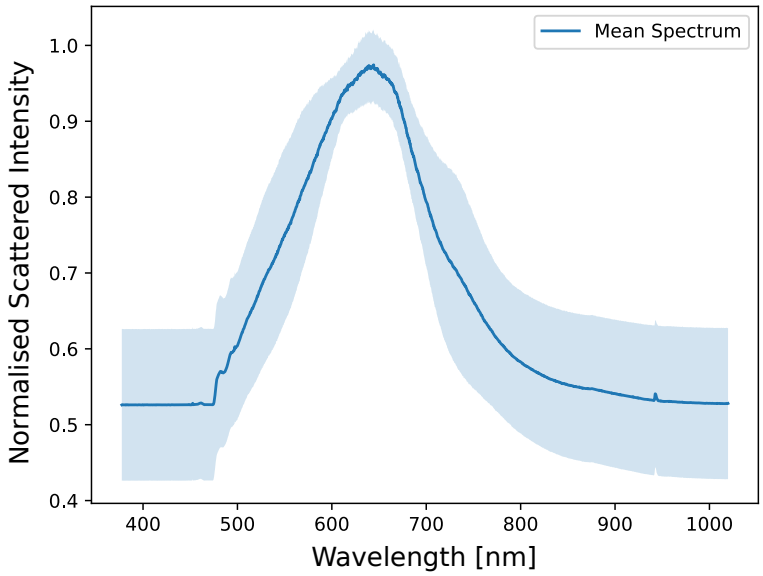

Figure 5.3: Mean normalised laser spectrum of 23 antennas with standard deviation intervals.

Additionally, spectra have been recorded with the white-light DF setup (see chapter 3.1). The spectrum of one antenna can be seen in figure 5.4 (blue spectrum). It is noticeable that the peak has shifted from 642 nm over 100 nm to 751 nm. The spectrum still is very broad, hinting at the multiple antenna elements which are illuminated.

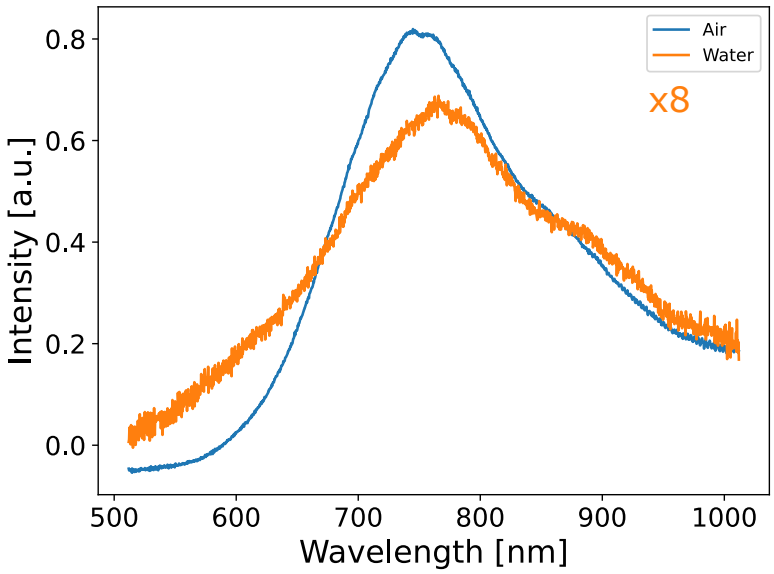

Figure 5.4: DF spectra of a Yagi-Uda-antenna. In blue: the antenna is in air. In orange: the antenna was covered with a water drop. The intensity severely decreased due to the absorption in water and reflection of light at the water surface. Because of that, the intensity of the spectrum in water has been increased by a factor of eight. The resonance peak shifts by 15 nm from 751 nm (air) to 766 nm (water).

For the DF spectra, the sample is uniformly illuminated, and the measured structure is determined by an aperture. The DF spectra consist of the intensity from all antenna elements.
It should be noted, that the DF spectrum is a scattering spectrum, while the laser spectrum is from pumping the system with energy through the laser off-resonance and then reemitting the energy corresponding to resonant modes given by the geometry of the gold nanostructures.
Furthermore, a spectrum of the antenna covered by a drop of water has been taken (see figure 5.4 orange spectrum). This spectrum has a much lower intensity due to the absorption of light in water and the reflection of light on the water surface. The intensity of the spectrum has been increased by a factor of eight, to be comparable to the one in air.
The resonance peak is red shifted compared to the spectrum in air by 15 nm from 751 nm (air) to 766 nm (water). This is to be expected since Gans' theory (the solution of Mie scattering for spheroidal particles) predicts the longitudinal plasmon wavelength of a metal spheroid (and in good approximation a metal rod) to be [147]:

$$\lambda_{LSPP} = \lambda_p \sqrt{\epsilon_\infty + \left(\frac{1}{P} - 1\right)\epsilon_d}. \tag{5.1}$$

λ_p is the wavelength corresponding to the plasma frequency in the bulk metal, $\epsilon_d = n_d^2$ is the squared refractive index of the dielectric surrounding the nanoparticle, ϵ_∞ is the high-frequency dielectric constant of the metal, and lastly P describes the depolarisation factor along the long axis of the spheroid (or rod).

According to Yunos et al. [148] the depolarisation P of an elongated ellipsoid can be calculated with

$$P = 4\pi \frac{1-e^2}{e^2}\left(\frac{1}{2e}\log\left(\frac{1+e}{1-e}\right)-1\right), \tag{5.2}$$

where e is the numerical eccentricity that can be calculated with

$$e = \frac{\sqrt{A^2-B^2}}{A}. \tag{5.3}$$

A and B are the half axes of the ellipsoid. With a plasmon wavelength of gold $\lambda_p = 168\,\text{nm}$ [149], a dielectric constant of $\epsilon_\infty = 9,5$ [150], and $A = 120\,\text{nm}$ and $B = 50\,\text{nm}$ the wavelength of the LSPP in an ellipsoid of similar shape as the antenna can be calculated. In water with $n = 1,33$ in the optical regime [151], it is $\lambda_{LSPP,water} = 756\,\text{nm}$, whereas in air with $n = 1$ [152] the calculated wavelength is $\lambda_{LSPP,air} = 663\,\text{nm}$. This would equate to a sensitivity of 282 nm/RIU, where RIU stands for refractive index unit. One can now see that a red-shift is expected of the Yagi-Uda-antenna elements with increasing refractive index of the surrounding. This is the case in the experiment above when going from air with $n = 1$ to water with $n = 1,33$ and results in a sensitivity of the antennas as refractive index sensors of around 45,5 nm/RIU. This is low compared to other works, where a sensitivity of $\sim 40-60\,\text{nm/RIU}$ is seen in gold nanospheres and $\sim 170-290\,\text{nm/RIU}$ for the long axis of gold rods [153, 154].
Nevertheless, measurement series were carried out with Yagi-Uda-antennas incorporated into a microfluidic flow cell (see chapter 4.3). A total of six flow cells were fabricated on which seven measurement series were taken, however none of them showed the desired refractive index shift at the time where the medium was changed.
For the measurements, spectra were taken every 15 s for the same integration time. The measurement started with water in the flow cell, and measurements were taken for 10 min. Following that, the liquid was changed to a water/glycerol mixture with 9% glycerol. From there on, the liquid was changed every 10 min, alternating between pure water and a water/glycerol mixture. The remaining weight percentages of glycerol were 17%, 24% and 32%. These percentages were chosen, since the refractive indices of these mixtures should increase in 0,012 steps compared to that of water [155].
A representative DF spectrum of the measurement including fits of three peaks can be seen in figure 5.5. Noticeably, the spectrum has more peaks than the one in figure 5.3 with a major peak at a wavelength of 659 nm, which is more comparable to that of the laser spectrum. The second peak is at a wavelength of 752 nm and the third at 921 nm.

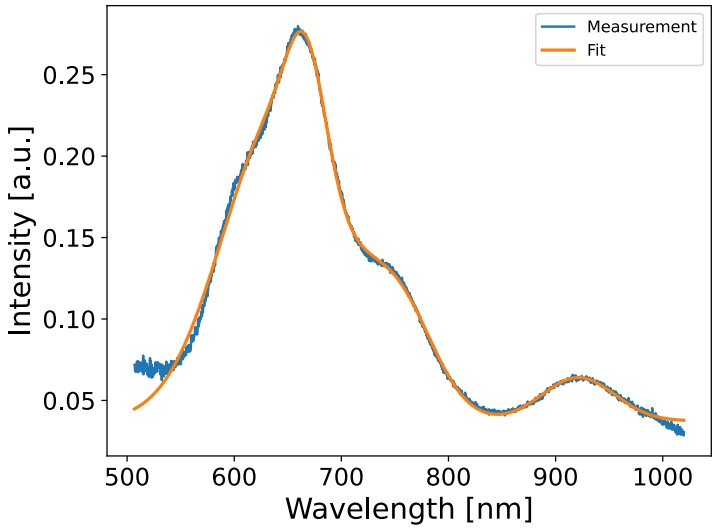

Figure 5.5: DF spectrum of Yagi-Uda-antenna in the flow cell filled with water.

Three peaks were fitted for all single spectra of the long-term measurement. The peak position of the peaks around 650 nm and 920 nm were plotted over time, which can be seen in figure 5.6. While jumps in the resonance frequency can be seen for both peaks, the jumps are not always consistent with the points in time where the liquid is supposed to change, as well as with the direction in which the resonance frequency is expected to shift. Noticeable jumps in both peaks can be seen at the 15, 22, 25, 35, 40, 53 and the 64 min mark. However, measurements were carried out in several parts, starting with a 5 min measuring block, followed by 10 min measurement blocks so that changes in refractive index fall into the middle of one block. This means, that the jumps at times which end on five are probably measuring artefacts, from the end and start of one measuring block. It was tried to not move the sample over the whole course of the measurement, only the one end of the tube of the peristaltic pump was put into the different containers with different liquids.

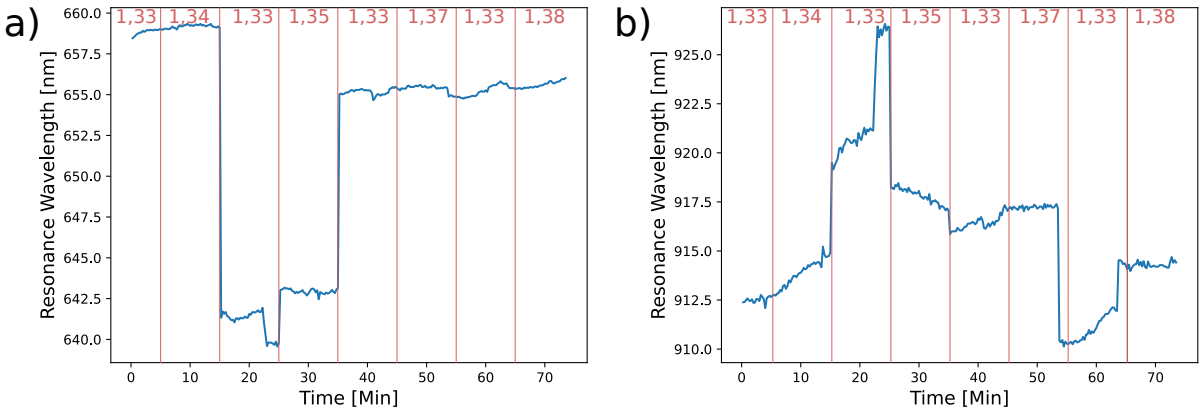

Figure 5.6: Peak positions of the fitted spectra over the course of one measurement cycle. a) Fits of the major peak around 650 nm. b) Fits of the minor peak around 920 nm. The red vertical lines indicate a change in medium. The red numbers are the refractive index of the present medium.

However, while there was no active movement of the sample, the stage drifted over the course of the measurement, so that the sample moved out of the measurement spot in x- and y-direction as well as out of focus. This movement of the stage has been corrected between different measurement steps, since otherwise no signal would be detected at the end of the measurement. This correction should not cause a shift in resonance wavelength, only the intensity of the measured spectra should be influenced.
In these measurements, next to no change in resonance frequency could be measured at the points of interest (at each 10 min mark). From the previous measurement, a sensitivity of 45,5 nm/RIU was measured, which should amount to a resonance frequency change of 2 nm between water and the 32% mixture, however, the expected sensitivity could not be seen. A possible explanation for that is that during the assembly of the cell, the antennas were damaged or covered in residue of the PMMA, which would make them inaccessible to refractive index changes. Another idea for the measurement of refractive index changes is to have a look at BFP measurements and changes in emission of the antenna with changing surroundings.

5.3 Back Focal Plane Measurements

BFP images were taken with the setup described in chapter 3.2 under laser illumination. The laser intensity is reduced by a grey filter with optical density of 1 to prevent altering/melting of the delicate gold structures. However, a compromise had to be found between signal strength and local heating of the sample. For measurements with quantum dots (QDs), the intensity can and should be reduced even further to reduce photo bleaching of the QDs.
Before measurements, the laser had to be aligned with the optical axis, so that the laser does not illuminate the sample already under an angle, which can be seen in the BFP image. To adjust the laser, the two mirrors which guide the laser beam into the microscope have to be adjusted. The mirror further away from the microscope (or closer to the laser) shifts the laser beam path, whereas the upper mirror tilts the beam. Only with a combination of both mirrors, a parallel laser beam can be achieved on the desired sampling region.
To filter out the laser signal from the BFP images, two notch filters (for a wavelength of 473 nm) are placed into the beam path. One is fixed in the microscope, another after the Bertrand lens on a flip mount. It can be of advantage to flip out this filter for beam adjustment, so that the laser spot can be better seen in the camera.
BFP images are taken in pairs of background measurements and antenna measurements. After adjusting the sample into the optimal position for measurement, the sample gets moved by a fixed amount (usually 10 µm) via the piezo stage away from the antenna. The Betrand lens, attached to a flip mount, is brought into the beam path. On an empty spot, a BFP image is taken with an exposure time of 15 s. Without touching the Bertrand lens, the piezo stage is moved back again, so that the antenna is in the laser focus and another BFP image is taken. The background measurement is subtracted from the sample measurement, a resulting image can be seen in figure 5.7.

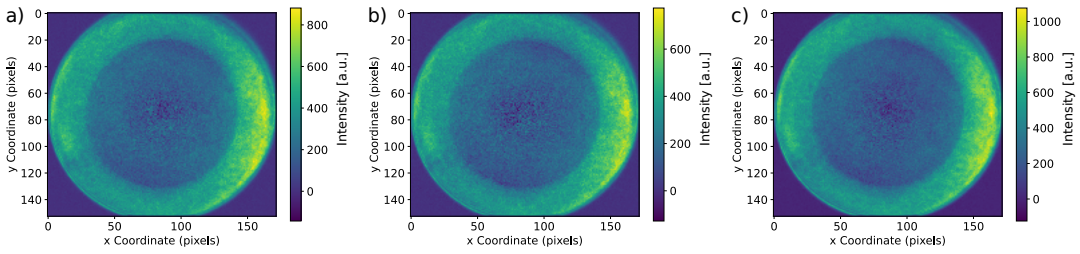

Figure 5.7: Background corrected and cropped BFP image of a standard antenna structure illuminated with laser light polarisation a) circular, b) parallel to the feed structure and c) perpendicular to the feed structure.

The polarisation of the laser light is parallel to the plane of the optical desk after passing the polarising beam splitter and can be manipulated with half- and quarter-wave plates before coupling into the back of the microscope. To achieve a linear polarisation along the line of sight when standing in front of the microscope, a half-wave plate was installed into the beam path and turned to an angle of 45°, which effectively rotates the polarisation plane by 90°.
For the majority of the measurements, the antennas were oriented in a way, that the

single elements of the antennas are parallel to the line of sight when standing in front of the setup, with the directors pointing to the right side.
The maximum driving efficiency is expected for the polarisation parallel to the feed element of the antenna. To confirm this, a series of measurements has been conducted with the polarisation parallel and perpendicular to the feed element, as well as with circularly polarised light.
With the help of the analysis method described in the following chapter 5.4, the front-to-back ratio (f/b ratio) as well as the directivity equivalent for these measurements have been calculated. For illumination with light parallel to the feed element, a f/b ratio of 1,25 was achieved as well as a directivity of 4,76. For illumination with polarisation perpendicular to the feed element, a lower f/b ratio of 1,13 has been measured as well as a directivity of 3,77. For circularly polarised light, the f/b ratio was measured at 1,19 with a directivity of 4,34.
This matches with the expectation, that the antennas are best driven with light polarised parallel to the elements. Due to this, measurements are from there on taken with light in this polarisation. However, it should be noted, that the half-wave plate orientation also has to change for changed antenna orientation.

5.4 Analysis of BFP Images

The analysis of the acquired BFP images was carried out with a script written in Python. In this section, the idea behind it is shortly described. Parts of the code were taken from [156].
After reading in the measurement and background data, the background gets subtracted from the antenna signal. Now the image has to be manually cropped in such a way that the centre of the BFP signal is also the centre of the image. Furthermore, a cut-off intensity is assigned, so that all pixels outside the BFP signal get assigned a value of zero. For analysis, the image is first transformed from a Cartesian coordinate system into a polar coordinate system (see figure 5.8).

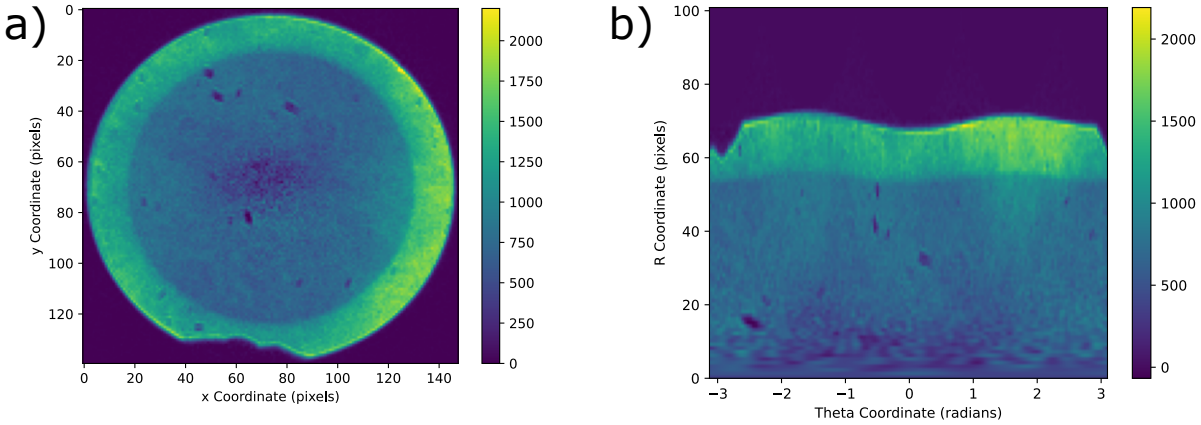

Figure 5.8: a) Cropped BFP image in Cartesian coordinates. b) Cropped BFP image in polar coordinates.

From there on, the sum of the radial slices (which are now columns in figure 5.8b)) can be taken and plotted in a polar coordinate plot (see figure 5.9). Following that, the angle of maximum emission can be extracted. To extract the angle of maximum emission, first the angle of highest sum value gets chosen. However, since the measurement is noisy, the values around that angle of maximum sum should be involved too, to find the true emission angle. To do so, the weighted average of all the angles $\pm 45^\circ$ around the maximum sum angle was taken and used as the true angle of highest emission $\alpha_{\text{max,weighted}}$. The weighted average is calculated with:

$$\alpha_{\text{max,weighted}} = \frac{\sum_{i=\alpha_{\text{max}}-45^\circ}^{\alpha_{\text{max}}+45^\circ} \alpha_i \cdot I(\alpha_i)}{\sum_{i=\alpha_{\text{max}}-45^\circ}^{\alpha_{\text{max}}+45^\circ} I(\alpha_i)}, \tag{5.4}$$

where α_i denote the different angular slices, α_{max} the angle of highest intensity and $I(\alpha_i)$ their corresponding radial intensity sums.

These angular measurements should however only be compared over the course of one measurement series, since antennas can have a slight angle on the substrate as well as the possible placement of the substrate in the measurement setup with

a small offset angle. However, for front-to-back emission ratios different measurements can be compared, when adjusted for the angle of highest emission.

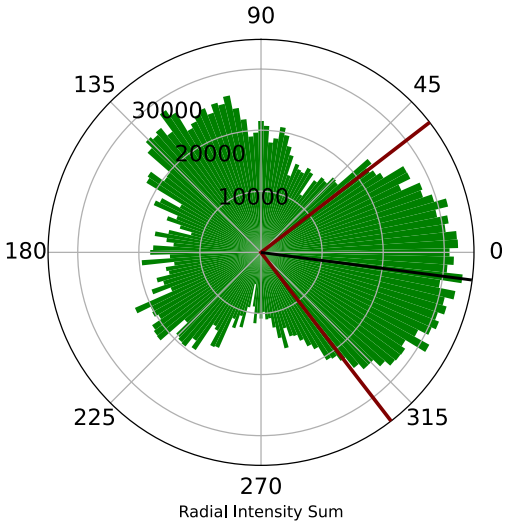

Figure 5.9: Sum of the radial intensities from the centre of the BFP image to the detection limit. The black line depicts α_{max} and the red line the area of angles that are used to calculate $\alpha_{\text{max,weighted}}$.

5.5 Quantum Dot coupling

To drive the antennas with maximum efficiency, it was tried to place quantum dots (QDs) at one end of the feed element. A placement at the end of such a feed element is preferred due to the high electric mode density at that position [30]. The antenna feed element was designed to be resonant with the emission spectrum of the QDs, which peaks around 650 nm.
To achieve an area-selective bonding, two effects were tried to combine: a mask was applied, that only leaves the ends of the feed elements uncovered, and a chemically selective binding process, which should not bind the QDs to the substrate but only to the antenna element itself.

5.5.1 PMMA

As masks, several materials and preparation techniques were tried in various combinations. As a first attempt, samples fabricated out of gold on a glass/ITO substrate were taken, and an additional layer of PMMA was spin coated on top. Moreover, the antenna fields were surrounded by four markers (one in each corner) consisting of two rectangles touching each other at one corner. For the help of orientation on the sample, the rectangle closer to the antenna field was smaller. The touching point of the rectangles functioned as marker for alignment in the SEM for a second lithography step. In this step, the top half of the feed elements was exposed. After a development step in MIBK and isopropanol (1:3 for 65 s), parts of the feed elements are supposed to be uncovered. Results of the double exposure can be seen in figure 5.10.

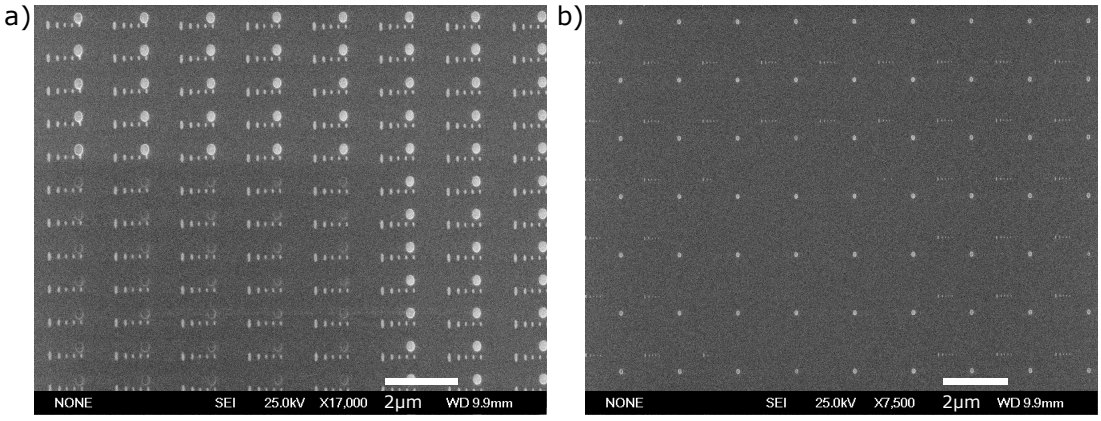

Figure 5.10: Antenna structures with an additional PMMA layer on top for double exposure. a) Bright oval spots are the exposed structures in the PMMA mask. The alignment is off, even for very dense antenna arrays, however sometimes overlaps with other antenna parts than the feed. b) Bright spots are again the exposed structures in the PMMA mask. This time the alignment is even farther off and does not touch the antennas at all.

Even after several attempts with dense and loosely packed antenna arrays, a perfect alignment could not be achieved. For dense arrays, the double-exposed areas sometimes overlapped by chance, however for antennas with larger spacing, which were of interest for single antenna measurements, they were never exposed at the right regions.
One idea, to still achieve some overlap, would be a lattice constant smaller or larger than the one of the antennas. This way, at no point would all antennas and holes overlap, however antennas with multiples of both lattice constants (bar an offset at the beginning of the lattice) should align well. Otherwise, one could go even further and vary the lattice constant of the second exposure in order to achieve overlap at some structures.
A technique not accessible at the used SEM, is a laser interferometer stage such as the one offered by Raith GmbH [157], which can align patterns in the low nm regime.

5.5.2 HIM and Chromium

Instead of taking a pseudo-random approach and pick out the best fits, another possibility is the use of the HIM. With the help of the HIM, holes can be etched into a mask precisely at the area where they are needed. Different configurations have been tested out again. Firstly, gold antennas on a glass/ITO substrate were tested with a 10 nm layer of chromium (Cr) on top. In the HIM, holes with dimensions of 100 nm $\times$ 100 nm were etched into this layer, slightly overlapping the feed element and the substrate area above it.
The process of linking the QDs to the antennas was the same for all different mask approaches. It was started by creating a solution of 20 ml water with one drop ($\sim$ 5 µl) of 3-mercaptopropionic acid (3-MPA). The sulphur ligand of the 3-MPA molecule binds strongly with the gold surface [158], while the other end can bind to the QD. To bind the 3-MPA linker molecule to the gold surface, the whole sample is submerged in the acidic solution for 30 min.
For the QDs a stock solution is first prepared consisting of 5 mg dry QDs (650 nm emitting cadmium selenide/zinc sulphide (CdSe/ZnS) quantum dots by PlasmaChem GmbH) that are dissolved in 15 ml hexane. From that stock solution, 1400 µl are again mixed in 15 ml hexane to prepare the QD solution for the antenna samples. The samples are taken out of the 3-MPA solution and dried with nitrogen, before fully submerging in the QD solution. There the samples stay covered for 24 h at room temperature. Samples can be cleaned in acetone and isopropanol afterwards.

The chromium mask was removed in chrome etch (TechniEtch Cr01 by MicroChemicals GmbH). After submerging the sample for 30 s, the chromium film is vanished completely. However, while the etchant does not dissolve most photoresists and the used QDs, it apparently does attack the ITO layer on which the antenna structures are fabricated. As a result, the sample was stripped of nearly all structures and is destroyed.

As an idea to circumvent this problem, samples were fabricated on a substrate without ITO layer. However, now an additional layer of a conductive resist had to be spin coated on top of the PMMA to prevent charging effects in the SEM. Electra 92 (AR-PC 5090) by Allresist GmbH was applied by spin coating the resist at 4000 rpm for 60 s, followed by a curing step at 105 °C for 2 min. Also, an additional 3 nm layer of either chromium or titanium is needed to ensure adhesion of the gold to the glass. Since the sample is expected to be submerged in chrome etch, titanium is chosen here as adhesive material.
The Yagi-Uda-antenna sample was again coated with a 10 nm layer of chromium and prepared in the HIM (the chromium layer provided enough conductivity to prevent charging in the HIM). However, after the etching step still no QD signal could be measured in the DF setup with the laser as illumination source.

5.5.3 HIM and Titanium

As chromium appeared to not be suitable as a masking material, further tests were conducted. As a next easy-to-apply material titanium was chosen and tested. Fabrication steps are the same as the ones for chromium masks. The removal of the titanium layer however was conducted in a solution of ammonium (28% by Merck KGaA) and hydrogen peroxide (30% by Carl Roth GmbH+Co. KG) (3:1). The samples were submerged until the titanium layer was not visible to the eye any more, which could take from 30 s up to 5 min. The highly unstable, unreproducible etching rates can stem from inaccurate mixing of ammonium and hydrogen peroxide, however the solution was poured from one container to another at least four times to mix the solution thoroughly.
Another cause for the unpredictable etching rates could be the varying degree of oxidation the titanium layer has endured. An indication for this being the case is that the etching does not appear to be linear, but rather contains a period where no etching is visible, followed by a rapid etching where the sample clears up in a matter of several seconds.
For samples with an ITO layer, the layer appears to be attacked in long etching processes. This effect and the unreliability of the process made this masking process not viable either.

5.5.4 HIM and Aluminium

As a last masking material, aluminium was tested. Again, a 10 nm thick layer was applied over the sample and treated in the HIM. To remove the aluminium, the samples were placed in a KOH solution (10 % by weight) for 20 s. Although KOH can also attack the ITO layer, low etching times prevent the samples from too much damage. With this method, signal of the QD could be seen in the spectrum (see figure 5.11, however the signal was low and only visible on three of sixteen antennas. Furthermore, no forward directivity could be seen in the BFP. It is possible, that the sample got contaminated in the several process steps (especially during the etching in HIM) so that good plasmonic properties cannot be ensured any more.

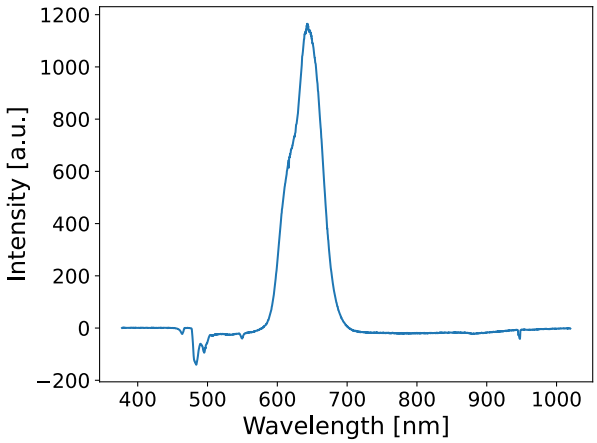

Figure 5.11: Laser driven spectrum of a QD coupled to the feed with the help of an aluminium mask.

5.6 Manipulation of BFP

Chapters 5.6 and 5.7 are building on ideas from discussions with the collaboration partners Anne-Laure Baudrion from University of Technology of Troyes and Dai Zhang from the Institute for Physical and Theoretical Chemistry in Tübingen.
During the course of this work, it was tried to manipulate the emission pattern of the Yagi-Uda-antennas. To do so, antennas were placed in media of different refractive indices. First, the antennas were incorporated into a flow cell, so that the medium on top of the antennas could be changed in situ from air to water or mixtures of water and glycerol in different ratios. This changes the polar angle with which the antenna emits light.
Additionally, it was tried to cover the antennas only halfway with different material, from PMMA to ITO to silicon dioxide. This way, a change in emission in the azimuthal angle would be expected.

5.6.1 Flowcell

Measurements in flow cells were carried out with the setup described in 3.3. As a first experiment with the easiest setup, Yagi-Uda-antennas of standard dimensions (see figure 5.1) were incorporated into a flow cell. In intervals of five minutes, water and mixtures of water and glycerol were pumped through the flow cell. Beside measuring the spectral response (see chapter 5.2), BFP images were taken each time water or one of the mixtures flooded the cell.
To get an idea of what to expect as a result of the experiment, FDTD simulations were carried out on Yagi-Uda-antennas with air, water and glycerol as surrounding medium. The far-field emission into the glass substrate was recorded. The far-field projection of highest intensity was for air at 700 nm, for water at 635 nm and at 660 nm for glycerol and can be seen in figure 5.12.

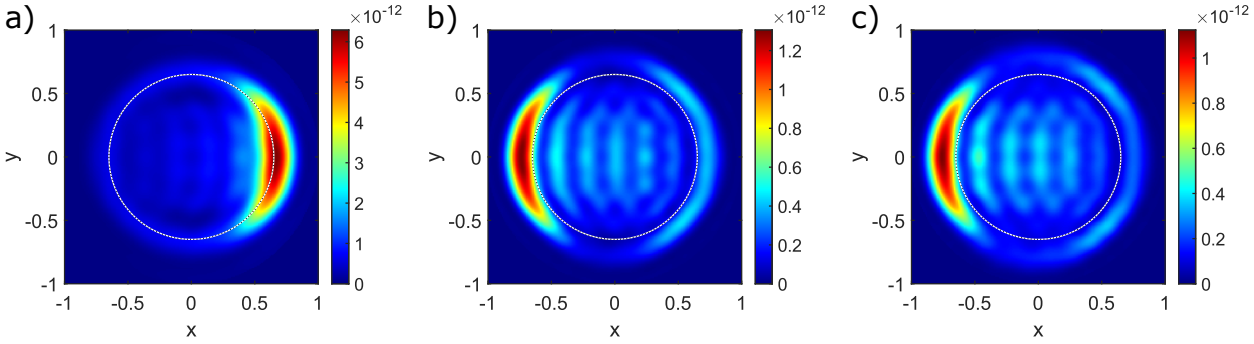

Figure 5.12: Far-field projection of the near-field simulated with FDTD. A circle of radius 0,65 is drawn as guide to the eye. a) Antenna in air, b) in water, c) in glycerol.

The most remarkable result is, that the emission direction changes by 180° from the side of the directors (as it is originally intended) to the side of the reflector. Due to the different refractive indices of water and glycerol (compared to air), the effective detuning of the antenna elements (see equation 2.54), as well as the effective wavelength in the medium changes in such a way, that constructive interference of reemitted light from the excited antenna elements happens in backwards direction. The simulated maximum emission direction of the antenna in air is for a polar angle of $\theta_{\text{max,air}} = 62{,}0°$.

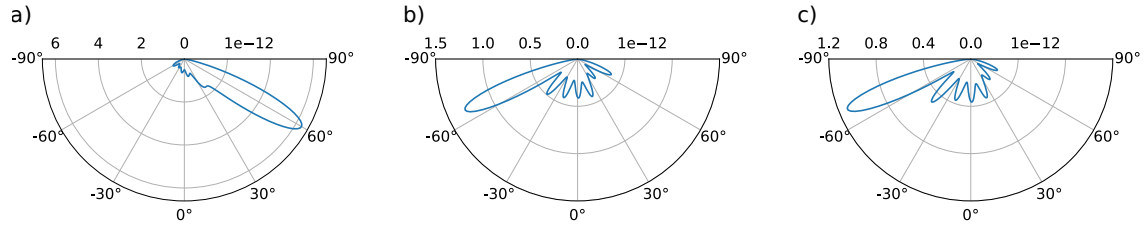

Figure 5.13: FDTD simulated polar emission of the antenna. Side-view of the antenna emission into the substrate. a) Antenna in air. Maximum emission angle of 62,0°. b) Antenna in water. Maximum emission angle of –65,6°. c) Antenna in glycerol. Maximum emission angle of –68,3°

The difference between the emission in water and glycerol however is more subtle. With the help of the circle of radius 0,65 one can see that the maximum of emission shifts outwards to higher angles compared to air. While the emission for antennas on glass in air is at the radius of the circle, it already moved out for water as medium to $\theta_{\text{max,water}} = -65{,}6°$ and shifts even a little bit further for glycerol to $\theta_{\text{max,glycerol}} = -68{,}3°$. Looking at the emission of a dipole on a planar interface (see chapter 2.6) one would expect such behaviour, until the refractive index of the medium matches that of the glass, in which case the emission is straight in the forward direction again.

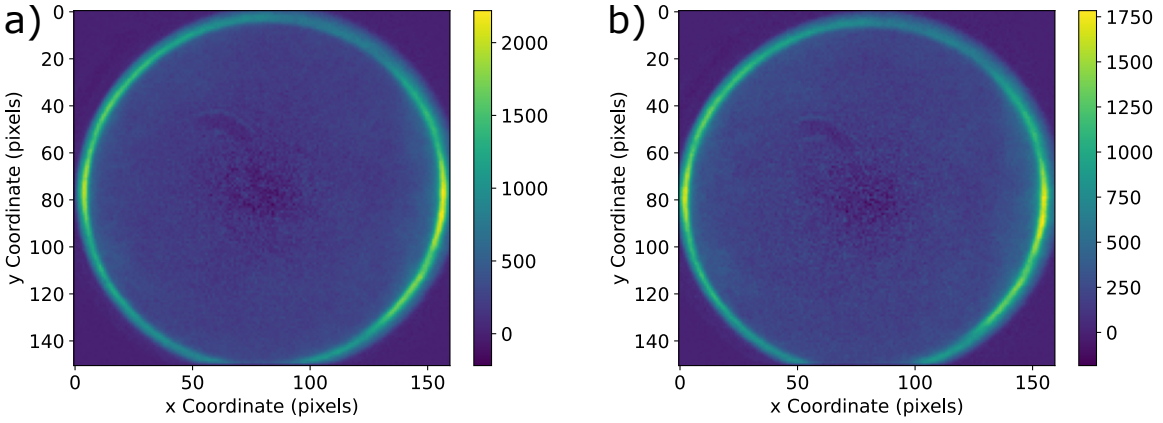

Figure 5.14: BFP images of Yagi-Uda-antennas in a flow cell. a) Antenna covered in water. b) Antenna covered in glycerol.

Looking at actual measurements of the antenna emission from antennas incorporated into flow cells, this behaviour could not been replicated. In figure 5.14 one can see the BFP image of a Yagi-Uda-antenna covered by water and by glycerol. An inversion of the direction of emission can not be seen, with the highest intensity still in the direction of the directors.
Despite the very high NA of 1.49 of the objective, it still is only barely possible to observe the forbidden zone, although the critical angle of $\alpha_{\text{crit}} = \arcsin(1,33/1,52) = 61{,}2° < 78{,}98°$ is smaller than the opening angle of the objective. The in the simulation already subtle differences in the polar angle of emission cannot be resolved to a high enough degree to use this metric for sensor applications.

5.6.2 Half-Covered Antennas

A different approach is to use the manipulation of the azimuthal angle instead of the polar angle as measurand. To do so, half of the antenna (meaning half of each element; see figure 5.15a)) can be coated in a high refractive index dielectric. The emission of the antenna should then be refracted more into the direction of the high refractive index material. When submerging the antenna in liquid with higher refractive index than air, the refractive indices surrounding both antenna halves should approach each other again, and emission should again move towards the straight forward direction.
Again, to get an idea of what to expect in the experiment, FDTD simulations have been carried out. The setup and result of the far-field projection can be seen in figure 5.15. Here, half of each antenna element was covered from the top and all sides with a dielectric of refractive index n=1,9. In the far field projection of the emission, one can see a 5,2° deviation of the emission in polar direction from the forward direction of the antenna assembly.

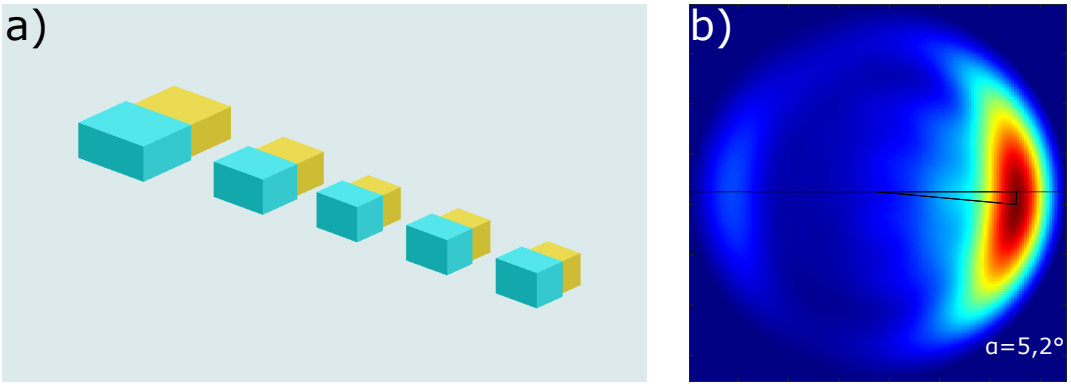

Figure 5.15: a) FDTD Simulation setup for half-covered antennas. b) Far-field projection of the FDTD simulation. The maximum of emission diverges around 5,2° in azimuthal direction from the forward direction of the antenna assembly.

The antennas were fabricated with the help of the HIM (see chapter 4.2). All antenna elements were first covered by 10 nm of SiO_2 during the thermal evaporation process step before the lift-off. One side of each antenna element was then etched free of the SiO_2 layer in the HIM (see figure 4.7).
Measurements were done on antennas prepared as described above as well as on antennas still completely covered with SiO_2 as a reference. For each antenna, five corrected BFP images were taken for the antenna in air and covered by a drop of water. Exemplary BFP images of one half-covered antenna can be seen in figure 5.16.
In the BFP images it can already be seen, that the angle of emission has changed. As already seen in chapter 5.6.1, the angle of total internal reflection moves outwards, so that only a small outer ring where the highest intensity is concentrated can be seen.

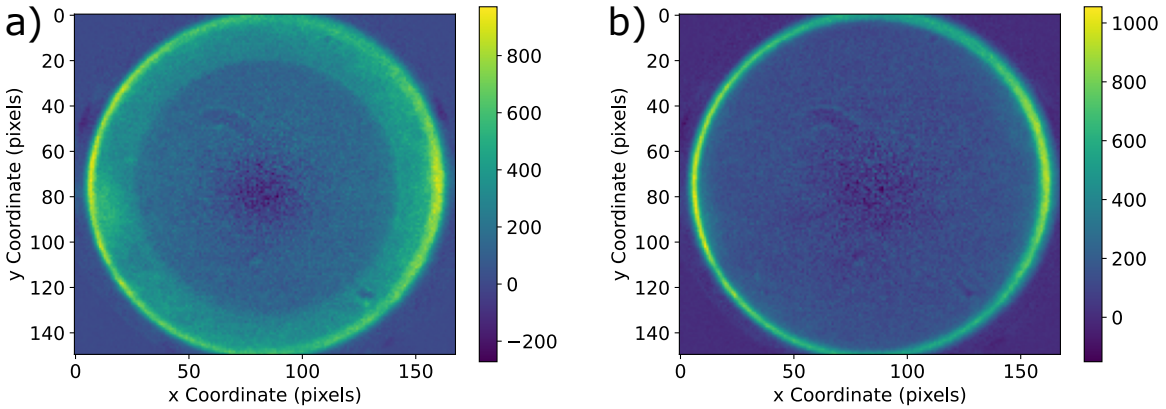

Figure 5.16: BFP images of a Yagi-Uda-antenna, where half of each antenna element is covered by a 10 nm layer of SiO_2. a) BFP image of the antenna in air. b) BFP image of the antenna covered by water. The emission direction moves slightly to higher values of the polar angle.

More interesting, however, is that also the azimuthal angle of emission appears to be changing. From now on, the azimuthal angle will be given with respect to the x-axis, which denotes 0°. Despite not moving the sample between measurements, it could be possible that this change in emission direction stems from a movement of the sample, for example when putting the drop of water onto the surface. Therefore, the emission direction of the fully covered antenna is used to adjust and correct the emission directions of the half-covered antennas. The emission direction of the covered antenna can be subtracted from the emission angles of the half-covered antennas, to correct for systematic errors.
The fully coated antenna showed azimuthal angles of maximum emission in air $\varphi_{\text{full,air}}$ and in water $\varphi_{\text{full,water}}$ of:

$$\varphi_{\text{full,air}} = 3,4 \pm 2,0^\circ \tag{5.5}$$

$$\varphi_{\text{full,water}} = 7,1 \pm 6,5^\circ. \tag{5.6}$$

There appears to be a rotation of the sample of around 3,7° between the measurements. This amount of deviation in emission direction should therefore be

accounted for as a systematic error in the other measurements. It should also be noted that the high standard deviation of the antenna covered in water comes from one bigger outlier. SEM images and tables of the emission angles of the covered and half-covered antennas as well as BFP images and emission patterns can be found in the appendix.

For the first half-covered antenna (antenna 1_6), the following azimuthal emission angles were measured:

$$\varphi_{1\_6,\text{air}} = 1,4 \pm 2,2^\circ \tag{5.7}$$
$$\varphi_{1\_6,\text{water}} = 15,1 \pm 6,3^\circ. \tag{5.8}$$

Even when correcting for a systematic error of 3,7°, the change in emission angle for the half-covered antenna appears to be significant. The difference in emission angle from uncovered to covered with water is 10° even with the systematic error of 3,7° subtracted. It should also be noted, that the shift of the azimuthal emission angle is in the right direction, towards the uncovered half of the antennas, albeit higher than expected from the simulations. Additionally, the shift is so big, that it crosses the normal direction of the antenna and is emitting into the direction of the uncovered half of the antenna, despite the refractive indices of both antenna halves approaching each other. An explanation of this behaviour cannot be given.
A linear relation between the emission angle and the refractive index can not be assumed, especially for higher angles. A sensitivity in units of °/RIU is therefore not sensible, but would come out to 30,3 °/RIU for this antenna.

The second half-covered antenna (antenna 1_7) has the following azimuthal emission angles when covered in air or water:

$$\varphi_{1\_7,\text{air}} = 2,5 \pm 1,7^\circ \tag{5.9}$$
$$\varphi_{1\_7,\text{water}} = 22,2 \pm 4,7^\circ. \tag{5.10}$$

The change in emission direction is again in the right direction, towards the uncovered half of the antenna. However, the systematic-error-corrected difference in emission direction for air- and water-covered antenna is 16°, which appears to be very high and again shifts the emission over the normal direction of the antenna towards the direction of the uncovered half.
The linear sensitivity for this antenna would be 48,5 °/RIU. An additional systematic error in the measurement can not be ruled out. It should however be stated, that due to the fabrication process in the HIM every single antenna is unique, so a deviation in behaviour is not only unlikely, but rather expected.
Of the 23 in the HIM prepared antennas, only three were deemed good enough to be measured optically, of which two showed the above described behaviour and one showed an inconclusive behaviour.

For future experiments, the antennas could be incorporated into a flow cell, to further increase the versatility of the system, leading to an easier change of liquid and therefore refraction index surrounding the antenna, without the need of moving the

antenna. Additionally, the uncovered half of the antenna could be prepared with a linker molecule, so that a biosensor can be realised similar to [11]. An advantage of this system compared to others would be the access to two different measurement parameters: the azimuthal angle of emission and the plasmon resonance frequency.

5.7 Second Harmonic Generation

The samples presented in the following chapter were designed and fabricated by the author of this thesis, the here presented measurements and figures were made by Felix Schneider of the group of Alfred J. Meixner and Dai Zhang at the University of Tübingen.

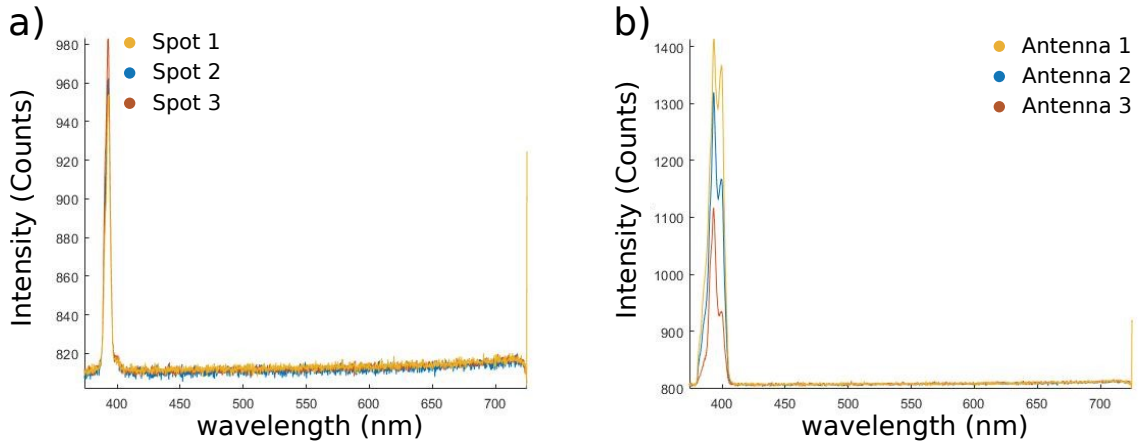

Figure 5.17: Three spectra were taken of the following configurations. A 780 nm short-pass filter suppresses the laser signal. a) Spectra of the silicon substrate. An additional 390 nm band pass filter is introduced. b) SHG spectra of three antennas. A 390 nm band-pass filter suppresses the PL signal.

Measurements of standard Yagi-Uda-antennas made of gold on a silicon substrate were performed in the parabolic mirror setup (see chapter 3.4). For a first characterisation of the second harmonic (SHG) and photoluminescence (PL) signal, laser spectra in the parabolic mirror setup were taken of the silicon substrate and of the gold structures.
For these first measurements, the laser power was set to 32 mW with an acquisition time of 10 s. As a reference, a spectrum of the silicon substrate was taken, with a 780 nm short-pass filter to suppress the laser, and with an additional 390 nm band pass filter, to suppress any PL signal. Measurements were later duplicated on three antenna structures instead of the silicon substrate.
For the antenna structures, the PL signal is suppressed greatly, however even within the range of the band pass filter SHG and PL effects are observed.
Additional to the spectra, BFP images were taken of the background and antenna structures.
BFP images of the silica substrate and the combined PL and SHG were recorded as a reference and for background correction. Then, measurements on the antennas were carried out with a band-pass filter inserted before detection, to ensure that most of the signal is SHG and not PL. An exemplary image can be seen in figure 5.18.

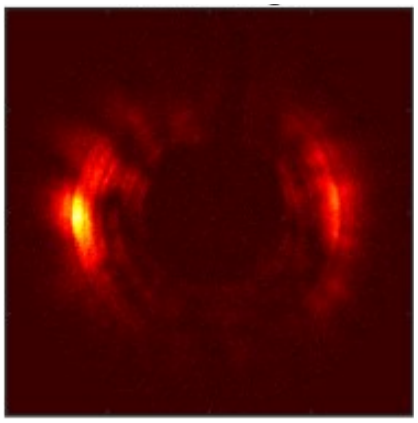

Figure 5.18: BFP image of an antenna on silicon substrate with 780 nm short pass filter and 390 nm band pass filter. The BFP image consist mostly of SHG signal.

The antenna shows clear directivity of emission to the left side, with only very weak emission into the right direction. Contrary to the BFP images without the band pass, the BFP images of different antennas look more uniform to one another. Also, the isotropic emission observed in the reference measurement is greatly reduced, which suggests that this emission predominantly stems from PL.

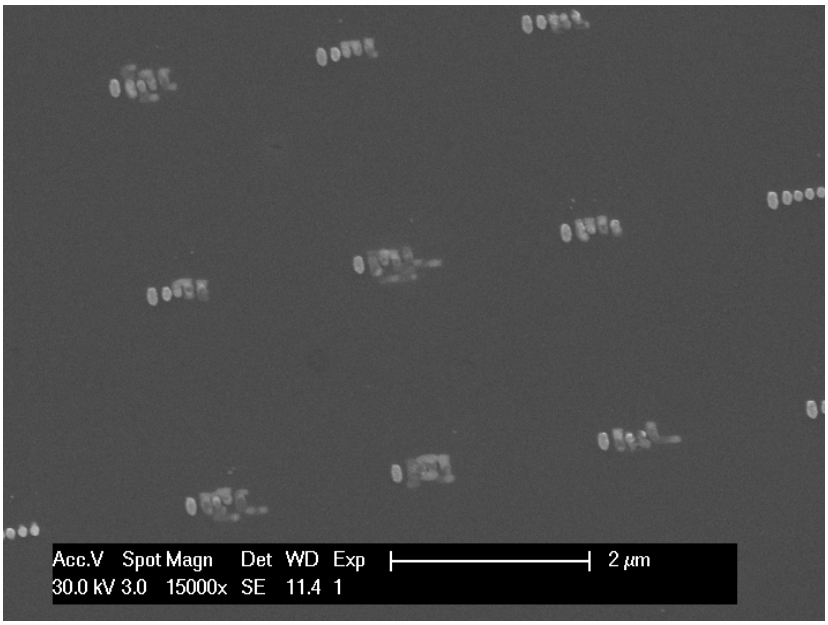

Figure 5.19: SEM images of the antenna structures on silicon substrate, which melted during BFP measurements with high laser powers in the parabolic mirror setup.

It should be noted, that these measurements were not replicable on the exact same antenna structures. A look onto these structures in the SEM (see figure 5.19) after the measurements revealed that the high laser power did indeed melt the delicate gold structures. Lower laser powers were used from here on.

Additional to these measurements, the antennas were illuminated by linearly polarised laser light of different orientation. The spectra series of one antenna can be seen in figure 5.20
The spectra series was taken at a laser power of 8,6 mW. With the lower laser power, the PL intensities seem to decrease disproportionally compared to the SHG intensity. It can be observed that the highest SHG signal is for illumination with polarisation parallel to the individual antenna elements, which is denoted as the angle of 90° (purple spectra) in this measurement. This suggests, that SHG is most efficient if light is polarised parallel to the long axis of gold nanostructures. A possible explanation could be, that the high local field enhancement of plasmon modes excited by parallel illumination enhances the SHG of the silicon, which is shown to be there even without gold structures. This effect would be similar to the one reported in [146]. However, other effects or simply the generation of second harmonics in the gold structures are very much possible and have been reported before [116, 159, 160].

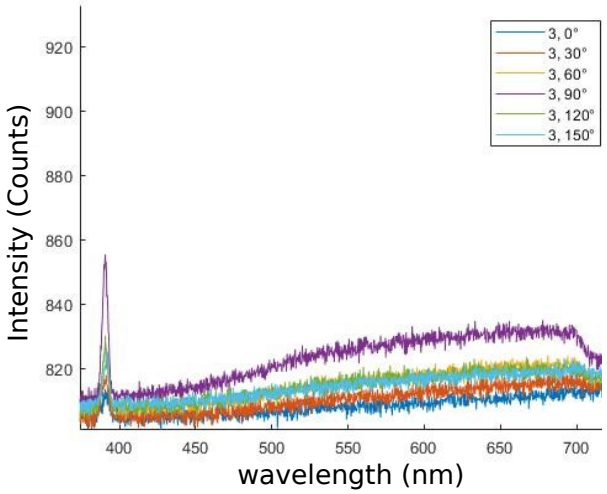

Figure 5.20: Spectra series of an antenna illuminated by linearly polarised laser light. The intensity of the SHG signal is highest for a polarisation angle of 90° (purple spectrum), which is illumination parallel to the antenna elements.

The BFP images of the antennas have a very low signal and a low signal-to-noise ratio, but one can still see some preferred emission into the front and back direction of the antenna structures. Further measurements can be conducted with these antennas, either again with higher powers and the risk of melting the structures but with higher signal, or with longer integration times. Additionally, antenna structures made from aluminium, which are already fabricated, can be measured. Here a lower PL signal is expected since the material has a higher melting point and better plasmonic properties in the wavelength regime of the SHG signal (around 380 nm) [161].

6 Core-Satellite Structures

Core-satellite structures have some interesting properties and advantages, which give them an edge over different, simpler plasmonic structures. They are highly customisable in the material used, the shape of the core and satellite particles, the gap width between core and satellite as well as satellite and satellite, their general arrangement and the way core and satellite link to each other. This makes these particles highly interesting as research objects [53, 40, 162]. The results presented in the following chapter are prepared for publication.
Since most of the effects which are of interest are due to the plasmonic properties of the core-satellite structures, different measurements and simulations have been carried out to achieve a deeper understanding of their characteristics. The simulations and measurements, which are discussed in the following sections, are carried out on particles fabricated by Yingying Cai at the group of Phillip Vana at the University of Göttingen, while some of the measurements are carried out by Benedikt Hettesheimer as part of his bachelor thesis in the group of Monika Fleischer at the University of Tübingen.
The structures all consisted of silica as core material and gold for the satellites. However, the exact sizes and arrangements differed for different samples and also from particle to particle on the same sample. Generally, two different arrangements were considered over the course of this work: the so-called monomer and dimer structures (see figure 6.1). The monomer consist of a single silica particle as core, which is surrounded by typically twelve gold spheres as satellites. The dimer structure consists of two silica core particles, which are together surrounded by typically 20 gold spheres as satellites.

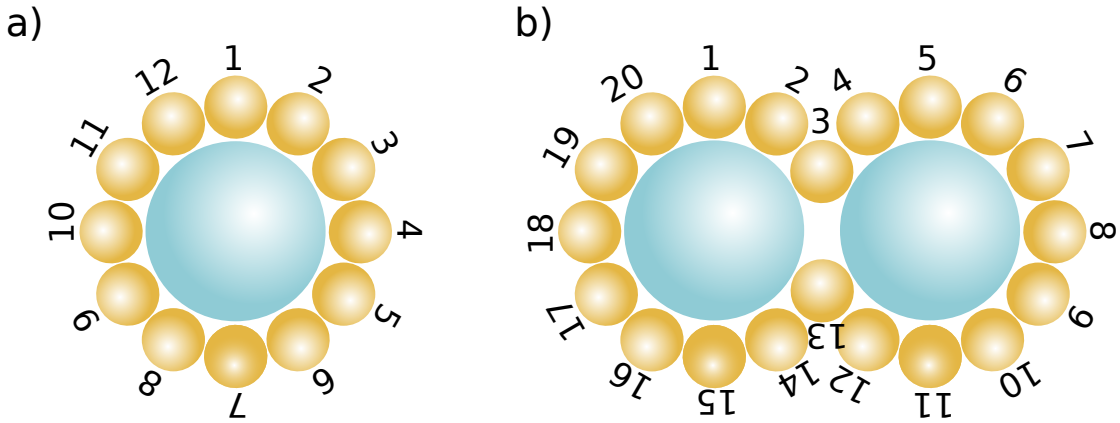

Figure 6.1: a) Monomer structure: a single silica core typically surrounded by twelve gold satellite spheres. b) Dimer structure: two silica particles serve as a combined core, with typically 20 gold satellite spheres surrounding them.

SEM images were taken of several structures to understand the geometry and arrangement of the core satellite nanostructures. The SEM images were typically taken after DF measurements, since the building up of carbon residue on the structures during imaging is not (completely) reversible with an oxygen plasma and can have an impact on the plasmonic response of the particles. In figure 6.2 one can see SEM

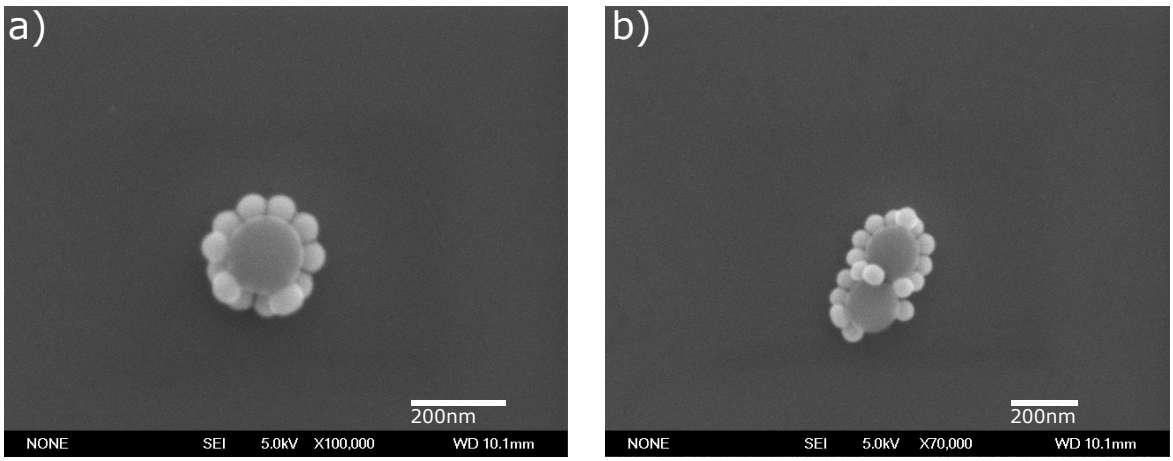

Figure 6.2: SEM images of structures that were cleaned in an oxygen plasma. a) Monomer structure. b) Dimer structure.

images of a) monomer and b) dimer structures. Both structures were found on the same sample, that was cleaned in an oxygen plasma. No silhouette can be seen around the structures, which are visible if the PEG is not removed beforehand.

6.1 FDTD Simulations

Numerical simulations were carried out to understand the different (coupled) plasmon modes, which are excited during the optical characterisation of the samples. To get a model, that is as accurate to the real particles as possible, several SEM images were taken of different structures on one sample, and an average was calculated to evaluate the correct size and arrangement of the 'average particle'.

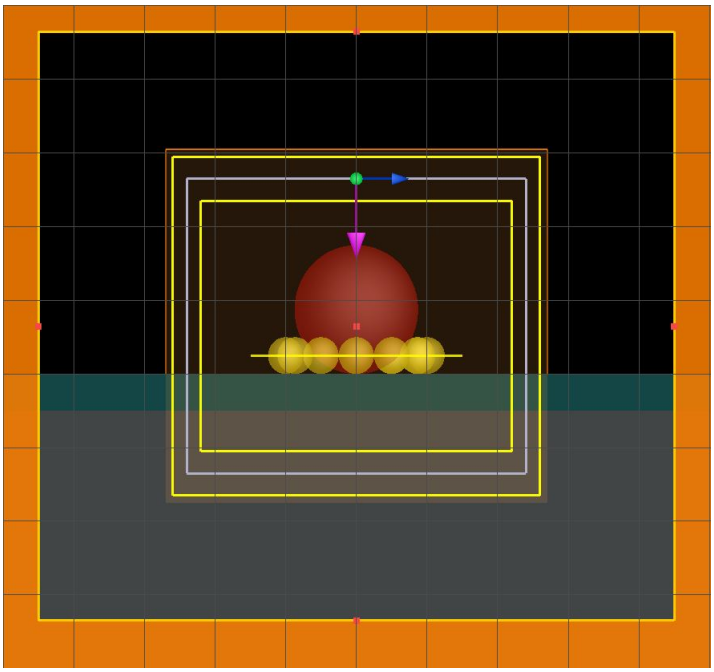

Figure 6.3: Simulation setup for the monomer structure. From outside inwards: the outer orange box is the FDTD simulation area, the inner thin orange box is a finer mesh with 1 nm mesh constant, the first yellow box is the DFT monitor that records the scattering cross-section, the grey box is the plane-wave light source with a pink arrow indicating the propagation direction, a blue arrow for the electric field orientation and a green arrow (here pointing into the plane) indicating the magnetic field direction. Inside the light source is a DFT monitor, that records the absorption cross-section of the simulated structure. The red sphere represents the silica core and the yellow spheres the gold satellites. The thin yellow line is the monitor that records the electric near field. In the lower half, the grey area is the glass substrate and the turquoise area the ITO layer.

The simulations were carried out as FDTD simulations in the software Lumerical by ANSYS. The model consists of a glass substrate with a 50 nm layer of ITO on top. The refractive index of the glass was again taken from [145], whereas the refractive index of the ITO layer was fixed to 1,9.
The monomer was simulated with a central sphere of radius r=87,5 nm consisting of fused silica with a lossless refraction index taken from [163]. It is surrounded by twelve equidistant gold spheres of radius r=25 nm, arranged on a circle of

r=100 nm around the silica core. The refractive indices of gold were taken from [91]. In the z-direction, all particles are placed in such a way, that their lowest point touches the ITO layer. The monomer structure is illuminated by the light of a linearly polarised total-field scattered-field (TFSF) light source of dimensions 480 nm × 480 nm × 400 nm. The frequency of the light source ranges from 400 nm to 700 nm and has a pulse length of 2,66 fs. The mesh constant of the simulation in direct vicinity of the structures is 1 nm.
One DFT monitor is set up inside the light source (dimensions: 440 nm × 440 nm × 340 nm) and is there to record the absorption cross-section $\sigma_{\text{absorption}}$. A second DFT monitor is set up just outside the light source (dimensions: 520 nm × 520 nm × 460 nm) and is there to record the scattering cross-section σ_{scat}. Lastly, a 2D DFT monitor is set up in the plane that is spanned by the centres of the gold spheres. The monitor has a dimension of 300 nm × 300 nm and tracks the electric field in that plane. It gives information about the plasmonic modes of the structure. For the monomer, the rotation symmetry was used and boundaries were set to antisymmetric for the x-axis and symmetric for the y-axis. This way, only a quarter of the whole volume needed to be calculated, which effectively reduced the simulation time by four.
The dimer was simulated with two silica cores touching each other (centre to centre distance of 175 nm). The double core is surrounded by 20 gold spheres also equally distanced around the core. Again, the lowest point of all particles touches the ITO surface. The light source and monitors were set up in the same way as for the monomer structure, except they are 200 nm longer in the x-direction. For the dimer structure, only the symmetry along the x-axis could be used to effectively half the simulation time. A simulation setup can be seen in figure 6.3.

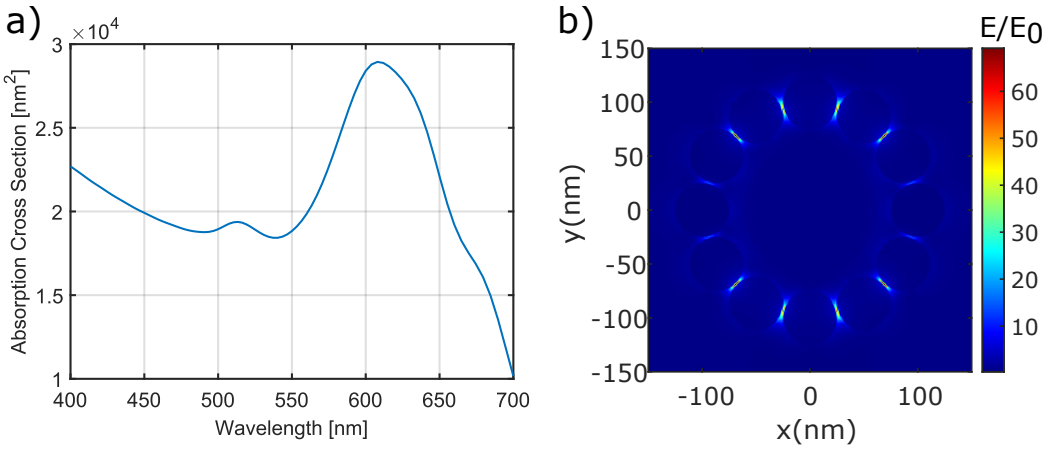

Figure 6.4: a) Simulated absorption cross-section of monomer structure with a minor peak at 510 nm and a major peak at 607 nm. b) Simulated electric field enhancement compared to the incident light. The field enhancement for the major hotspots between the top and bottom spheres and their nearest neighbours is calculated to be 69.

Simulations for the monomer structure were done with light polarised along the x-axis. Since the structure has rotational symmetry, the generality of the problem is

preserved. The absorption cross-section of the monomer structures shows a minor peak at 510 nm and a major peak at 607 nm (see figure 6.4a)). The major peak can be attributed to the mode that can be seen in the electrical field simulation in figure 6.4b). A strong field enhancement is visible between the top and bottom gold spheres and their nearest neighbours. Four minor hotspots can be found between spheres two and three (see figure 6.1a)) and symmetrically equivalent spheres. A field enhancement of 69 is calculated relative to the field strength of the incident light for the major hotspots. For the dimer structure, simulations were carried out for illumination with light polarised along the x-axis (long axis) and y-axis (short axis). For illumination along the long axis, a similar situation as for the monomer structures arises. The absorption cross-section shows a broad major peak at 607 nm and a minor peak a 520 nm (see figure 6.5a)). Again, major hotspots could be found between the top and bottom spheres and their nearest respective neighbours. Eight minor hotspots can be seen in the next neighbouring gaps and low field enhancement on the outermost spheres. For the major hotspots, a field enhancement of 69 is calculated.

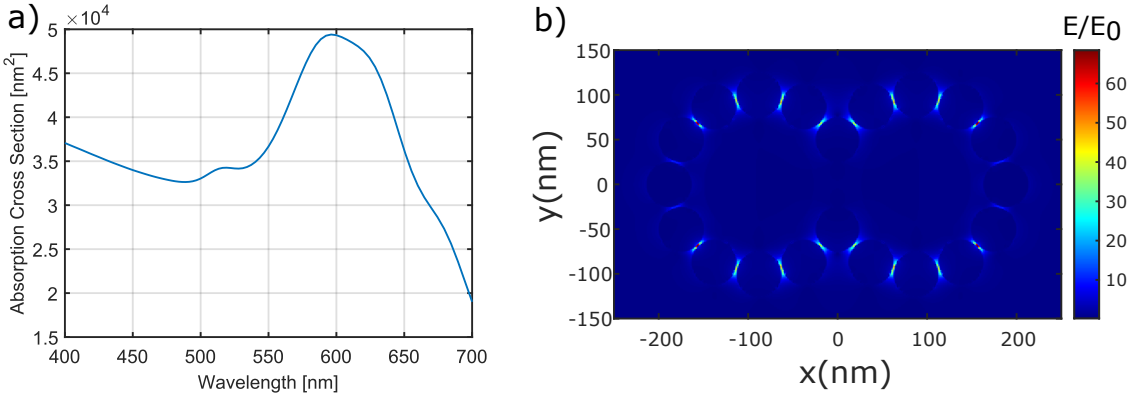

Figure 6.5: a) Simulated absorption cross-section of the dimer structure for excitation along the long axis. A minor peak is visible at 520 nm and a major peak at 607 nm. b) Simulated field enhancement. Eight major hotspots can be seen between the top and bottom spheres and their nearest neighbours. Eight minor hotspots can be found in the next neighbouring gaps, while the field enhancement is low on the outermost spheres. A maximum field enhancement of 69 is calculated compared to the incident light.

For simulations with illumination along the short axis, the absorption cross-section as well as the modes look quite different since the dimer structure is not rotationally symmetric. The absorption cross-section shows three distinct peaks: 513 nm, 573 nm and 680 nm (see figure 6.6).

In the simulation of the electric field enhancement, one can see different modes which correspond to these different peaks. A maximum of field enhancement was found at 581 nm. This mode can be seen in 6.7a). For this mode, four major hotspots arise at the outermost gold spheres and their nearest neighbours and smaller hotspots in the neighbouring gaps. Additionally, hotspots of high intensity arise between the innermost spheres (with x=0) and their respective neighbours. Again, smaller hotspots arise in the gaps next to these gaps. The highest field

enhancements could be found in the outermost gaps, with an enhancement factor of 44.1.

A different mode with another local maximum in field enhancement could be found at 689 nm. The major hotspots this time are between the outermost spheres and the adjacent spheres, with minor hotspots between these spheres and their respective next neighbours. Only very little field enhancement can be found around the innermost spheres (see figure 6.7b)).
To get a further understanding of the absorption cross-sections, the absorption cross-section of a single silica sphere as well as that of a single gold sphere on glass and ITO were simulated. The cross-sections can be found in figure 6.8.
The single silica sphere has a smaller cross-section than the (larger) monomer and dimer structures, as well as the (smaller) single gold sphere. This is expected due to the small imaginary part of the refractive index of the dielectric material compared to that of gold, which is directly responsible for absorption of light in all material [163, 91, 164, 165]. Despite its smaller absorption cross-section, the contribution of the silica core to the monomer and dimer cross-sections can be seen in the increasing areas when looking at wavelength smaller than 480 nm.
The absorption cross-section of a single gold sphere on glass and ITO has a peak at 500 nm as well as at 684 nm. This peak can probably be seen in the absorption cross-section of the monomer as well as of the dimer structures, however shifted red by around 15 nm. This shift could happen due to the contact with the silica core in the other configurations. Another hint, that this peak in the monomer and dimer spectra is due to the gold particle, can be seen in the electric field monitor. For the excitation along the short axis, no new mode can be seen for the peaks at 513 nm and 573 nm, which suggests that one of the peaks in the cross-section stems from the gold particles.

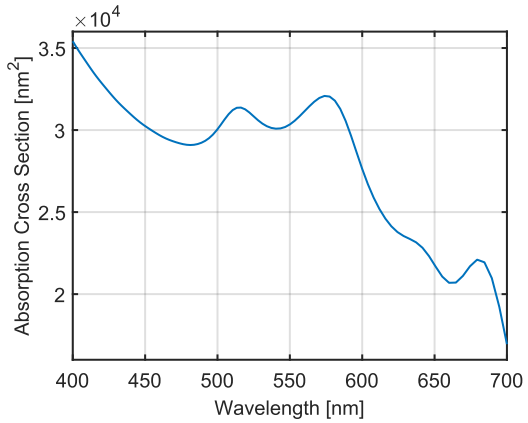

Figure 6.6: Simulated absorption cross-section of dimer structure illuminated with linearly polarised light along the short axis. Three distinct peaks can be seen at 513 nm, 573 nm and 680 nm.

Limitations and deviations of the simulation from the actual particles are of various kinds. For one, the chemically grown core and satellite spheres are never completely spherical, but rather have facets due to the gold atoms being arranged in a crystalline

structure. These additional 'peaks' or flat facets, can highly influence the gap size, the local near field and field enhancement in these gaps [166, 167, 168].

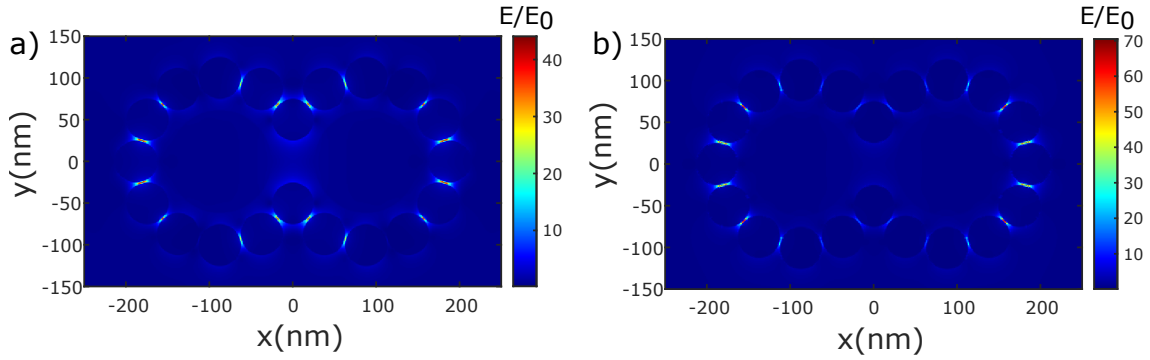

Figure 6.7: Field enhancement simulations for dimers with illumination along the short axis. a) Local maximum of field enhancement for 581 nm with major hotspots on the outermost and innermost spheres. b) Local maximum of field enhancement for 689 nm, with major hotspots on the outermost spheres, but only small field enhancement at the innermost spheres.

Furthermore, Benedikt Hettesheimer has measured and calculated the diameters of multiple cores and satellites and found for a sample size of 780 gold spheres an average diameter of 58,7 nm with a standard deviation of 4,8 nm. The size of the satellites can therefore fluctuate in one structure and between different structures. The same holds true for the core particles, for which he found for a sample of size 102 a diameter of 162,0 nm with a standard deviation of 5,6 nm.

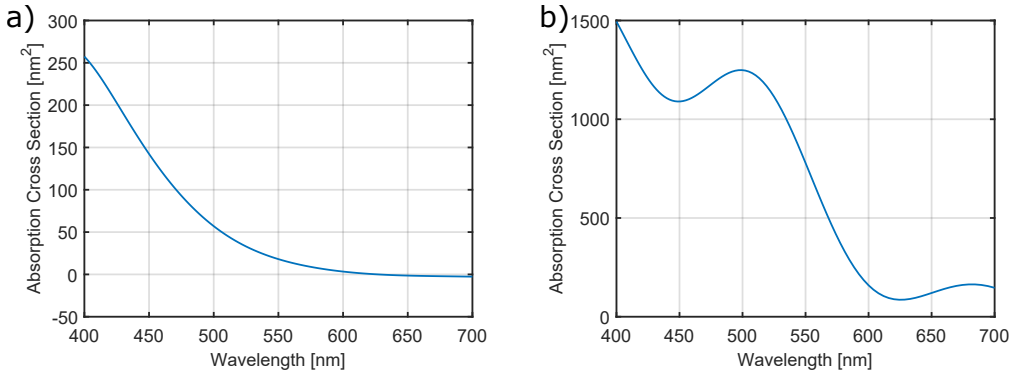

Figure 6.8: a) Absorption cross-section of a single silica core. The cross-section is small compared to that of the monomer and dimer structure, as well as the cross-section of a single gold sphere. The maximum lies somewhere in the ultraviolet regime. b) Absorption cross-section of a single gold sphere. A maximum can be seen at 500 nm with a second one at 684 nm.

Also, the arrangement of the spheres can have an influence on the gap size. Never all particles are distanced completely uniformly, which, as already mentioned, can have a huge impact on the resonance of plasmonic particles [169, 170]. Lastly, the

actual structures do not always have the same amount of satellites at all. While most monomer structures have 12 satellites, often extra satellite particles are stacked on one another, or sometimes satellite particles are missing, leaving either a big gap, widening the individual gaps on average, or mostly a mixture of both. All of these limitations and deviations could not be taken into account in the simulations, instead an idealised scenario was simulated based on the data, which was obtained from SEM images.

6.2 Optical Characterisation

Optical measurements were done in the DF setup described in chapter 3.1. First, a series of spectra were taken of different samples with unpolarised light. The spectra in figure 6.9 are of the exact same structures, that can be seen in figure 6.2, which were plasma cleaned. For the monomer structure (blue) a major peak can be seen at 805 nm and a minor one at 588 nm, which is a lot higher than expected from the simulations, however spectra differed greatly from particle to particle. Although, the general shape with a minor peak followed by a major peak fits well with the simulations.
The dimer structure (orange) shows a major peak at 796 nm and two smaller peaks at 558 nm and 627 nm, which overlap and nearly form a plateau. The shape of the major peak resembles that of the simulations for the dimer structure illuminated along the short axis, although again the location is not at the expected location. Moreover, for unpolarised light, a spectrum containing all modes would theoretically be expected.

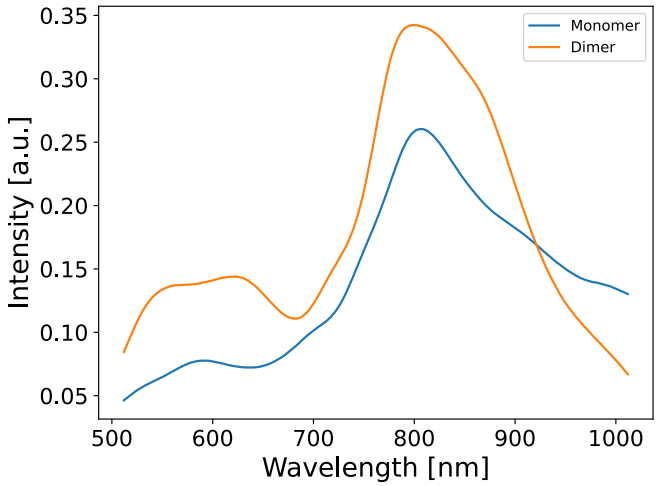

Figure 6.9: Unpolarised spectra of the monomer (blue) and dimer (orange) structure, that can be seen in figure 6.2.

Not only measurements with unpolarised light were carried out, but also with polarised light. To do so, a linear polarisation filter was placed into the illumination beam path of the DF microscope. Spectra were taken in 10° steps from 0° to 180°. In the following, measurements carried out by Felix Nägele and also by Benedikt Hettesheimer are presented.
For most particles, including monomers, a difference in spectra could be observed dependent on the orientation of the linear polariser. In the following figure 6.10, two spectra can be seen of one structure illuminated with linearly polarised light, with polarisation planes perpendicular to each other.

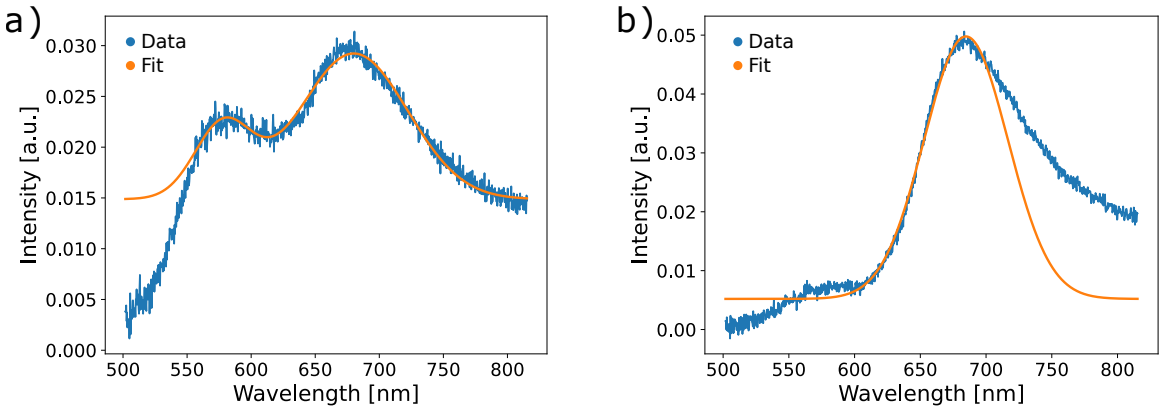

Figure 6.10: Spectra of structure with polarised light. a) At 0° and b) 90°. Since the orientation of the particle on the sample is unknown, the polarisation angles are only for orientation during measurements.

Two things can be seen while turning the polarisation filter between the measurements: the peak at 577 nm decreases in intensity until it vanishes completely when the polarisation plane approaches 90°, and the intensity of the peak at 684 nm increases in intensity. This indicates, that the particle is at least not rotationally symmetric and potentially a dimer structure.

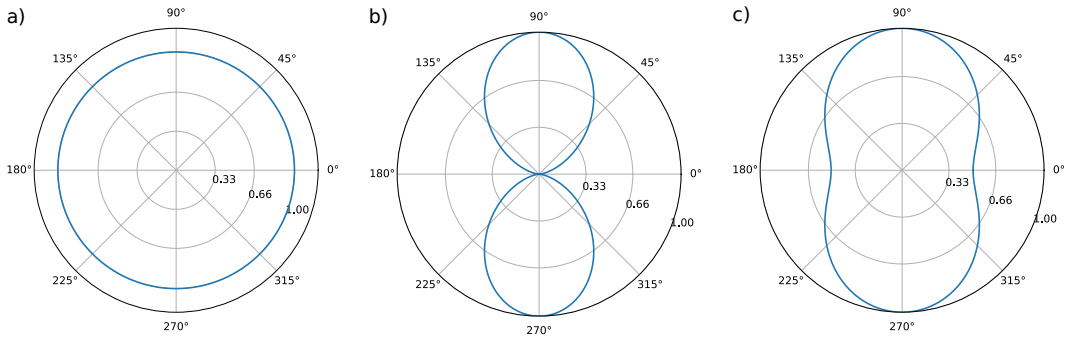

Figure 6.11: Calculated normalised emission intensity for different linearly polarised emission orientations and geometries. a) For a rotationally symmetric particle like a nanosphere the emission is expected to be independent of excitation orientation. b) For a perfect dipole it is expected to have the highest emission for excitation along the dipole axis (here 90°) and zero emission when exciting perpendicular to the dipole (here 0°). c) For a more complex structure consisting of a dipole and an isotropic offset a combined behaviour is expected with the highest emission along the dipole axis but a non-vanishing amount of emission when excited perpendicular to the dipole axis.

Figure 6.11 shows the emission response of various geometries to the excitation with linearly polarised light. The θ angle indicates the orientation of the linearly polarised light, while the radius indicates the normalised emission. For a rotationally symmetric particle like a nanosphere, the emission is independent of the excitation orienta-

tion. For a dipole, the highest emission is expected for excitation along the dipole axis and zero emission, when exciting perpendicular to that [85, 171]. For a hybrid structure like the dimer a superposition of both emission characteristics is expected with a preferential orientation of excitation, however a non-vanishing intensity for excitation perpendicular to that direction.
In figure 6.12, the intensity of the peak at 684 nm is plotted in polar coordinates. One can see its maximum intensity at 110° and its minimum for the perpendicular orientation of 20°. This suggests, that the particle has a long axis along the 110° axis.

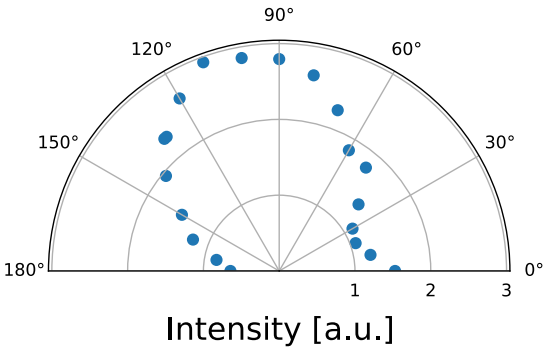

Figure 6.12: Intensity of the peak at 684 nm, depending on the orientation of the linearly polarised excitation light.

To be able to confirm the orientation and details of the measured structure in the SEM, further measurements were made on samples with a gold grid for orientation. The following measurements presented here were carried out by Benedikt Hettesheimer during the course of his bachelor thesis.
In figure 6.13, one can see the DF spectra of a dimer structure illuminated with unpolarised light (blue graph). Peaks are visible at 560 nm, 694 nm and 749 nm. For linearly polarised light, the spectrum changes depending on the orientation of the particle axis compared to the linear polarisation angle.

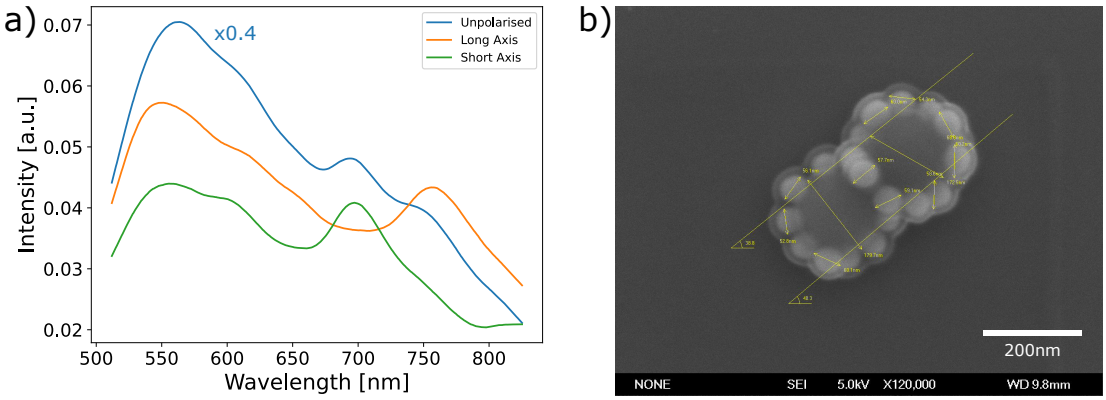

Figure 6.13: Measurements by Benedikt Hettesheimer. a) Scaled DF spectra of a dimer structure. Compared to the unpolarised light (blue) only one peak at higher wavelengths can be seen depending on the orientation of the polarised light. b) SEM image of the dimer structure.

For light polarised along the short axis of said particle (green graph), again a peak can be seen at 557 nm with a smaller peak at 600 nm, however in the red, there is only one peak at 700 nm. For a polarisation along the long axis, a peak is visible at 548 nm and again only one peak in the near-infrared at 760 nm.

The recorded DF spectra align quite well with the predictions made by simulations. The excitation along the short axis of a dimer structure shows three peaks, as expected in the calculated absorption cross-sections. Even the position of two relatively close peaks in the range between 500 nm and 600 nm fits very well with simulations, followed by a single peak at higher wavelengths. A general red shift of the spectrum compared to the simulation can be explained by the additional gold spheres around the centre of the structure as well as general arrangement deviations from the idealised model, which includes exact spacings, particle size and orientation of the particles.
The DF spectrum of excitation along the long axis does align well with the predictions from the simulation. Instead of just one plasmonic mode that is predicted in the adsorption cross-section, two peaks can be found, however the second peak is outside the simulation range of 700 nm. Differences can again stem from deviations between the actual particle and the simulation. Also, an excitation which does not perfectly align with the long axis has a small proportion of the field projected into the direction of the small axis, which could excite additional modes again.
Furthermore, as already explained above, a series of spectra is taken with changing polarisation planes again. The intensity of the peak at 760 nm is tracked with regard to the polarisation angle (see figure 6.14).

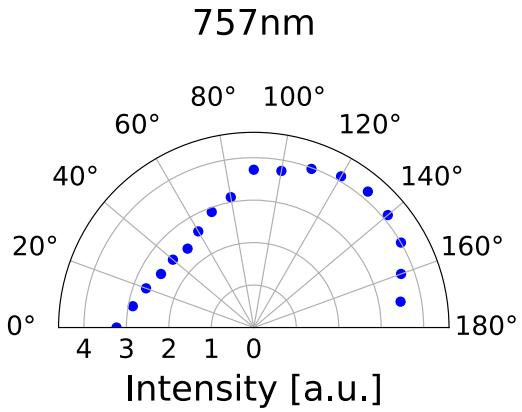

Figure 6.14: Measurement by Benedikt Hettesheimer. Intensity of the peak at 760 nm, depending on the orientation of the linearly polarised excitation light.

The maximum of emission for this peak can be seen at 130°. A major axis of the dimer structure would therefore be expected along that axis. SEM images taken of that exact structure with the same orientation of the sample in the SEM as well as the optical setup do align well. One can see in figure 6.13b), that the orientation of the dimer structure is rotated by 40° from the x-axis. This would correspond to a maximum for the 140° axis.

However, looking at further measurements of dimer structures, it becomes apparent that this small discrepancy is not exclusive for the dimer structure that can be seen in figure 6.13b), but rather appears on nearly all dimer structures. A further example structure is depicted in figure 6.15 (named P280), where the structure's long axis is aligned with the horizontal axis in 6.15b). The red line indicates a rotation by –15° away from the long dimer axis, the green line a rotation by 15°, and the blue line is perpendicular to the long dimer axis.

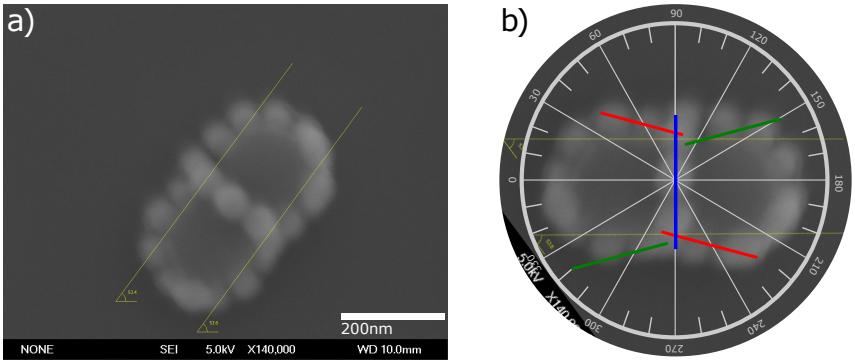

Figure 6.15: Measurement by Benedikt Hettesheimer. a) SEM image of dimer structure P280 as it is oriented on the sample. b) Rotated image, so that the long dimer axis is parallel to the horizontal axis. The red line is rotated by –15° towards the dimer axis, the green one by 15°. The blue line is perpendicular to the long dimer axis.

In figure 6.16 one can see spectra with excitation along the long axis and along the short axis, as well as the intensities of the peaks at 560 nm, 710 nm, and 880 nm. The angles are rescaled in a way, that the orientation aligns with the rotated image in figure 6.15b). One can see, that the maximum of the peak at 710 nm is at an angle of around 15° compared to the long dimer axis (which is at 0°).
Looking again at figure 6.15 one can see, that the angle aligns well with the longest straight alignments of gold nanospheres around the centre of the dimer structure. It is speculated, that these chains of spheres act as dipoles and thus explain the offset between structure axis and axis of highest excitation. These chains also explain the maximum of the peak at 880 nm, which would then correspond to the chain indicated by the blue line.
It should be noted, that due to the curvature of the cores, such arrangements are expected near the centre of the dimer structure and only for the case of additional satellites on the outer sides of the dimer structures.

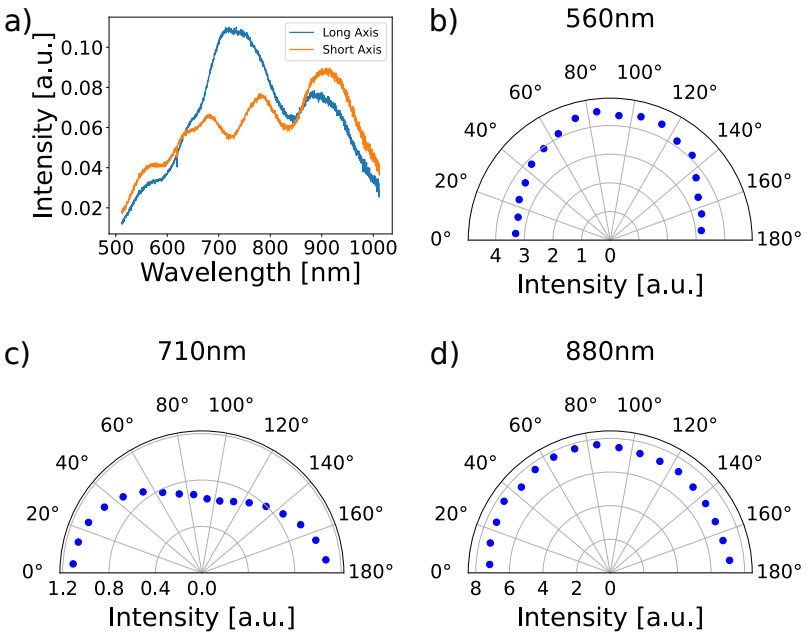

Figure 6.16: a) Spectra for excitation along the long axis and short axis. b) Intensities of the peaks for different polarisation angle of structure P280. Peak at 560 nm, c) at 710 nm and d) at 880 nm. Spectra are of the structure depicted in figure 6.15a) and are rescaled, to fit the orientation of the particle, as depicted in figure 6.15b).

6.3 (Surface Enhanced) Raman Spectroscopy

Surfaced Enhanced Raman Spectra (SERS) were taken of core-satellite structures to investigate their ability of local field enhancement and therefore enhancement of Raman scattering. For a first test, a sample was again cleaned in an oxygen plasma (as described above for the cleaning step), to clean the sample again but also to activate the surface for better adhesion of Raman-active molecules. Afterwards, the sample was submerged for 24 h in a 1 mmol/l solution of 4-mercaptobenzoic acid (4-MBA) (see the structural formula in figure 6.18) and ethanol. During that time, the thiol group of 4-MBA should bind to the gold surface and form a self-assembled monolayer. The sample was rinsed with ethanol after 24 h to remove excessive 4-MBA that did not bind to the gold surface. The laser power of the 633 nm laser was tuned to the maximum of 2,5 mW. Unfortunately, no Raman scattering could be measured with this preparation method on over 20 particles.

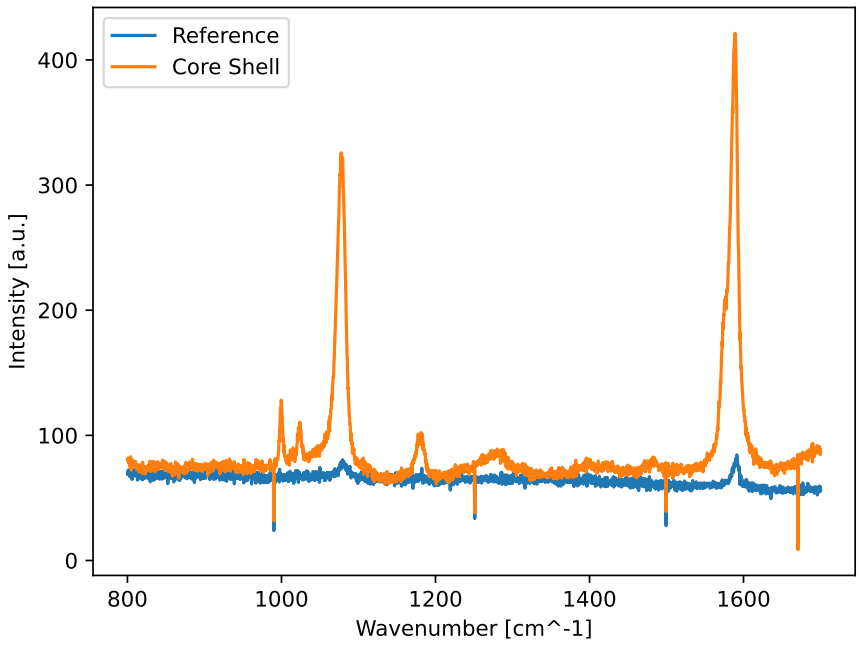

Figure 6.17: Raman spectrum of 4-MBA. The laser power was reduced to 1,3 mW. The reference (blue) was taken on the gold grid, integrated over 30 s and averaged over three cycles. The particle spectrum (orange) was integrated over 10 s and again averaged over three cycles.

In a second attempt, a 10 mM/l 4-MBA solution was spin coated on the sample at 500 rpm until the sample was dry. However, with this method big flakes of 4-MBA formed on the surface, mostly concentrated on the gold grid and core-satellite structures. These big flakes made it impossible to access the delicate and small core-satellite structures. Therefore, the sample was again cleaned with ethanol, to get rid of the big flakes.

Samples prepared this way did not show visible impurities or 4-MBA flakes in the DF microscope, however, a low intensity Raman scattering signal on the gold surface and an increased signal in around 3 of 30 nanostructures could be measured. This indicates a thin layer of 4-MBA bound to the surface of gold structures. A reference and a structure signal can be seen in figure 6.17.

The laser intensity for this measurement was reduced to 1,3 mW. The reference spectrum was taken on a random spot on the gold grid and was integrated for 30 s and averaged over three cycles. The signal is low compared to the background offset, but also compared to the noise level. Small peaks at 1077 cm^{-1} and 1589 cm^{-1} can be seen. The peaks will be later appointed to different vibrational modes of the 4-MBA molecule.
The spectrum on the core-satellite structure (the SERS measurement) was taken with an integration time of only 10 s and was also averaged over three cycles. The spectrum shows a way higher intensity compared to the reference spectrum, as well as compared to the background and noise of the measurement. From lowest to highest wave number, distinct peaks can be seen at 999 cm^{-1}, 1023 cm^{-1}, 1078 cm^{-1}, 1180 cm^{-1}, 1276 cm^{-1}, 1482 cm^{-1}, 1588 cm^{-1}.

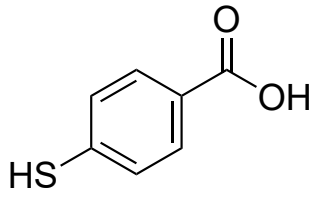

4-Mercaptobenzoic acid

Figure 6.18: Structural formula of 4-MBA

Raman Shift [cm^{-1}]	Mode
999	surface-π conj.
1023	ring deformation
1078	ν_{ring} breathing
1180	surface-π conj.
1276	ν_s(C-O)
1482	β (CH_2/CH_3)
1588	ν_{ring} breathing

Table 6.1: Table of peaks from the SERS measurement with their corresponding vibrational modes. The peaks were assigned to the different modes with the help of [14, 172, 173, 174, 175]

These peaks can be assigned to various vibrational modes of the 4-MBA. The naming convention follows the Wilson notation, where stretching modes ν, bending modes β and rocking modes γ are denoted with their respective Greek letter. Furthermore, symmetric (s) and asymmetric (as) modes are denoted via subscript on the Greek letters, to provide further information about the vibration.
The different peaks of the SERS and their corresponding vibrational modes are listed in table 6.1.
Special attention should be given to the fact, that 4-MBA has a benzene ring, whose

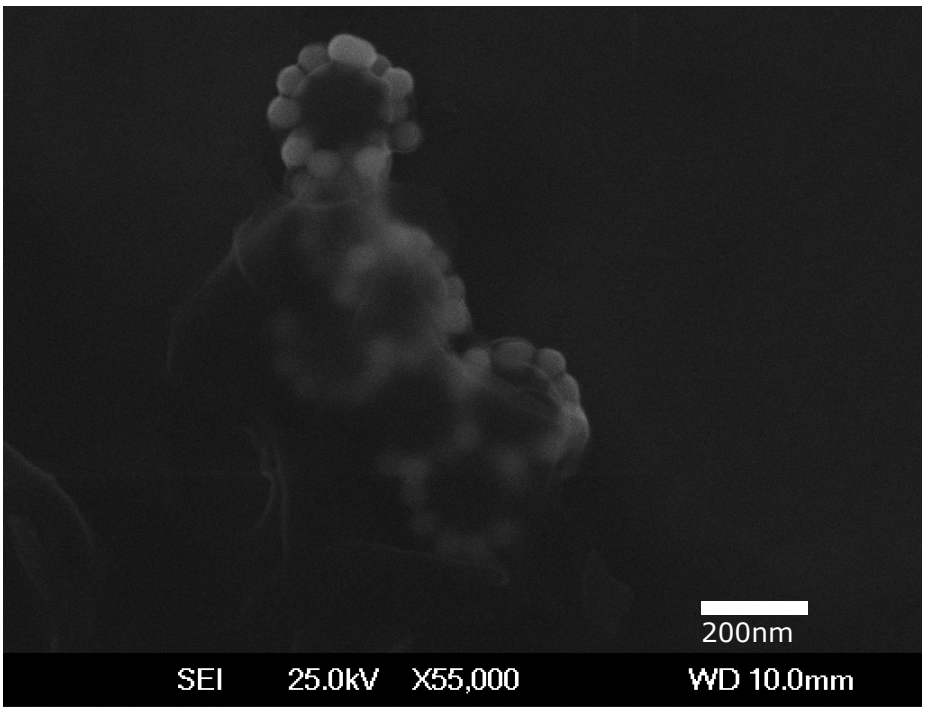

Figure 6.19: SEM image of the exact structure of which the SERS measurements were taken. It should be noted, that the whole complex of cores and satellites is larger than the diameter of the laser spot.

π-electron system can conjugate with the gold surface. According to [173], this indicates that 4-MBA is bonded to the gold surface under an angle compared to the normal direction of the surface. Furthermore, this configuration is also energetically preferable, since now the π-electrons of the neighbouring molecules can reach maximum van-der-Waals interaction [173]. An SEM image of the structure with the highest SERS enhancement (shown in figure 6.17) could be taken due to the marker system on the sample (figure 6.19).
The SERS structure consists of several cores with multiple satellites and has a longest extension of around 1000 nm. It also appears as if parts of the structures are covered with some substance. It is estimated, that this substance is a larger accumulation of 4-MBA. This poses the question, whether the SERS is actually a Raman spectrum of the 4-MBA which adheres to the surface or rather if it is a 'bulk' Raman spectrum of the 4-MBA layer. A good indication, that the SERS spectrum is actually (mostly) of the surface molecules is againgiven by a look at the surface-conjugated π-electrons. These modes with peaks at 999 cm^{-1} and 1180 cm^{-1} are only visible if the molecule is bound to a gold surface and furthermore is angled to the normal of that gold surface. This is the case in SERS measurements, since the peaks are clear and prominent in this measurement. To confirm with certainty that no 'bulk' Raman spectrum of a 4-MBA flake covering a gold structure was taken by accident, a Raman spectrum of actual pure 4-MBA powder was taken and compared to the SERS measurement. The laser power for the measurement on powder was increased again to 2,5 mW (compared to 1,3 mW for the SERS), the integration time and averages stayed the same. The 4-MBA powder Raman spectrum compared to that of the SERS can be seen in figure 6.20

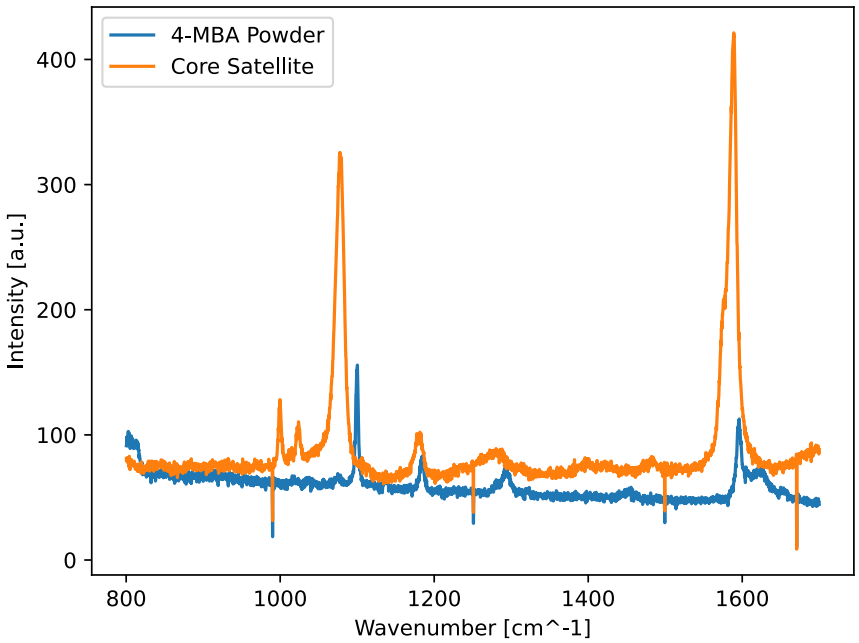

Figure 6.20: Comparison of the SERS spectrum (orange) with the Raman spectrum of pure 4-MBA powder on glass (blue). The laser power for the measurement on powder was 2,5 mW compared to 1,3 mW for the SERS measurement.

The overall intensity of the powder Raman spectrum is lower than that of the SERS measurement, despite a higher laser intensity and a much higher interaction volume of the laser. Also, the peaks at 999 cm^{-1} and 1023 cm^{-1} are completely gone, of which the 999 cm^{-1} peak indicates a surface conjugation of the π-electrons in the ring. This gives further proof of an actual SERS measurement of the samples.
With the help of the SEM image in figure 6.19 and the SERS spectrum with reference in figure 6.17, one can calculate the effective enhancement factor (see chapter 2.9). To do so, first the hotspot area or rather the surface of the satellites in the hotspot area has to be calculated/estimated. Looking at the simulations, the polar angle between the ray from the centre of the sphere to the intensity maximum and the ray from the centre of the sphere to the edge of the hotspot is measured at $\alpha_o = 14°$. The area of that spherical cap can be calculated with [176]

$$A_{eff} = 2\pi r^2 (1 - \sin\alpha_0), \tag{6.1}$$

which corresponds to a surface area of the satellite in the hotspot of 116 nm^2 with a satellite diameter of 50 nm. For simplicity reasons and to find a lower limit for the enhancement factor, it is assumed that the laser was unpolarised, and a hotspot occurred between every pair of neighbouring satellites. With the help of figure 6.19, one can see 44 satellites and calculate with as many hotspots, despite the laser focus diameter being smaller than that. Since it is not possible to know where exactly the laser was focused on the structure, it is assumed that the whole surface was illuminated.

With that assumption we receive an upper limit for the hotspot area of

$$A_{eff} \cdot n = 116\,nm^2 \cdot 44 = 5104\,nm^2. \tag{6.2}$$

For the calculation of the effective enhancement factor EF* with equation 2.75, the area of the laser focus A_{laser} is required, which is given by equations 2.76 and 2.77. The NA of the used objective is NA = 0,5. This leads to a value of

$$A_{laser} = 466\,921\,nm^2. \tag{6.3}$$

Additionally, the normal enhancement factor EF is needed for the calculation of EF*. To obtain that, the peaks at $1078\,cm^{-1}$ of the measurement on the structures and that of the reference in figure 6.17 were fitted with a Gauss function, and their intensities relative to the background were divided by each other. An $EF_{rel} = 69$ was obtained, meaning that the signal of the core-satellite structures was more intense by this factor. Finally, it is possible to calculate a lower bound for the effective enhancement factor EF*:

$$EF^* = EF_{rel} \cdot \frac{A_{laser}}{A_{eff} \cdot n} = 69 \cdot \frac{466\,921\,nm^2}{5104\,nm^2} = 6312. \tag{6.4}$$

It should be noted, that this estimation is only a lower bound of one measurement, however, it already shows the potential of these structures for SERS measurements as already has been done in similar structures [46, 47, 48]. As a next step, it would be interesting to fabricate these core-satellite structures with a Raman active molecule as linker instead of PEG to achieve an even better and more selective placement of the Raman active material in the hotspots.
Also, different materials than 4-MBA can be tested as SERS molecule, for example polystyrene.

6.4 Refractive Index Sensor

As with the Yagi-Uda-antennas, refractive index dependent measurements were carried out with the core-satellite particles. A special feature of the structures is, as aforementioned, the encapsulation of the structures in a PEG layer due to the fabrication process. In order to even get into the vicinity of the structures, the several nanometer thick polymer layer has to be removed. This is done in a RIE process (see chapter 4.4).
Following that, spectra of different structures were recorded with the sample as is. Afterwards, a drop of water was cast on top of the sample, and new spectra of the exact same structures were taken. Exemplary spectra can be seen in figure 6.21. A clear shift of the resonance frequency can be seen between air (blue) and water (orange). While the DF spectrum in air has a resonance frequency of 804 nm, the spectrum of the sample covered with water has a peak at 842 nm. With a refractive index of water of n = 1,33 a sensitivity of the structures of 115 nm/RIU can be calculated.
For five measurements on different particles the average frequency shift came out to be even higher with an average shift of 43,4 nm and a standard deviation of 14,1 nm. The relatively high standard deviation shows again the influence of the individual gap sizes and arrangements of the satellites around the core on the plasmonic properties of he structures. The sensitivity of the average shift would increase to 132 nm/RIU. This can be compared to the sensitivity of single gold spheres of a diameter of 54 nm surrounded by a homogeneous medium. According to [165], the resonance peak here is 508 nm for air as medium and 532 nm in water. This would lead to a sensitivity of 85 nm/RIU. That makes the core satellite structures already a more sensitive refractive index sensor than a simple gold colloid solution.

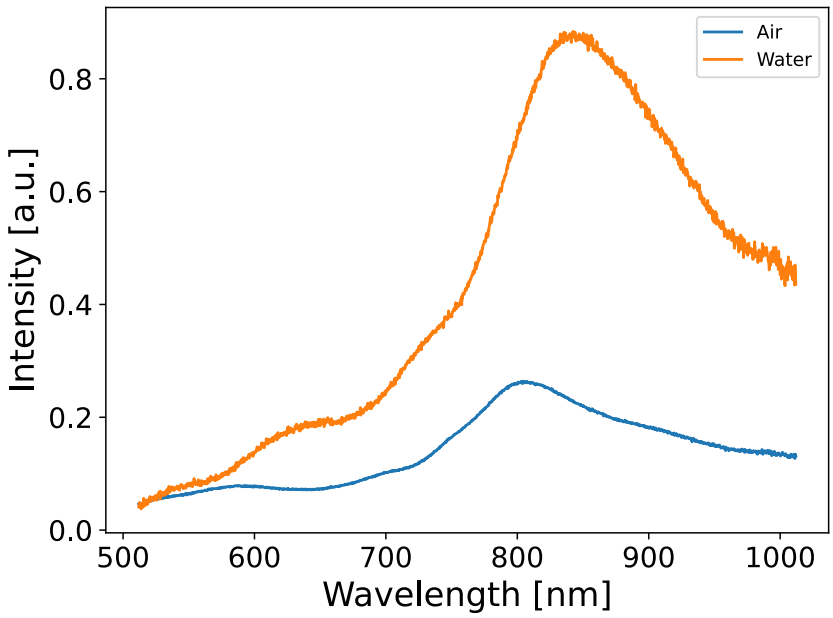

Figure 6.21: DF spectra of the monomer structure in figure 6.2a). While the spectrum in air (blue) has a peak at 804 nm, the spectrum of the structure covered with water (orange) has a peak at 842 nm

Additional to the measurements on monomer structures, the experiment was repeated on a dimer structure. The SEM image and DF spectra of the dimer structure in air (blue) and water (orange) can be seen in figure 6.22. The major peak of the dimer structure in air is at 794 nm, while the major peak in water is at 856 nm. Again, with the refractive index of water of n=1,33 one can calculate a sensitivity of 188 nm/RIU. This is an even higher sensitivity than for the monomer structure and suggests, that the more complex structures respond stronger to environmental changes than simpler structures.

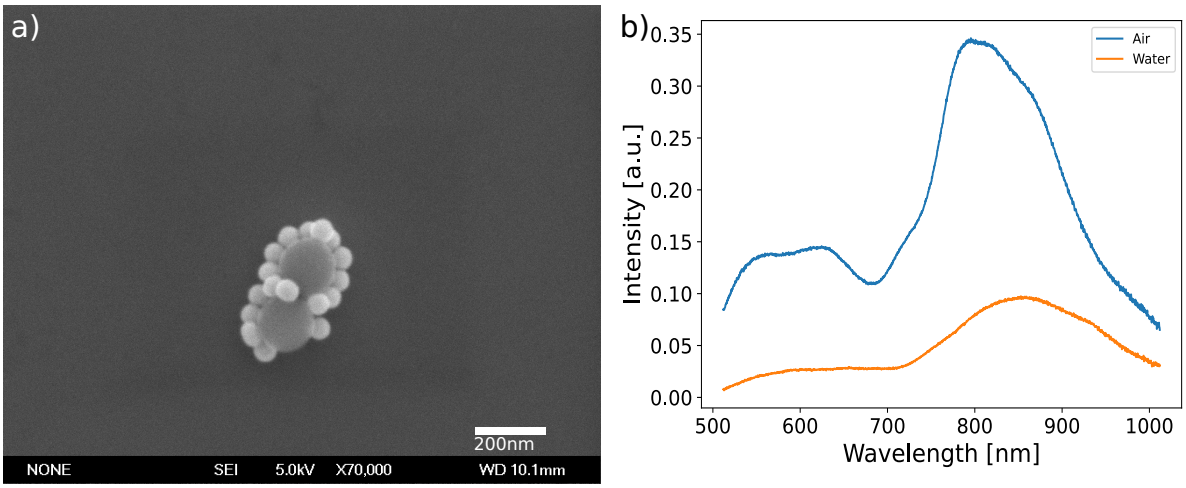

Figure 6.22: a) SEM image of dimer structure. b) DF spectra of the structure in air (blue) with a major peak at 794 nm and in water (orange) with a major peak at 856 nm.

Considering that surface functionalisation of these structures was shown two times already, once in the fabrication with PEG molecules and another time during the Raman measurements with 4-MBA, the here-presented core-satellite structures could function well as an optical biosensor. Similar to the work of [177, 153, 11], the structures could be again incorporated in a flow cell, and a linker structure can be bound to the surface. The analyte can couple to the surface and induce a refractive index change, which thereby shifts the plasmon resonance. Considering that various samples were submerged in water and ethanol and rinsed several times, the structures appear to be durable enough to also function in a flow cell setup with a moderate flow rate.

7 Summary and Outlook

Over the course of this work, different plasmonic nanostructures were fabricated, and their properties and behaviours were studied. The first big part of this work revolved around optical Yagi-Uda-antennas, their fabrication and optical characterisation. Before the first antennas were fabricated, FDTD simulations were carried out to find optimal production parameters, as well as indications of what to expect for changing environments or configurations of the antennas.
Different fabrication techniques were adapted, among them the most used technique of electron beam lithography, as well as milling out antennas via a focused helium ion beam. Furthermore, it was tried to produce a mask by etching holes in a metal layer for selective quantum dot coupling with the help of the focused helium ion beam. Lastly, half-covered antennas were fabricated, by covering all antenna elements with a layer of high refractive index SiO_2 and milling away this layer on one half of each antenna element.
While the quantum dot coupling did not work well via metal mask, a double electron beam lithography process with better alignment techniques on a new SEM could provide the mask together with a soft mask removal technique, that does not destroy the antennas in the process, to successfully couple quantum dots to Yagi-Uda-antennas.

Of the Yagi-Uda-antennas, DF spectra were taken in air as they are, or incorporated into a flow cell with different mixtures of water and glycerol. A small shift in resonance frequency could be seen between air and water, which resulted in a sensitivity of 45,5 nm/RIU, however, due to the overlap of resonance spectra of the single antenna elements, the overall resonance curve of the antennas has a large width.
Additional to the DF spectra, BFP images were taken of the antennas incorporated into a flow cell, where a manipulation of the polar angle of emission was expected due to the different refractive indices of the liquids in the cell. However, the forbidden zone of emission could not be mapped sufficiently with the provided microscope to observe a manipulation of the polar angle of emission. Furthermore, BFP measurements were carried out on half-covered antennas. Here, a manipulation of the azimuthal angle of emission was expected. Two different half-covered antennas were compared to a fully covered antenna. A change of the azimuthal angle of emission could be seen for all antennas, which was significantly higher for the half-covered antennas. After deduction of the offset given by the fully covered antenna, a change in emission angle from air to water of 10° and 16° could be seen for the half-covered antennas, which also occurred into the expected direction.
For future measurements, different masking materials could be tried as well as different fabrication methods, for example again with an aligned double electron beam lithography step. Moreover, the antennas can be incorporated into flow cells, which gives rise to higher versatility in the change of liquids and could potentially reduce or eliminate the offset problem. A further idea would be to biologically functionalise the uncovered gold surface and change the local refractive index by accumulating an analyte on one half of the antenna.

Final measurements with Yagi-Uda-antenna structures were carried out in the parabolic mirror setup by Felix Schneider. A SHG signal could be produced, which exceeded that of the silicon substrate, however, the PL signal dominated the spectrum. Measurements with rotated linear polarisation showed greatest SHG for an orientation of the light parallel to the antenna elements. Furthermore, in the BFP some directed emission could be seen, although low compared to the reference signal.
For further measurements different materials can be tested, for example aluminium, which produces a lower PL signal compared to gold, or different substrates, which influences the emission distribution in the two half spaces.

In the second part of this work, core-satellite structures were studied. They were fabricated in a wet chemical, bottom-up synthesis by Yingying Cai at the University of Göttingen. The structures consist of one or two silica cores, which are surrounded by gold nanospheres. Again, FDTD simulations were carried out to determine the absorption cross-section of the monomer and dimer configuration for different polarisations. Additionally, the near-field was monitored and the different plasmon modes determined.
As a first experiment, DF spectra of the structures were taken with unpolarised light as well as with linearly polarised light of different orientations. With the help of a marker system, the exact structures and their orientation could be determined in the SEM. It showed that the different axes of maximum excitation correlate not necessarily with the structure axis, but rather with long straight arrangements of nanospheres, which acted like dipoles.
As a second experiment, the structures were tested for their SERS abilities. To do so, the samples were cleaned in oxygen plasma and exposed to a nanoscopic layer of 4-MBA. In some structures a SERS effect could be observed, with an increase in signal due to the high local fields between the gold nanospheres compared to a flat gold structure. In future experiments, the polymer used for the fabrication of the nanostructures could be exchanged for a Raman active one like polystyrene. This way, it would be incorporated even better into the electric field hotspots for higher enhancements.
Lastly, the shift in plasmon frequency of the monomer and dimer structures was observed in dependency on the surrounding refractive index. DF spectra were taken of oxygen-cleaned structures in air or covered by water. A sensitivity of 115 nm/RIU could be observed, which makes these structures viable for sensing applications. Due to the versatility of the core-satellite system, a surface functionalisation of the gold nanospheres is possible, but also the linking polymer can have interesting properties like thermal expansion [56] or biological activity.

Appendix

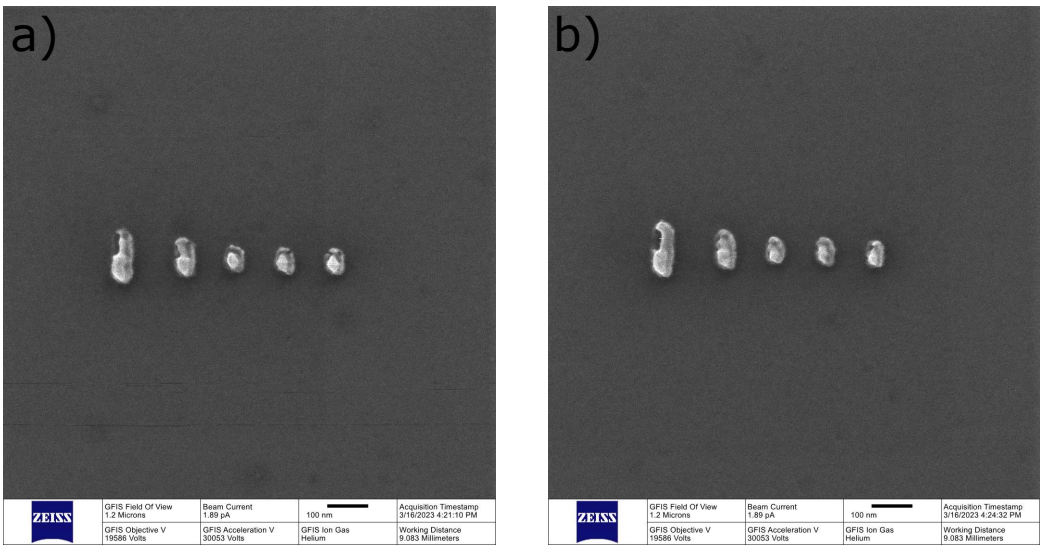

Figure 7.1: HIM images of half-covered antennas. The bottom half of each antenna element is covered in SiO_2. a) HIM image of antenna 1_6. b) HIM image of antenna 1_7.

Sample	Water	Air	Sample	Water	Air	Sample	Water	Air
1_6	10,64	-0,06	1_7	19,26	0,24	Covered	5,22	5,25
	24,16	1,34		17,24	2,88		18,65	1,98
	11,84	-1,4		27,36	4,98		4,08	1,94
	19,38	3,65		24,93	2,41		4,14	5,91
	9,92	3,64		-4,86	1,87		3,38	2
Mean	15,19	1,43	Mean	16,79	2,48	Mean	7,09	3,42
Std dev	6,28	2,24	Std dev	12,78	1,728	Std dev	6,49	1,99
			Mean2	22,20				
			Std dev2	4,74				

Table 7.1: Table with azimuthal emission angles of the half-covered antennas 1_6 and 1_7 shown in figure 7.1 as well as the completely covered antenna. Mean2 and Std dev2 of antenna 1_7 is calculated by omitting the outlier of the fifth measurement.

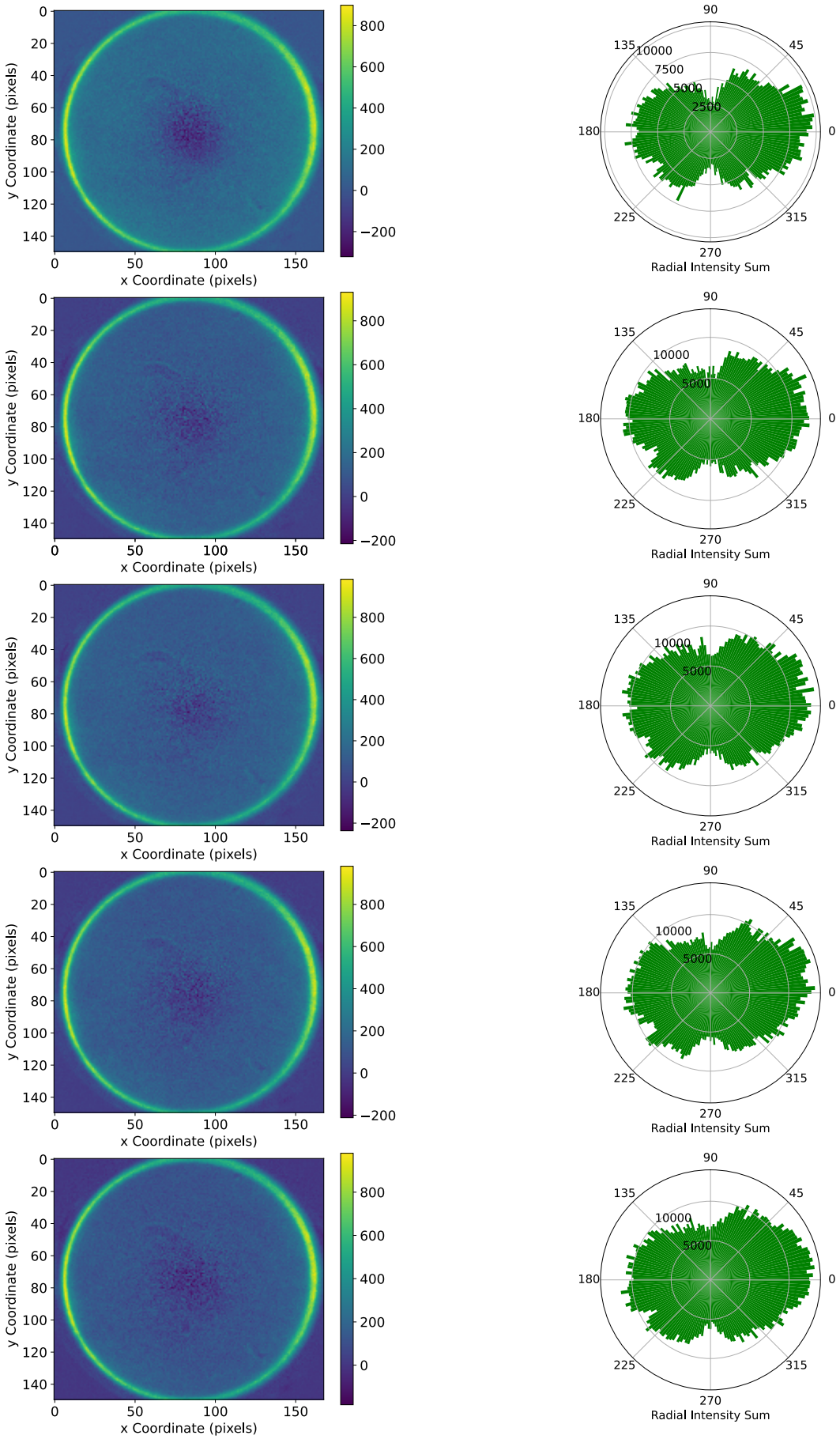

Figure 7.2: BFP images and emission patterns of antenna 1_6 covered in water.

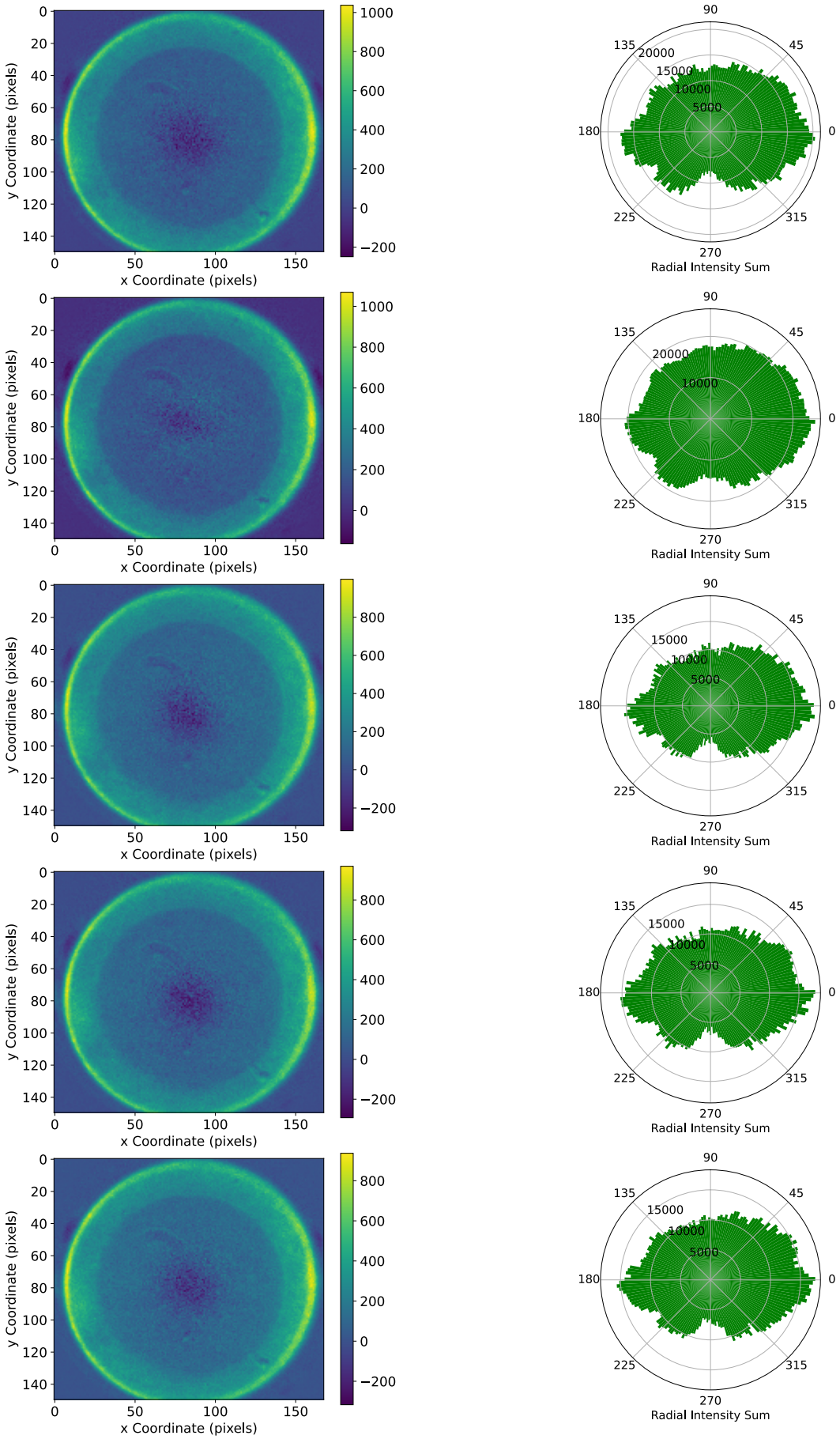

Figure 7.3: BFP images and emission patterns of antenna 1_6 in air.

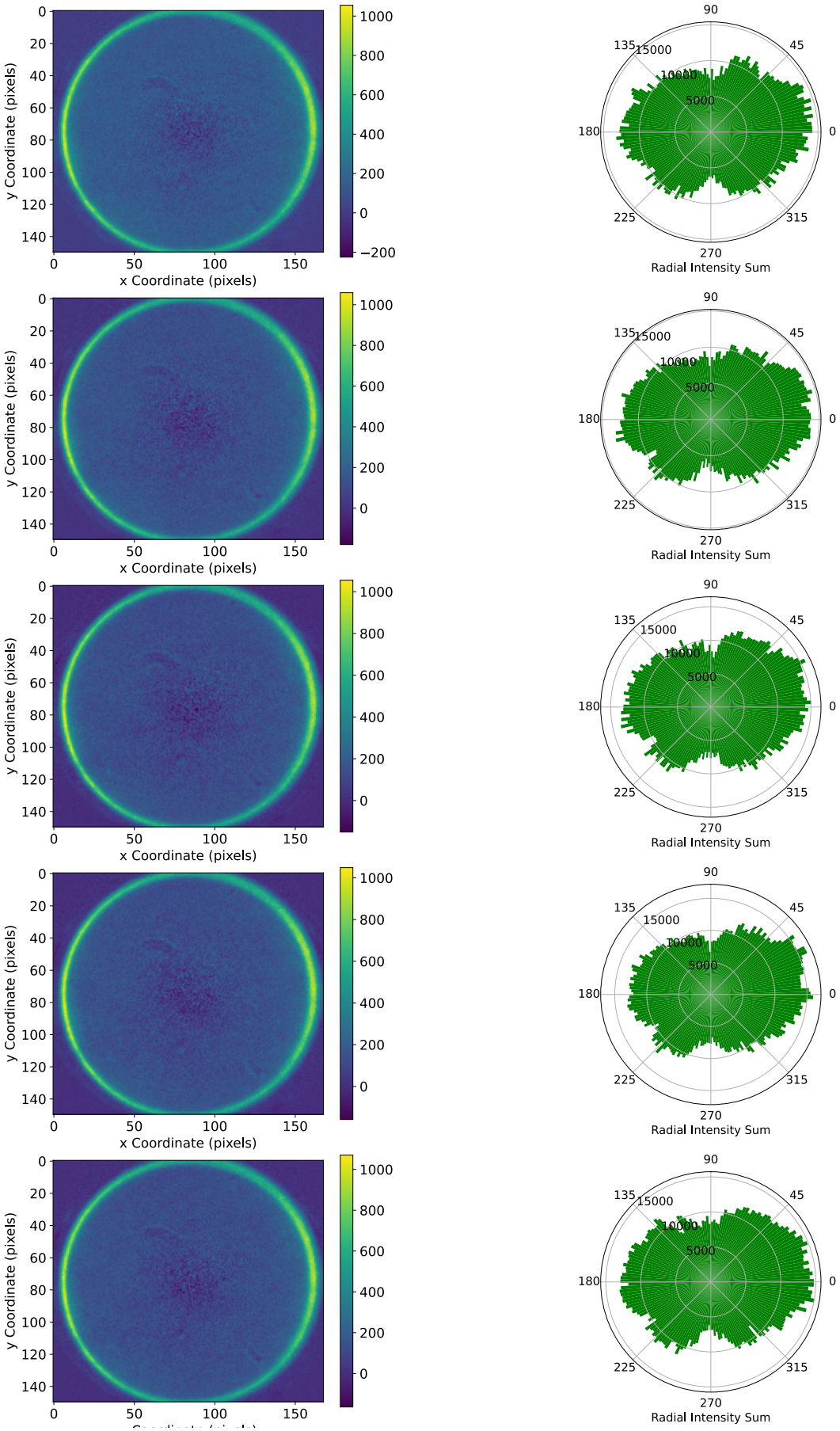

Figure 7.4: BFP images and emission patterns of antenna 1_7 covered in water.

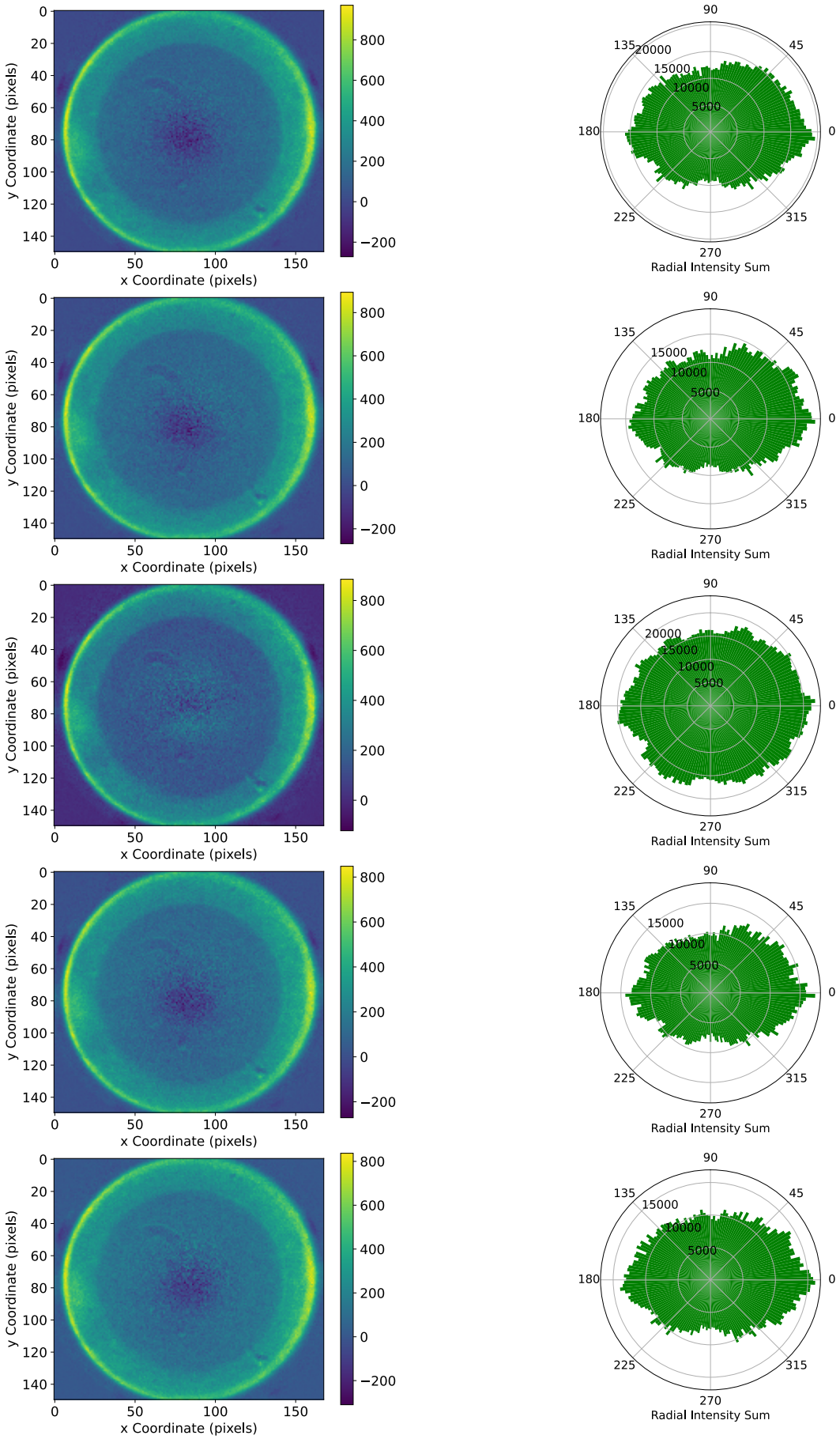

Figure 7.5: BFP images and emission patterns of antenna 1_6 in air.

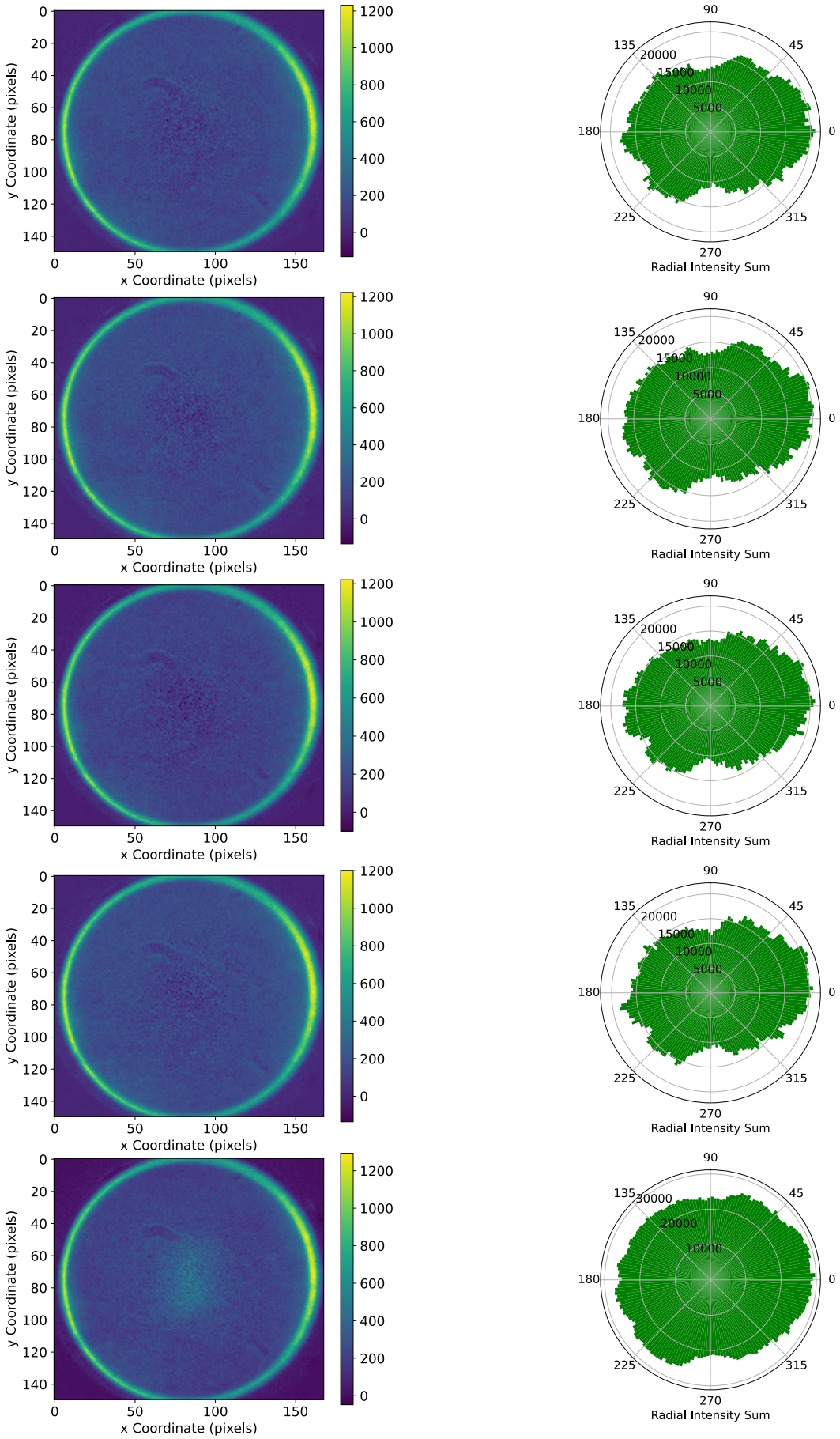

Figure 7.6: BFP images and emission patterns of completely covered antenna in water.

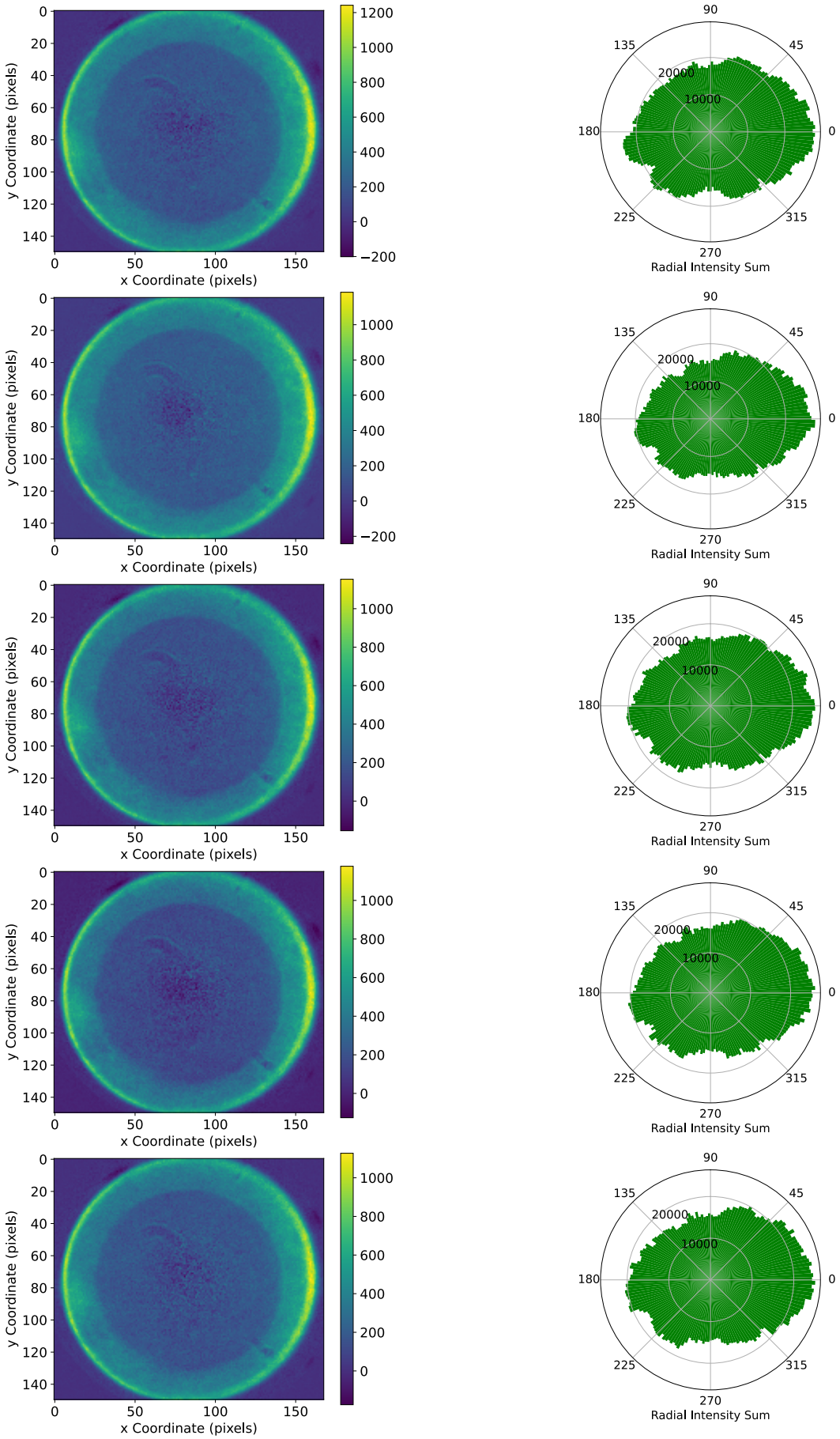

Figure 7.7: BFP images and emission patterns of completely covered antenna in air.

References

[1] H. Yagi and S. Uda. "Projector of the Sharpest Beam of Electric Waves". In: *Proceedings of the Imperial Academy* 2.2 (1926), pp. 49–52. DOI: 10.2183/pjab1912.2.49.

[2] H. Yagi. "Beam Transmission of Ultra Short Waves". In: *Proceedings of the IRE* 16.6 (1928), pp. 715–740. DOI: 10.1109/jrproc.1928.221464.

[3] X. Hong et al. "Synthesis, properties and applications of one- and two-dimensional gold nanostructures". In: *Nano Research* 8.1 (2014), pp. 40–55. DOI: 10.1007/s12274-014-0636-3.

[4] K. He et al. "Assemblies and composites of gold nanostructures for functional devices". In: *Aggregate* 3.4 (2021). DOI: 10.1002/agt2.57.

[5] Z. Guo et al. "Intrinsic Optical Properties and Emerging Applications of Gold Nanostructures". In: *Advanced Materials* 35.23 (2023). DOI: 10.1002/adma.202206700.

[6] X. Huang et al. "Cancer Cell Imaging and Photothermal Therapy in the Near-Infrared Region by Using Gold Nanorods". In: *Journal of the American Chemical Society* 128.6 (2006), pp. 2115–2120. DOI: 10.1021/ja057254a.

[7] K. Sztandera, M. Gorzkiewicz, and B. Klajnert-Maculewicz. "Gold Nanoparticles in Cancer Treatment". In: *Molecular Pharmaceutics* 16.1 (2018), pp. 1–23. DOI: 10.1021/acs.molpharmaceut.8b00810.

[8] Y. Zhang et al. "Colorimetric detection based on localised surface plasmon resonance of gold nanoparticles: Merits, inherent shortcomings and future prospects". In: *Talanta* 152 (2016), pp. 410–422. DOI: 10.1016/j.talanta.2016.02.015.

[9] N. Zohora et al. "Rapid colorimetric detection of mercury using biosynthesized gold nanoparticles". In: *Colloids and Surfaces A: Physicochemical and Engineering Aspects* 532 (2017), pp. 451–457. DOI: 10.1016/j.colsurfa.2017.04.036.

[10] A. Piriya et al. "Colorimetric sensors for rapid detection of various analytes". In: *Materials Science and Engineering: C* 78 (2017), pp. 1231–1245. DOI: 10.1016/j.msec.2017.05.018.

[11] A. Horrer et al. "Compact plasmonic optical biosensors based on nanostructured gradient index lenses integrated into microfluidic cells". In: *Nanoscale* 9.44 (2017), pp. 17378–17386. DOI: 10.1039/c7nr04097k.

[12] Z. Hua et al. "Recent advances in gold nanoparticles-based biosensors for food safety detection". In: *Biosensors and Bioelectronics* 179 (2021), p. 113076. DOI: 10.1016/j.bios.2021.113076.

[13] J. Reguera et al. "Anisotropic metal nanoparticles for surface enhanced Raman scattering". In: *Chemical Society Reviews* 46.13 (2017), pp. 3866–3885. DOI: 10.1039/c7cs00158d.

[14] P. C. Simo et al. “Hexagonal arrays of plasmonic gold nanopyramids on flexible substrates for surface-enhanced Raman scattering”. In: *Nanotechnology* 33.9 (2021), p. 095303. DOI: 10.1088/1361-6528/ac3579.

[15] K. L. Kelly et al. “The Optical Properties of Metal Nanoparticles: The Influence of Size, Shape, and Dielectric Environment”. In: *The Journal of Physical Chemistry B* 107.3 (2002), pp. 668–677. DOI: 10.1021/jp026731y.

[16] P. Nordlander et al. “Plasmon Hybridization in Nanoparticle Dimers”. In: *Nano Letters* 4.5 (2004), pp. 899–903. DOI: 10.1021/nl049681c.

[17] N. J. Halas et al. “Plasmons in Strongly Coupled Metallic Nanostructures”. In: *Chemical Reviews* 111.6 (2011), pp. 3913–3961. DOI: 10.1021/cr200061k.

[18] A. Movsesyan et al. “Hybridization and Dehybridization of Plasmonic Modes”. In: *The Journal of Physical Chemistry C* 125.1 (2020), pp. 724–731. DOI: 10.1021/acs.jpcc.0c08570.

[19] H. F. Hofmann, T. Kosako, and Y. Kadoya. “Design parameters for a nano-optical Yagi–Uda antenna”. In: *New Journal of Physics* 9.7 (2007), pp. 217–217. DOI: 10.1088/1367-2630/9/7/217.

[20] J. Li, A. Salandrino, and N. Engheta. “Shaping light beams in the nanometer scale: A Yagi-Uda nanoantenna in the optical domain”. In: *Physical Review B* 76.24 (2007), p. 245403. DOI: 10.1103/physrevb.76.245403.

[21] T. H. Taminiau, F. D. Stefani, and N. F. van Hulst. “Enhanced directional excitation and emission of single emitters by a nano-optical Yagi-Uda antenna”. In: *Optics Express* 16.14 (2008), p. 10858. DOI: 10.1364/oe.16.010858.

[22] A. E. Krasnok et al. “Huygens optical elements and Yagi—Uda nanoantennas based on dielectric nanoparticles”. In: *JETP Letters* 94.8 (2011), pp. 593–598. DOI: 10.1134/s0021364011200070.

[23] L. Ma et al. “Yagi–Uda optical antenna array collimated laser based on surface plasmons”. In: *Optics Communications* 368 (2016), pp. 197–201. DOI: 10.1016/j.optcom.2016.01.090.

[24] I. S. Maksymov, A. E. Miroshnichenko, and Y. S. Kivshar. “Actively tunable bistable optical Yagi-Uda nanoantenna”. In: *Optics Express* 20.8 (2012), p. 8929. DOI: 10.1364/oe.20.008929.

[25] J. Li, A. Salandrino, and N. Engheta. “Optical spectrometer at the nanoscale using optical Yagi-Uda nanoantennas”. In: *Physical Review B* 79.19 (2009), p. 195104. DOI: 10.1103/physrevb.79.195104.

[26] X. Y. Z. Xiong et al. “Compact Nonlinear Yagi-Uda Nanoantennas”. In: *Scientific Reports* 6.1 (2016). DOI: 10.1038/srep18872.

[27] W. T. Sethi et al. “Yagi-Uda nantenna for 1550 nanometers optical communication systems”. In: *Microwave and Optical Technology Letters* 60.9 (2018), pp. 2236–2242. DOI: 10.1002/mop.31339.

[28] G. H. B. Damasceno, W. O. F. Carvalho, and J. R. Mejía-Salazar. “Design of Plasmonic Yagi–Uda Nanoantennas for Chip-Scale Optical Wireless Communications”. In: *Sensors* 22.19 (2022), p. 7336. DOI: 10.3390/s22197336.

[29] T. Kosako, Y. Kadoya, and H. F. Hofmann. "Directional control of light by a nano-optical Yagi–Uda antenna". In: *Nature Photonics* 4.5 (2010), pp. 312–315. DOI: 10.1038/nphoton.2010.34.

[30] A. G. Curto et al. "Unidirectional Emission of a Quantum Dot Coupled to a Nanoantenna". In: *Science* 329.5994 (2010), pp. 930–933. DOI: 10.1126/science.1191922.

[31] K.-M. See et al. "Photoluminescence-Driven Broadband Transmitting Directional Optical Nanoantennas". In: *Nano Letters* 18.9 (2018), pp. 6002–6008. DOI: 10.1021/acs.nanolett.8b02836.

[32] D. Dregely et al. "3D optical Yagi–Uda nanoantenna array". In: *Nature Communications* 2.1 (2011). DOI: 10.1038/ncomms1268.

[33] J. Dorfmüller et al. "Near-Field Dynamics of Optical Yagi-Uda Nanoantennas". In: *Nano Letters* 11.7 (2011), pp. 2819–2824. DOI: 10.1021/nl201184n.

[34] M. Ramezani et al. "Hybrid Semiconductor Nanowire–Metallic Yagi-Uda Antennas". In: *Nano Letters* 15.8 (2015), pp. 4889–4895. DOI: 10.1021/acs.nanolett.5b00565.

[35] R. Kullock et al. "Electrically-driven Yagi-Uda antennas for light". In: *Nature Communications* 11.1 (2020). DOI: 10.1038/s41467-019-14011-6.

[36] J. Ho et al. "Highly Directive Hybrid Metal–Dielectric Yagi-Uda Nanoantennas". In: *ACS Nano* 12.8 (2018), pp. 8616–8624. DOI: 10.1021/acsnano.8b04361.

[37] J. Kim et al. "Babinet-Inverted Optical Yagi–Uda Antenna for Unidirectional Radiation to Free Space". In: *Nano Letters* 14.6 (2014), pp. 3072–3078. DOI: 10.1021/nl500062f.

[38] M. Ha et al. "Multicomponent Plasmonic Nanoparticles: From Heterostructured Nanoparticles to Colloidal Composite Nanostructures". In: *Chemical Reviews* 119.24 (2019), pp. 12208–12278. DOI: 10.1021/acs.chemrev.9b00234.

[39] R. C. Mucic et al. "DNA-Directed Synthesis of Binary Nanoparticle Network Materials". In: *Journal of the American Chemical Society* 120.48 (1998), pp. 12674–12675. DOI: 10.1021/ja982721s.

[40] K. Ode et al. "Highly Sensitive Plasmonic Optical Sensors Based on Gold Core–Satellite Nanostructures Immobilized on Glass Substrates". In: *ACS Applied Materials Interfaces* 8.32 (2016), pp. 20522–20526. DOI: 10.1021/acsami.6b06313.

[41] H. Chen et al. "Self-Assembled Au@Fe Core/Satellite Magnetic Nanoparticles for Versatile Biomolecule Functionalization". In: *ACS Applied Materials &amp Interfaces* 11.27 (2019), pp. 23858–23869. DOI: 10.1021/acsami.9b05544.

[42] T. Zhang et al. "Construction of Plasmonic Core–Satellite Nanostructures on Substrates Based on DNA-Directed Self-Assembly as a Sensitive and Reproducible Biosensor". In: *ACS Applied Materials &amp Interfaces* 7.49 (2015), pp. 27131–27139. DOI: 10.1021/acsami.5b07152.

[43] F. Mazur et al. “Core-satellite gold nanoparticle biosensors for monitoring cobalt ions in biological samples”. In: *Sensors and Actuators B: Chemical* 268 (2018), pp. 182–187. DOI: 10.1016/j.snb.2018.04.089.

[44] J. R. Waldeisen et al. “Disassembly of a Core–Satellite Nanoassembled Substrate for Colorimetric Biomolecular Detection”. In: *ACS Nano* 5.7 (2011), pp. 5383–5389. DOI: 10.1021/nn2002807.

[45] Z. Weng et al. “Self-assembly of core-satellite gold nanoparticles for colorimetric detection of copper ions”. In: *Analytica Chimica Acta* 803 (2013), pp. 128–134. DOI: 10.1016/j.aca.2013.09.036.

[46] J. H. Yoon, J. Lim, and S. Yoon. “Controlled Assembly and Plasmonic Properties of Asymmetric Core–Satellite Nanoassemblies”. In: *ACS Nano* 6.8 (2012), pp. 7199–7208. DOI: 10.1021/nn302264f.

[47] S.-Y. Ding et al. “Nanostructure-based plasmon-enhanced Raman spectroscopy for surface analysis of materials”. In: *Nature Reviews Materials* 1.6 (2016). DOI: 10.1038/natrevmats.2016.21.

[48] C. Zong et al. “Surface-Enhanced Raman Spectroscopy for Bioanalysis: Reliability and Challenges”. In: *Chemical Reviews* 118.10 (2018), pp. 4946–4980. DOI: 10.1021/acs.chemrev.7b00668.

[49] N. Gandra et al. “Plasmonic Planet–Satellite Analogues: Hierarchical Self-Assembly of Gold Nanostructures”. In: *Nano Letters* 12.5 (2012), pp. 2645–2651. DOI: 10.1021/nl3012038.

[50] J. Feng et al. “A SERS active bimetallic core–satellite nanostructure for the ultrasensitive detection of Mucin-1”. In: *Chemical Communications* 51.79 (2015), pp. 14761–14763. DOI: 10.1039/c5cc05255f.

[51] L. Xu et al. “Regiospecific Plasmonic Assemblies for in Situ Raman Spectroscopy in Live Cells”. In: *Journal of the American Chemical Society* 134.3 (2012), pp. 1699–1709. DOI: 10.1021/ja2088713.

[52] Y. Yang et al. “Gold nanoring core-shell satellites with abundant built-in hotspots and great analyte penetration: An immunoassay platform for the SERS/fluorescence-based detection of carcinoembryonic antigen”. In: *Chemical Engineering Journal* 409 (2021), p. 128173. DOI: 10.1016/j.cej.2020.128173.

[53] B. Lv et al. “Multifunctional satellite Fe3O4-Au@TiO2 nano-structure for SERS detection and photo-reduction of Cr(VI)”. In: *Colloids and Surfaces A: Physicochemical and Engineering Aspects* 513 (2017), pp. 234–240. DOI: 10.1016/j.colsurfa.2016.10.048.

[54] Z. Zhang et al. “Au-Protected Ag Core/Satellite Nanoassemblies for Excellent Extra-/Intracellular Surface-Enhanced Raman Scattering Activity”. In: *ACS Applied Materials &amp Interfaces* 9.50 (2017), pp. 44027–44037. DOI: 10.1021/acsami.7b14976.

[55] L. Wu, U. Glebe, and A. Böker. "Fabrication of Thermoresponsive Plasmonic Core-Satellite Nanoassemblies with a Tunable Stoichiometry via Surface-Initiated Reversible Addition-Fragmentation Chain Transfer Polymerization from Silica Nanoparticles". In: *Advanced Materials Interfaces* 4.15 (2017), p. 1700092. DOI: 10.1002/admi.201700092.

[56] C. Rossner, O. Glatter, and P. Vana. "Stimulus-Responsive Planet–Satellite Nanostructures as Colloidal Actuators: Reversible Contraction and Expansion of the Planet–Satellite Distance". In: *Macromolecules* 50.18 (2017), pp. 7344–7350. DOI: 10.1021/acs.macromol.7b01267.

[57] R. Jin et al. "Core–Satellite Mesoporous Silica–Gold Nanotheranostics for Biological Stimuli Triggered Multimodal Cancer Therapy". In: *Advanced Functional Materials* 28.31 (2018). DOI: 10.1002/adfm.201801961.

[58] C. Pei et al. "FeOOH@Metal–Organic Framework Core–Satellite Nanocomposites for the Serum Metabolic Fingerprinting of Gynecological Cancers". In: *Angewandte Chemie* 132.27 (2020), pp. 10923–10927. DOI: 10.1002/ange.202001135.

[59] H. Liu et al. "Radiosensitive core/satellite ternary heteronanostructure for multimodal imaging-guided synergistic cancer radiotherapy". In: *Biomaterials* 226 (2020), p. 119545. DOI: 10.1016/j.biomaterials.2019.119545.

[60] M. Behi et al. "Nanoassembled Peptide Biosensors for Rapid Detection of Matrilysin Cancer Biomarker". In: *Small* 16.16 (2020). DOI: 10.1002/smll.201905994.

[61] B. Chen and F. Wang. "$NaYbF_4$@CaF_2 core-satellite upconversion nanoparticles: one-pot synthesis and sensitive detection of glutathione". In: *Nanoscale* 10.42 (2018), pp. 19898–19905. DOI: 10.1039/c8nr05552a.

[62] J. Robert et al. "Coiled-coil peptide-based assembly of a plasmonic core-satellite polymer-metal nanocomposite as an efficient photothermal agent for drug delivery applications". In: *Journal of Colloid and Interface Science* 641 (2023), pp. 929–941. DOI: 10.1016/j.jcis.2023.03.085.

[63] X. Zhao et al. "Building heterogeneous core–satellite chiral assemblies for ultrasensitive toxin detection". In: *Biosensors and Bioelectronics* 66 (2015), pp. 554–558. DOI: 10.1016/j.bios.2014.12.021.

[64] Y. Zheng et al. "DNA-Directed Self-Assembly of Core-Satellite Plasmonic Nanostructures: A Highly Sensitive and Reproducible Near-IR SERS Sensor". In: *Advanced Functional Materials* 23.12 (2012), pp. 1519–1526. DOI: 10.1002/adfm.201202073.

[65] Z. Huang et al. "Surface-enhanced Raman scattering from plasmonic Ag-nanocube@Au-nanospheres core@satellites". In: *Journal of Raman Spectroscopy* 48.2 (2016), pp. 217–223. DOI: 10.1002/jrs.5032.

[66] J. Zhao et al. "Core–Satellite Gold Nanoparticle Complexes Grown by Inert Gas-Phase Condensation". In: *The Journal of Physical Chemistry C* 124.44 (2020), pp. 24441–24450. DOI: 10.1021/acs.jpcc.0c07346.

[67] A. S. D. S. Indrasekara et al. "Tailoring the Core–Satellite Nanoassembly Architectures by Tuning Internanoparticle Electrostatic Interactions". In: *Langmuir* 34.48 (2018), pp. 14617–14623. DOI: 10.1021/acs.langmuir.8b02792.

[68] K. Xu et al. "Ultrasensitive detection of vitamin E by signal conversion combined with core-satellite structure-based plasmon coupling effect". In: *The Analyst* 147.3 (2022), pp. 398–403. DOI: 10.1039/d1an02289j.

[69] M. Abbas, S. RamuluTorati, and C. Kim. "Multifunctional Fe_3O_4/Au core/satellite nanocubes: an efficient chemical synthesis, characterization and functionalization of streptavidin protein". In: *Dalton Transactions* 46.7 (2017), pp. 2303–2309. DOI: 10.1039/c6dt04486g.

[70] P. Rohani, M. K. Sharma, and M. T. Swihart. "Core–satellite ZnS–Ag nanoassemblies: Synthesis, structure, and optical properties". In: *Journal of Colloid and Interface Science* 463 (2016), pp. 207–213. DOI: 10.1016/j.jcis.2015.10.059.

[71] W. Zhang et al. "Tip-Selective Growth of Silver on Gold Nanostars for Surface-Enhanced Raman Scattering". In: *ACS Applied Materials &amp Interfaces* 10.17 (2018), pp. 14850–14856. DOI: 10.1021/acsami.7b19328.

[72] Y. Cai, W. Peng, and P. Vana. "Gold nanoparticle ring arrays from core–satellite nanostructures made to order by hydrogen bond interactions". In: *Nanoscale Advances* 4.13 (2022), pp. 2787–2793. DOI: 10.1039/d2na00204c.

[73] T. Fließbach. *Elektrodynamik*. Springer Berlin Heidelberg, 2022. DOI: 10.1007/978-3-662-64889-6.

[74] E. Hecht. *Optik*. De Gruyter, 2018. DOI: 10.1515/9783110526653.

[75] L. Novotny and B. Hecht. *Principles of Nano-Optics*. Cambridge University Press, 2012. DOI: 10.1017/cbo9780511794193.

[76] S. A. Maier. *Plasmonics: Fundamentals and Applications*. Springer Science + Business Media LLC, 2007. ISBN: 0-387-33150-6.

[77] P. West et al. "Searching for better plasmonic materials". In: *Laser Photonics Reviews* 4.6 (2010), pp. 795–808. DOI: 10.1002/lpor.200900055.

[78] S. Hunklinger. *Festkörperphysik*. De Gruyter, 2017. DOI: 10.1515/9783110567755.

[79] G. Kumar and P. K. Sarswat. "Interaction of Surface Plasmon Polaritons with Nanomaterials". In: *Reviews in Plasmonics 2015*. Springer International Publishing, 2016, pp. 103–129. ISBN: 9783319246062. DOI: 10.1007/978-3-319-24606-2_5.

[80] W. O. F. Carvalho and J. R. Mejía-Salazar. "Plasmonics for Telecommunications Applications". In: *Sensors* 20.9 (Apr. 2020), p. 2488. ISSN: 1424-8220. DOI: 10.3390/s20092488.

[81] K. A. Willets and R. P. Van Duyne. "Localized Surface Plasmon Resonance Spectroscopy and Sensing". In: *Annual Review of Physical Chemistry* 58.1 (May 2007), pp. 267–297. ISSN: 1545-1593. DOI: 10.1146/annurev.physchem.58.032806.104607.

[82] S. Kawata. *Near-Field Optics and Surface Plasmon Polaritons*. Springer, 2001.

[83] J. A. Stratton. *Electromagnetic Theory*. McGraw-Hill Book Company, Inc, 1941.

[84] E. H. Land and J. S. Friedman. *Patent US1918848: Polarizing Refracting Bodies*. Patent. Apr. 1929. URL: https://patents.google.com/patent/US1918848.

[85] C. A. Balanis. *Antenna Theory Analysis and Design*. John Willey Sons, Inc., 2005.

[86] P. Bharadwaj, B. Deutsch, and L. Novotny. "Optical Antennas". In: *Advances in Optics and Photonics* 1.3 (2009), p. 438. DOI: 10.1364/aop.1.000438.

[87] C. A. Balanis, ed. *Modern Antenna Handbook*. Wiley, 2007. DOI: 10.1002/9780470294154.

[88] C. Wolff. *Yagiantennen*. Jan. 2024. URL: https://www.radartutorial.eu/06.antennas/Yagiantennen.de.html.

[89] N. Engheta, A. Salandrino, and A. Alù. "Circuit Elements at Optical Frequencies: Nanoinductors, Nanocapacitors, and Nanoresistors". In: *Physical Review Letters* 95.9 (2005), p. 095504. DOI: 10.1103/physrevlett.95.095504.

[90] L. Sun et al. "Tuning the properties of magnetic nanowires". In: *IBM Journal of Research and Development* 49.1 (2005), pp. 79–102. DOI: 10.1147/rd.491.0079.

[91] P. B. Johnson and R. W. Christy. "Optical Constants of the Noble Metals". In: *Physical Review B* 6.12 (1972), pp. 4370–4379. DOI: 10.1103/physrevb.6.4370.

[92] D. Dominguez et al. "Fourier plane imaging microscopy". In: *Journal of Applied Physics* 116.10 (2014). DOI: 10.1063/1.4895157.

[93] M. A. Lieb, J. M. Zavislan, and L. Novotny. "Single-molecule orientations determined by direct emission pattern imaging". In: *Journal of the Optical Society of America B* 21.6 (2004), p. 1210. DOI: 10.1364/josab.21.001210.

[94] C. Huang et al. "Gain, detuning, and radiation patterns of nanoparticle optical antennas". In: *Physical Review B* 78.15 (2008), p. 155407. DOI: 10.1103/physrevb.78.155407.

[95] N. Hartmann et al. "Radiation Channels Close to a Plasmonic Nanowire Visualized by Back Focal Plane Imaging". In: *ACS Nano* 7.11 (2013), pp. 10257–10262. DOI: 10.1021/nn404611q.

[96] I. C. Seo et al. "Fourier-plane investigation of plasmonic bound states in the continuum and molecular emission coupling". In: *Nanophotonics* 9.15 (2020), pp. 4565–4577. DOI: 10.1515/nanoph-2020-0343.

[97] A. B. Vasista, D. K. Sharma, and G. P. Kumar. "Fourier Plane Optical Microscopy and Spectroscopy". In: (2019), pp. 1–14. DOI: 10.1002/3527600434.eap817.

[98] B. E. A. Saleh and M. C. Teich. *Fundamentals of Photonics*. Wiley, 1991. DOI: 10.1002/0471213748.

[99] C. Guo et al. "Fourier light-field microscopy". In: *Optics Express* 27.18 (2019), p. 25573. DOI: 10.1364/oe.27.025573.

[100] I. Sersic, C. Tuambilangana, and A. F. Koenderink. "Fourier microscopy of single plasmonic scatterers". In: *New Journal of Physics* 13.8 (2011), p. 083019. DOI: 10.1088/1367-2630/13/8/083019.

[101] J. A. Kurvits, M. Jiang, and R. Zia. "Comparative analysis of imaging configurations and objectives for Fourier microscopy". In: *Journal of the Optical Society of America A* 32.11 (2015), p. 2082. DOI: 10.1364/josaa.32.002082.

[102] H. Weyl. "Ausbreitung elektromagnetischer Wellen über einem ebenen Leiter". In: *Annalen der Physik* 365.21 (1919), pp. 481–500. DOI: 10.1002/andp.19193652104.

[103] N. Hartmann et al. "Launching Propagating Surface Plasmon Polaritons by a Single Carbon Nanotube Dipolar Emitter". In: *Nano Letters* 12.1 (2011), pp. 177–181. DOI: 10.1021/nl203270b.

[104] A. Sommerfeld. "Über die Ausbreitung der Wellen in der drahtlosen Telegraphie". In: *Annalen der Physik* 333.4 (1909), pp. 665–736. DOI: 10.1002/andp.19093330402.

[105] M. J. O. Strutt. "Strahlung von Antennen unter dem Einfluß der Erdbodeneigenschaften. A. Elektrische Antennen". In: *Annalen der Physik* 393.6 (1929), pp. 721–750. DOI: 10.1002/andp.19293930603.

[106] B. van der Pol and K. F. Niessen. "Über die Ausbreitung elektromagnetischer Wellen über eine ebene Erde". In: *Annalen der Physik* 398.3 (1930), pp. 273–294. DOI: 10.1002/andp.19303980302.

[107] W. Lukosz and M. Meier. "Lifetimes and radiation patterns of luminescent centers close to a thin metal film". In: *Optics Letters* 6.5 (1981), p. 251. DOI: 10.1364/ol.6.000251.

[108] W. Lukosz and R. E. Kunz. "Light emission by magnetic and electric dipoles close to a plane interface. I. Total radiated power". In: *Journal of the Optical Society of America* 67.12 (1977), p. 1607. DOI: 10.1364/josa.67.001607.

[109] W. Lukosz and R. E. Kunz. "Light emission by magnetic and electric dipoles close to a plane dielectric interface. II. Radiation patterns of perpendicular oriented dipoles". In: *Journal of the Optical Society of America* 67.12 (1977), p. 1615. DOI: 10.1364/josa.67.001615.

[110] Schott AG. *Technische Daten D263*. Sept. 2023. URL: https://www.schott.com/de-de/products/d-263-p1000318/technical-details.

[111] K. Yee. "Numerical solution of initial boundary value problems involving Maxwell's equations in isotropic media". In: *IEEE Transactions on Antennas and Propagation* 14.3 (1966), pp. 302–307. DOI: 10.1109/tap.1966.1138693.

[112] A. Faflove, S. C. Hagness, and M. Picket-May. "The Electrical Engineering Handbook". In: ed. by W.-K. Chen. Elsevier Academic Press, 2004. Chap. Computational Electromagnetics: The Finite-Difference Time-Domain Method, pp. 629–669.

[113] N. J. Higham. *Accuracy and Stability of Numerical Algorithms*. Society for Industrial and Applied Mathematics, 2002. DOI: 10.1137/1.9780898718027.

[114] M. Bass et al. “Optical Rectification”. In: *Physical Review Letters* 9.11 (1962), pp. 446–448. DOI: 10.1103/physrevlett.9.446.

[115] R. W. Terhune, P. D. Maker, and C. M. Savage. “Optical Harmonic Generation in Calcite”. In: *Physical Review Letters* 8.10 (1962), pp. 404–406. DOI: 10.1103/physrevlett.8.404.

[116] N. Bloembergen et al. “Optical Second-Harmonic Generation in Reflection from Media with Inversion Symmetry”. In: *Physical Review* 174.3 (1968), pp. 813–822. DOI: 10.1103/physrev.174.813.

[117] S. Boroviks et al. “Anisotropic second-harmonic generation from monocrystalline gold flakes”. In: *Optics Letters* 46.4 (2021), p. 833. DOI: 10.1364/ol.413003.

[118] G. Wiederrecht. *Handbook of Nanoscale Optics and Electronics*. Elsevier Science Technology Books, 2010. ISBN: 9780123751799.

[119] M. Göppert-Mayer. “Über Elementarakte mit zwei Quantensprüngen”. In: *Annalen der Physik* 401.3 (1931), pp. 273–294. DOI: 10.1002/andp.19314010303.

[120] R. W. Boyd. *Nonlinear Optics*. Elsevier, 2008. ISBN: 9780080485966.

[121] C. V. Raman and K. S. Krishnan. “A New Type of Secondary Radiation”. In: *Nature* 121.3048 (1928), pp. 501–502. DOI: 10.1038/121501c0.

[122] G. Landsberg and L. Mandelstam. “Eine neue Erscheinung bei der Lichtzerstreuung in Krystallen”. In: *Die Naturwissenschaften* 16.28 (1928), pp. 557–558. DOI: 10.1007/bf01506807.

[123] J. R. Ferraro, K. Nakamoto, and C. W. Brown. *Introductory Raman Spectroscopy*. Academic Press, 2003.

[124] R. R. Jones et al. “Raman Techniques: Fundamentals and Frontiers”. In: *Nanoscale Research Letters* 14.1 (2019). DOI: 10.1186/s11671-019-3039-2.

[125] J. M. Chalmers and P. R. Griffiths, eds. *Handbook of Vibrational Spectroscopy*. Wiley, 2001. DOI: 10.1002/0470027320.

[126] J. P. Camden et al. “Probing the Structure of Single-Molecule Surface-Enhanced Raman Scattering Hot Spots”. In: *Journal of the American Chemical Society* 130.38 (2008), pp. 12616–12617. DOI: 10.1021/ja8051427.

[127] S. L. Kleinman et al. “Structure Enhancement Factor Relationships in Single Gold Nanoantennas by Surface-Enhanced Raman Excitation Spectroscopy”. In: *Journal of the American Chemical Society* 135.1 (2012), pp. 301–308. DOI: 10.1021/ja309300d.

[128] J. Langer et al. “Present and Future of Surface-Enhanced Raman Scattering”. In: *ACS Nano* 14.1 (2019), pp. 28–117. DOI: 10.1021/acsnano.9b04224.

[129] Oxford Instruments. *iDus 416 CCD*. Sept. 2023. URL: https://andor.oxinst.com/products/idus-spectroscopy-cameras/idus-416.

[130] Allresist. “Protective Coating PMMA Electra 92 (AR-PC 5090) Data Sheet”. In: 2016.

[131] K. A. Materials. “SU-8 Permanent Negative Epoxy Photoresist”.

[132] V. R. Manfrinato et al. "Resolution Limits of Electron-Beam Lithography toward the Atomic Scale". In: *Nano Letters* 13.4 (Apr. 2013), pp. 1555–1558. ISSN: 1530-6984. DOI: 10.1021/nl304715p.

[133] J. Notte et al. "An Introduction to the Helium Ion Microscope". In: *AIP Conference Proceedings*. AIP, 2007. DOI: 10.1063/1.2799423.

[134] P. Sigmund. "Theory of Sputtering. I. Sputtering Yield of Amorphous and Polycrystalline Targets". In: *Physical Review* 184.2 (Aug. 1969), pp. 383–416. DOI: 10.1103/PhysRev.184.383. URL: https://link.aps.org/doi/10.1103/PhysRev.184.383 (visited on 05/03/2023).

[135] F. Laible et al. "Time-effective strategies for the fabrication of poly- and single-crystalline gold nano-structures by focused helium ion beam milling". en. In: *Nanotechnology* 30.23 (Mar. 2019), p. 235302. ISSN: 0957-4484. DOI: 10.1088/1361-6528/ab0506.

[136] R. Livengood et al. "Subsurface damage from helium ions as a function of dose, beam energy, and dose rate". In: *Journal of Vacuum Science & Technology B: Microelectronics and Nanometer Structures Processing, Measurement, and Phenomena* 27.6 (Dec. 2009), pp. 3244–3249. ISSN: 1071-1023. DOI: 10.1116/1.3237101.

[137] O. Scholder et al. "Helium focused ion beam fabricated plasmonic antennas with sub-5 nm gaps". en. In: *Nanotechnology* 24.39 (Sept. 2013), p. 395301. ISSN: 0957-4484. DOI: 10.1088/0957-4484/24/39/395301.

[138] G. Hlawacek et al. "Helium ion microscopy". In: *Journal of Vacuum Science & Technology B, Nanotechnology and Microelectronics: Materials, Processing, Measurement, and Phenomena* 32.2 (2014). DOI: 10.1116/1.4863676.

[139] Gelest Inc. *tridecafluoro-1,1,2,2-tetrahydrooctyl-1-trichlorosilane Safety Data Sheet SIT8174.0*.

[140] K. Chau et al. "Dependence of the quality of adhesion between poly(dimethyl siloxane) and glass surfaces on the composition of the oxidizing plasma". In: *Microfluidics and Nanofluidics* 10.4 (Nov. 2010), pp. 907–917. ISSN: 1613-4990. DOI: 10.1007/s10404-010-0724-y.

[141] C.-F. Chen. "Characterization of fracture energy and toughness of air plasma PDMS–PDMS bonding by T-peel testing". In: *Journal of Adhesion Science and Technology* 32.11 (Dec. 2017), pp. 1239–1252. ISSN: 1568-5616. DOI: 10.1080/01694243.2017.1406877.

[142] W. Peng et al. "Gold-Planet–Silver-Satellite Nanostructures Using RAFT Star Polymer". In: *ACS Macro Letters* 5.11 (2016), pp. 1227–1231. DOI: 10.1021/acsmacrolett.6b00681.

[143] N. G. Bastús et al. "Synthesis of Highly Monodisperse Citrate-Stabilized Silver Nanoparticles of up to 200 nm: Kinetic Control and Catalytic Properties". In: *Chemistry of Materials* 26.9 (2014), pp. 2836–2846. DOI: 10.1021/cm500316k.

[144] Y. Cai et al. "Silica-Coated Magnetite Nanoparticles Carrying a High-Density Polymer Brush Shell of Hydrophilic Polymer". In: *Macromolecular Rapid Communications* 39.13 (2018), p. 1800226. DOI: 10.1002/marc.201800226.

[145] E. D. Palik, ed. *Handbook of Optical Constants of Solids*. Elsevier, 1985. DOI: 10.1016/c2009-0-20920-2.

[146] E. Gürdal et al. "Enhancement of the second harmonic signal of nonlinear crystals by a single metal nanoantenna". In: *Nanoscale* 12.45 (2020), pp. 23105–23115. DOI: 10.1039/d0nr05696k.

[147] N. Jiang, X. Zhuo, and J. Wang. "Active Plasmonics: Principles, Structures, and Applications". In: *Chemical Reviews* 118.6 (2017), pp. 3054–3099. DOI: 10.1021/acs.chemrev.7b00252.

[148] N. M. Yunos et al. "The depolarization factors for ellipsoids and some of their properties". In: (2019). DOI: 10.11113/mjfas.v15n6.1364.

[149] S. Singh, R. S. Kaler, and S. Sharma. "A Novel Two-Dimensional Material Based Optical Fiber Surface Plasmon Resonance Sensor for Sensing of Organic Compounds in Infrared Spectrum Window". In: *Journal of Communications Technology and Electronics* 63.11 (Nov. 2018), pp. 1269–1275. ISSN: 1555-6557. DOI: 10.1134/s1064226918110116.

[150] C. Oubre and P. Nordlander. "Optical Properties of Metallodielectric Nanostructures Calculated Using the Finite Difference Time Domain Method". In: *The Journal of Physical Chemistry B* 108.46 (Oct. 2004), pp. 17740–17747. ISSN: 1520-5207. DOI: 10.1021/jp0473164.

[151] G. M. Hale and M. R. Querry. "Optical Constants of Water in the 200-nm to 200-μm Wavelength Region". In: *Applied Optics* 12.3 (1973), p. 555. DOI: 10.1364/ao.12.000555.

[152] P. E. Ciddor. "Refractive index of air: new equations for the visible and near infrared". In: *Applied Optics* 35.9 (1996), p. 1566. DOI: 10.1364/ao.35.001566.

[153] K. M. Mayer and J. H. Hafner. "Localized Surface Plasmon Resonance Sensors". In: *Chemical Reviews* 111.6 (2011), pp. 3828–3857. DOI: 10.1021/cr100313v.

[154] H. Chen et al. "Shape- and Size-Dependent Refractive Index Sensitivity of Gold Nanoparticles". In: *Langmuir* 24.10 (Apr. 2008), pp. 5233–5237. ISSN: 1520-5827. DOI: 10.1021/la800305j.

[155] K. Takamura, H. Fischer, and N. R. Morrow. "Physical properties of aqueous glycerol solutions". In: *Journal of Petroleum Science and Engineering* 98-99 (2012), pp. 50–60. DOI: 10.1016/j.petrol.2012.09.003.

[156] J. Kington. *Image information along polar coordinates system in Python*. Stack Overflow. URL: https://stackoverflow.com/questions/3798333/image-information-along-a-polar-coordinate-system/3806851#3806851.

[157] Raith GmbH. *Laser Interferometer Stage*. 2023. URL: https://raith.com/technology/laser-interferometer-stage/.

[158] V. Subramanian, E. E. Wolf, and P. V. Kamat. "Catalysis with TiO_2/Gold Nanocomposites. Effect of Metal Particle Size on the Fermi Level Equilibration". In: *Journal of the American Chemical Society* 126.15 (2004), pp. 4943–4950. DOI: 10.1021/ja0315199.

[159] J. R. Rouxel et al. “Enhanced second harmonic generation of gold nanostars: optimizing multipolar radiation to improve nonlinear properties”. In: *Optics Express* 27.4 (2019), p. 5620. DOI: 10.1364/oe.27.005620.

[160] K. Nadolski et al. “Adverse Role of Shape and Size in Second-Harmonic Scattering from Gold Nanoprisms”. In: *The Journal of Physical Chemistry C* 124.27 (2020), pp. 14797–14803. DOI: 10.1021/acs.jpcc.0c03489.

[161] D. Gérard and S. K. Gray. “Aluminium plasmonics”. In: *Journal of Physics D: Applied Physics* 48.18 (2014), p. 184001. DOI: 10.1088/0022-3727/48/18/184001.

[162] N. Pazos-Perez et al. “Modular assembly of plasmonic core–satellite structures as highly brilliant SERS-encoded nanoparticles”. In: *Nanoscale Advances* 1.1 (2019), pp. 122–131. DOI: 10.1039/c8na00257f.

[163] I. H. Malitson. “Interspecimen Comparison of the Refractive Index of Fused Silica”. In: *Journal of the Optical Society of America* 55.10 (1965), p. 1205. DOI: 10.1364/josa.55.001205.

[164] C. F. Bohren and D. R. Huffman. *Absorption and Scattering of Light by Small Particles*. Wiley, 1998. DOI: 10.1002/9783527618156.

[165] S. Oldenburg. “Light Scattering from Gold Nanoshells”. PhD thesis. Rice University, 2000.

[166] F. Benz et al. “SERS of Individual Nanoparticles on a Mirror: Size Does Matter, but so Does Shape”. In: *The Journal of Physical Chemistry Letters* 7.12 (2016), pp. 2264–2269. DOI: 10.1021/acs.jpclett.6b00986.

[167] K. Bian et al. “Formation of self-assembled gold nanoparticle supercrystals with facet-dependent surface plasmonic coupling”. In: *Nature Communications* 9.1 (2018). DOI: 10.1038/s41467-018-04801-9.

[168] J. H. Yoon et al. “Surface Plasmon Coupling in Dimers of Gold Nanoparticles: Experiment and Theory for Ideal (Spherical) and Nonideal (Faceted) Building Blocks”. In: *ACS Photonics* 6.3 (2019), pp. 642–648. DOI: 10.1021/acsphotonics.8b01424.

[169] P. K. Jain, W. Huang, and M. A. El-Sayed. “On the Universal Scaling Behavior of the Distance Decay of Plasmon Coupling in Metal Nanoparticle Pairs: A Plasmon Ruler Equation”. In: *Nano Letters* 7.7 (2007), pp. 2080–2088. DOI: 10.1021/nl071008a.

[170] C. Tabor et al. “On the Use of Plasmonic Nanoparticle Pairs As a Plasmon Ruler: The Dependence of the Near-Field Dipole Plasmon Coupling on Nanoparticle Size and Shape”. In: *The Journal of Physical Chemistry A* 113.10 (2008), pp. 1946–1953. DOI: 10.1021/jp807904s.

[171] W. Demtröder. *Experimentalphysik 2. Elektrizität und Optik*. 7. Aufl. 2017. Springer-Lehrbuch. Berlin, Heidelberg: Springer Berlin Heidelberg, 2018. 1449 pp. ISBN: 9783662557907.

[172] A. Michota and J. Bukowska. “Surface-enhanced Raman scattering (SERS) of 4-mercaptobenzoic acid on silver and gold substrates”. In: *Journal of Raman Spectroscopy* 34.1 (2003), pp. 21–25. DOI: 10.1002/jrs.928.

[173] T. Chen et al. “Hotspot-Induced Transformation of Surface-Enhanced Raman Scattering Fingerprints”. In: *ACS Nano* 4.6 (2010), pp. 3087–3094. DOI: 10.1021/nn100269v.

[174] R. Li et al. “Vibrational spectroscopy and density functional theory study of 4-mercaptobenzoic acid”. In: *Spectrochimica Acta Part A: Molecular and Biomolecular Spectroscopy* 148 (2015), pp. 369–374. DOI: 10.1016/j.saa.2015.03.132.

[175] A. Capocefalo et al. “Exploring the Potentiality of a SERS-Active pH Nano-Biosensor”. In: *Frontiers in Chemistry* 7 (2019). DOI: 10.3389/fchem.2019.00413.

[176] U. H. Kurzweg. *Area of a spherical cap*. Dec. 2017. URL: https://mae.ufl.edu/~uhk/SPHERICAL-CAP.pdf.

[177] A. J. Haes and R. P. V. Duyne. “A Nanoscale Optical Biosensor: Sensitivity and Selectivity of an Approach Based on the Localized Surface Plasmon Resonance Spectroscopy of Triangular Silver Nanoparticles”. In: *Journal of the American Chemical Society* 124.35 (2002), pp. 10596–10604. DOI: 10.1021/ja020393x.

Acknowledgement

Lastly, I would like to thank some people and institutions who greatly helped me to make this thesis come true.

First and foremost, I would like to thank Prof. Monika Fleischer for giving me this opportunity in the first place, but also for helping me out whenever advice was needed.

I would also like to thank PD Dr. Dai Zhang for being my second reviewer.

I also want to thank Prof. Dr. Alfred J. Meixner for being my second supervisor.

I also deeply want to thank Dr. Yingying Cai for providing me with the core-satellite samples, the discussions over them and the feedback you provided me regarding these samples.

Another collaborator, who made parts of this thesis possible, is Felix Schneider. Thank you for providing me with a plethora of data regarding SHG and BFP imaging.

A thank you also goes to Frederick Unger, who helped me with the Raman measurement setup.

Additionally, I want to thank Annika Mildner for setting up the BFP setup used over the course of this work.

For financial support through parts of this work, I would like to thank the state of Baden-Württemberg, which provided me with a scholarship through the Landesgraduiertenförderung.

Of course, I also want to thank the whole group (who I don't want to name in fear of forgetting someone) and the various people who were part of it for longer or shorter periods of time. Not only did I learn most of the techniques used from one of you, but you also provided me with friendship and fun, encouragement and great memories. And also the nanobeer!

Lastly, I would like to thank my family and my girlfriend Luisa Rehkopf for all the support they gave me, not only throughout this work, but my whole academic career and life in general. Thank you!